UNIVERSITY OF SOUTHAMPTON

FACULTY OF NATURAL AND ENVIROMENTAL SCIENCES

School of Chemistry

Oxygen Sensing and Oxide Formation: Optimisation and Novel X-ray Studies

by

Andrew Stephen Leach

Thesis for the degree of Doctor of Philosophy

May 2019

UNIVERSITY OF SOUTHAMPTON

ABSTRACT

FACULTY OF NATURAL AND ENVIROMENTAL SCIENCES

School of Chemistry

Thesis for the degree of Doctor of Philosophy

Oxygen Sensing and Oxide Formation: Optimisation and Novel X-ray Studies

Andrew Stephen Leach

Platinum remains vital for the use of electrochemical devices, therefore, understanding of the reactions which occur at the platinum-solution interface is paramount in continuing to improve gas sensors, as well as fuel cells and electrolysers. The following body of work uses a number of electrochemical techniques and X-ray spectroscopies to investigate the surface processes of platinum in acidic media.

The pH range over which the electrochemical behaviour can be accurately modelled by the Nernst equation, has been extended into highly acidic solutions by employing the Hammett acidity function (H_0) in place of pH when working below pH 1. Sulfuric acid and perchloric acid have been investigated. Both the hydrogen region and oxide formation region have been studied, and the comparison between these two potential regions by cyclic voltammetry has produced a method for electrolyte concentration measurements.

A variety of X-ray spectroscopies have been used to provide additional understanding of the oxide formation process on platinum. Conventional X-ray Absorption Near Edge Structure (XANES) and Extended X-ray Absorption Fine Structure (EXAFS) have presented a baseline for High Energy Resolution Fluorescence Detection (HERFD)-XANES, which offers higher spectral resolution, and Energy Dispersive EXAFS (EDE), which can measure on much smaller time scales. The surface oxidation and reduction of platinum nanoparticles will be discussed.

Additionally, a statistically designed set of experiments have been presented, investigating five parameters in an industrial gas sensor electrode manufacturing process. Both sensor output measurements and lab based techniques were employed to characterise the electrodes. It was shown that the electrode loading could be reduced without affecting the sensors initial performance, so cheaper electrodes can be used.

Table of Contents

DECLARATION OF AUTHORSHIP

I, Andrew Stephen Leach

declare that this thesis and the work presented in it are my own and has been generated by me as the result of my own original research.

Oxygen Sensing and Oxide Formation: Optimisation and Novel X-ray Studies .....

.....

I confirm that:

1. This work was done wholly or mainly while in candidature for a research degree at this University;
2. Where any part of this thesis has previously been submitted for a degree or any other qualification at this University or any other institution, this has been clearly stated;
3. Where I have consulted the published work of others, this is always clearly attributed;
4. Where I have quoted from the work of others, the source is always given. With the exception of such quotations, this thesis is entirely my own work;
5. I have acknowledged all main sources of help;
6. Where the thesis is based on work done by myself jointly with others, I have made clear exactly what was done by others and what I have contributed myself;
7. Parts of this work have been published as:

Leach, A. S.; Russell, A. E. Method and apparatus of electrolyte concentration measurement, September 30, 2016.

Signed: .....

Date: .....

Acknowledgements

First and foremost I would like to thank Andrea Russell, my supervisor, for her continued support and giving me the opportunity to study for my PhD. I would also like to thank John Chapples, Keith Pratt and Marvin Gayle for their support.

I owe a lot to David Inwood, Danai Panagoulia and Turgut Sonmez for their day to day advice and bedding me into the Russell group, as well as Alex Keeler for never agreeing with me! Haoling "Howard" Huang (HHH) has always been on hand with tasty oriental treats, I will never forget moon cake. Giancarlo Banda visiting form Brazil for my last year was a tremendous influence, always offering a hug! Everyone from the Russell group, and wider electrochemistry group, have always made the office a welcoming place open to discussions, perfect for research. Ann and Jenny of the Chemistry Tea Room have provided countless cups of rejuvenating tea, which have powered many additional hours work, and I am very grateful.

I would also like to thank Venushan Varatharajan, Rebecca Gummer, and Suji Pathmalingam for being thoughtful and intelligent project students, who helped guide my research while doing some important experiments.

A special mention needs to be made for the companions who have made synchrotron beamtimes both possible and (at times) bearable. David Inwood, Andrea Russell, Veronica Celorrio, HHH, Colleen Jackson, Nikolay Zhelev, Sam Fitch, Penny Whalley, Patrick Cullen, Rhodri Jervis, and of course the beamline staff from Diamond beamlines I20-scanning, I20-EDE, and B18 have all been excellent to me over the last 4 years.

Thomas Penfold, Denis Kramer and Diego Gianolio were all very helpful in analysis of the HERFD XANES with their knowledge of DFT calculations, and use of their computers.

Finally, and most importantly I would like to show my appreciation to my parents Stephen and Kate, and my siblings Daniel and Christine who have all helped me achieve this great feat. None of the above however have endured the worst and enjoyed the best of this journey as much as Jessica Shennan, without whom I could not have completed this work, thank you for everything.

Chapter 1: Introduction

1.1 Aims

This project aims to improve the understanding of how pH and acid concentration affect the features of platinum cyclic voltammetry. This will enable a deeper understanding of how adsorbates interact with the metal surface at more extreme conditions than have currently have been studied. The work has industrial importance as the electrodes being tested are the same as those used in gas sensors and the acid concentration range is also the same as these sensors use. The methods employed will mainly be cyclic voltammetry, derivative voltammetry and using the Hammet acidity function to describe pH for the very concentrated solutions.

Following on from this initial work, there will be further studies using X-ray absorbance spectroscopy (XAS) to give another perspective on the surface processes. A number of different synchrotron techniques have been used, including XANES (X-ray Absorption Near Edge Spectra), EXAFS (Extended X-ray Absorption Fine Structure), EDE (Energy Dispersive EXAFS) and HERFD (High Energy Resolution Fluorescence Detection) XANES. These complimentary techniques will elucidate in more detail which chemical states are present, what structure they are in and the timescale on which these changes occur. These measurements will allow the determination of both the electronic and structural properties of the platinum particles, while under electrochemical control. This will aid the understanding of the electrocatlyic activity of the nanoparticles.

Finally, a study of the electrode fabrication process of a gas sensor electrode using a statistical framework is presented. This method allows the maximum outcomes from the fewest experiments. Five factors of the electrode fabrication process (electrode loading, pressing pressure, PTFE content, use of a dispersing agent and catalyst surface area) were investigated. The electrodes were tested in the laboratory and by the factory standard tests at our industrial partner City Technology's premises in Portsmouth and the results analysed by a Design of Experiment (DoE) protocol. This study aims to identify the most important factors in the electrode fabrication process, so that these can be studied further.

1.2 City Technology Background

City Technology is the leading brand for Honeywell's gas sensors and produces over 300 different sensors for 28 gasses. City Technology sells products to customers from 48 countries and 80% of annual production is exported.

The company was set up in 1977 by scientists working at London's City University and made novel oxygen sensors using a technology developed by the University's Wolfson Institute for Electrochemical Technology. After expanding, combustible and toxic gas sensors were produced, and after increasing sales, City Technology won a total of four Queen's awards by 1992. In 1996 the company was floated on the London Stock Exchange and four years later was acquired by First Technology Plc, a UK based international group, manufacturing products that improve safety and the protection of people and their environment. In March 2006 First Technology Plc was acquired by Honeywell, a large US technology conglomerate. Now City Technology annually supplies three million sensors worldwide.[1]

1.3 Oxygen Sensors

1.3.1 Oxygen Pump Gas sensor

The focus of two of the results chapters (three and five) are gas sensors, therefore, the design of a City Technology oxygen pump gas sensor will be outlined. Figure 1a shows a schematic of the sensor. There are three platinum electrodes; the sensing electrode, the reference electrode, and the counter electrode. Pt has been shown previously to be used as a reference electrode when more typical references cannot be used.[2] The electrolyte is sulfuric acid. Figure 1b shows two whole sensors.

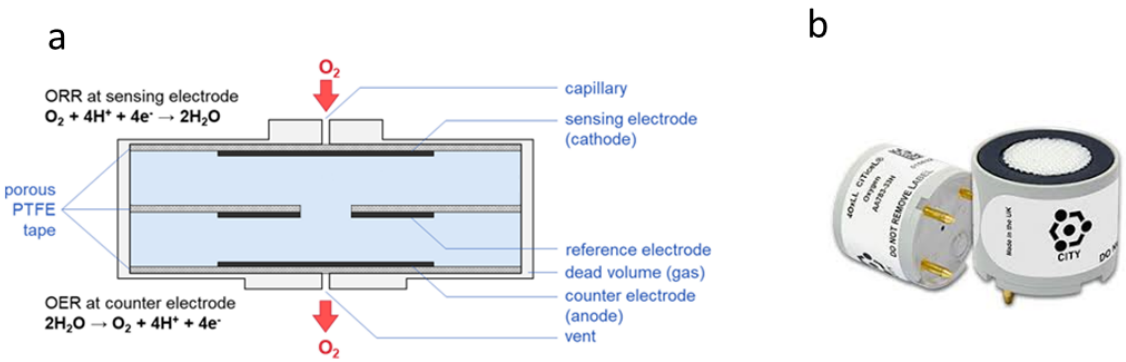

Figure 1. a. Schematic showing the cross section of a City Technology oxygen pump gas sensor. Image adapted from one drawn by Tammy Nimmo. b. Show two complete City Technology oxygen sensors.

The current generated by the sensor is limited by a capillary, which ensures a well-defined flow of oxygen gas to the sensing electrode.[3] The capillary ensures that the reaction in the sensor is mass transport limited, meaning the diffusion of the analyte gas to the electrode is slower than the reaction at the electrode surface. Since the reaction is mass transport limited, the current produced by the sensor is proportional to the concentration of oxygen in the air. The electrochemical cell reduces oxygen at the platinum sensing electrode. The potential of the sensing electrode is biased at -0.6 V versus another Pt reference electrode. The overall reaction is shown in Equation 1.

$$O_2 + 4H^+ + 4e^- \rightarrow 2H_2O$$

Equation 1

At a counter electrode (on the bottom of the cell in Figure 1a) the reverse reaction is occurs, where water is oxidised to oxygen, which then diffuses out of the sensor. This reaction is shown in Equation 2.

$$2H_2O \rightarrow O_2 + 4H^+ + 4e^-$$

Equation 2

Since oxygen is pushed through the cell it is called an “oxygen pump” sensor. There are three main issues that will be confronted in the thesis. Firstly, as the sensor has to be open to the environment, the concentration of the hygroscopic electrolyte can vary with differing environmental conditions, most notably the humidity and was discussed by Willet.[4] This will be addressed in the first results chapter. Secondly, the current material used as an electro catalyst is platinum, which is both expensive and rare. Optimisation of platinum catalysis and/or the replaces with cheaper more abundant materials would greatly beneficial, therefore, measurements of platinum particles *in situ* and *in operando* will be presented in the second results chapter. Finally, the design of all three electrodes is considered to be of upmost importance to a number of key sensor parameters and this will be discussed in the final results chapter. Design parameters such as ratio of catalyst to binder, loading and the use of a dispersing agent will be measured against sensor performance metrics, such as response time and cross sensitivity. As the ORR and OER (Oxygen evolution reaction) depicted in Figure 1a are both catalysed in the oxygen pump sensor by platinum these reactions will be discussed later in this chapter.

1.3.2 Alternative Oxygen Sensors

There are other types of oxygen sensors available. For example, electrochemical lead anode sensors.[5] Figure 2 shows a cross section of one of these sensors. In this type of sensor there is the same reaction of oxygen reduction at the sensing electrode, but the counter electrode reaction is different. The electrolyte is also different and is basic. The reaction at the counter electrode (which is made from lead), is the electrochemical oxidation of lead, shown in Equation 3.

$$2Pb + 4OH^- \rightarrow 2PbO + 2H_2O + 4e^-$$

Equation 3

As a result of the anode being consumed in equation 3, these sensors' lifetime can be limited by the size of the anode. Typically, these oxygen sensors last for up to 2 years, however this can be extended by increasing the size of the anode or using the sensor in a low oxygen concentration environment. This is in contrast to the electrochemical oxygen pump sensor, which is not limited by the size of any of the electrodes.

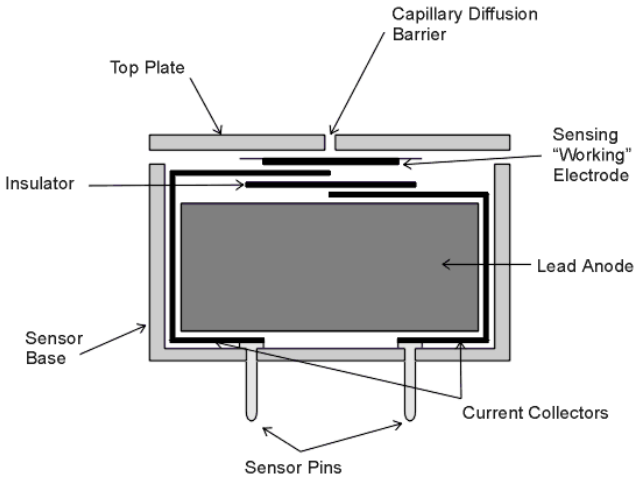

Figure 2. Schematic showing the cross section of an oxygen gas sensor with a consumable lead anode.

Aside from electrochemical sensors, there are also resistive oxygen gas sensors. These work by measuring the resistivity of a semiconductor, the resistivity is related to the oxygen partial pressure (pO_2) surrounding the material. Some of the first resistive sensors were titania based.[6] As the partial pressure of oxygen increases, the oxygen vacancies fill up, reducing the number of mobile charge carries in the material, which increases the resistivity. Equation 4 shows the relationship between oxygen partial pressure and resistivity.

$$R_{sensor} \rightarrow A_0 exp\left(\frac{E_A}{kT}\right)\left({}_pO_2\right)^m$$

Equation 4

Where A_0 denotes a constant and E_A is the thermal activation energy of the electrical conductivity. The exponent *m* is a parameter dependant on the material being used.[7] These sensors are very useful in harsh environments, for example in the exhaust of a car, and can operate up to and over 1000 °K.[8]

1.4 Platinum Electrocatalysts

1.4.1 Platinum and the Oxygen Reduction Reaction

The oxygen pump sensor uses platinum as an electrocatalyst for ORR. Platinum has long been studied as an excellent example of an electrocatlyst, in particular, being able to catalyse the electrochemical reduction of oxygen to water (the oxygen reduction reaction or ORR).[9–11] The ORR is a very important reaction, which has far reaching impacts across gas sensors, fuel cells and other electrochemical devices.[12] Stephens *et al.* discussed how the current global platinum production is not even close to being able to satisfy the demand for cars, should fuel cell cars become widespread.[12] A Toyota Mirai fuel cell car currently uses ~30 g of platinum per car. At present, fewer than 200 tons of platinum are being produced each year, globally.[13] Therefore, if the total annual production of Pt was used entirely for the production of fuel cell powered car, fewer than 7 million cars could be produced (about 10% of the global production). As a result, trying to optimise the use of platinum by better understand its catalytic activity and reaction mechanisms, is paramount. This will allow for a more efficient per appliance use. Alternatively, replacing platinum with cheaper more abundant materials, which can mimic the catalytic properties of platinum, is also desirable.

The electrochemical ORR reaction mechanism has a number of possible paths, which were simplified to three main pathways by Wroblowa *et al.* in 1976.[14] Figure 3 shows these reaction pathways, first, for any electrochemical reaction the reactant must diffuse to the surface. Once the oxygen is adsorbed to the metal surface, a four-electron reduction to water can occur, this is shown by the red line. Alternatively, a two-electron reduction to hydrogen peroxide can occur, shown by the first blue line. This can be followed by a second two reduction (shown by the second blue line) also yielding water as the reduction product. The third reaction pathway is the initial two electron reduction to hydrogen peroxide followed by desorption of this intermediate, which can undergo chemical disproportionation to water and oxygen (shown by the dotted black lines).

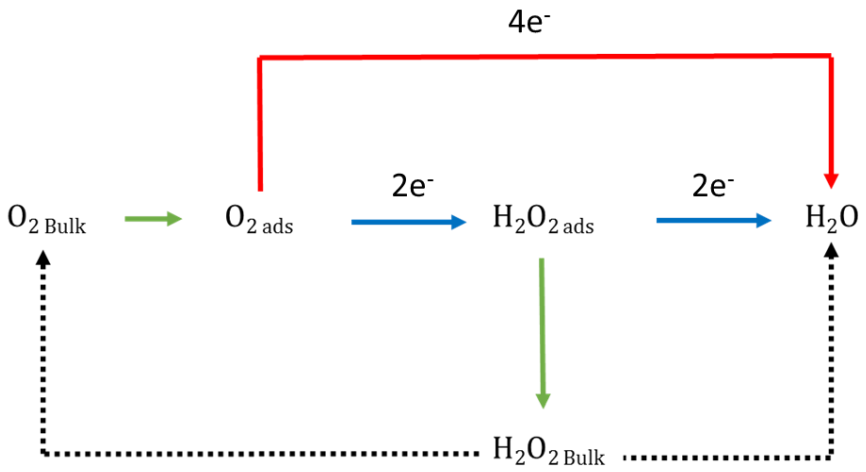

Figure 3. Schematic of the electrochemical oxygen reduction reaction pathways in acidic media as simplified by Wroblowa *et al.*[14] The green arrows show adsorption and desorption processes, the red line shows the four electron reduction, and the blue lines show two electron reductions and the dotted black lines show chemical disproportionation.

The kinetics of the ORR are slow, as a result there has been a lot of interest in the mechanism of the reaction, as well as finding the most active and cost efficient electrocatalysts. The electrode potential, material used, and the surface structure all affect the rate of the reactions described in Figure 3, on platinum electrodes, although the exact mechanism is still debated a "series" four electron reduction (via hydrogen peroxide) is generally accepted for platinum.[15] This mechanism is known as the 'associative' mechanism, and involves the protonation of an adsorbed O_2 molecule to form an intermediate peroxide species. This intermediate is then protonated again, breaking the O-O bond and yielding an H_2O molecule and leaving an adsorbed O_{ads} on the surface. The O_{ads} is then protonated twice to produce the second H_2O molecule. The O-O bond in the peroxide species could also be cleaved resulting in OH_{ads} and O_{ads} species on the metal surface. These species would then be protonated separately.

1.4.2 Platinum Electrochemistry

Figure 4 shows a typical cyclic voltammogram of platinum, the features of which will be described in more detail in the experimental chapter. Four regions have been highlighted in Figure 4 by coloured areas on the plot. The red region is the part of the voltammogram where the potential at the surface of the electrode is positive enough to oxidise the platinum surface, and eventually a multi-layer oxide is formed. The green region is the reverse, where, as the potential is swept back towards more reducing potentials and the oxide which was formed is reduced. The purple region is associated with the surface adsorption of hydrogen atoms (a monolayer covering), and the blue region the stripping of the adsorbed monolayer of hydrogen.

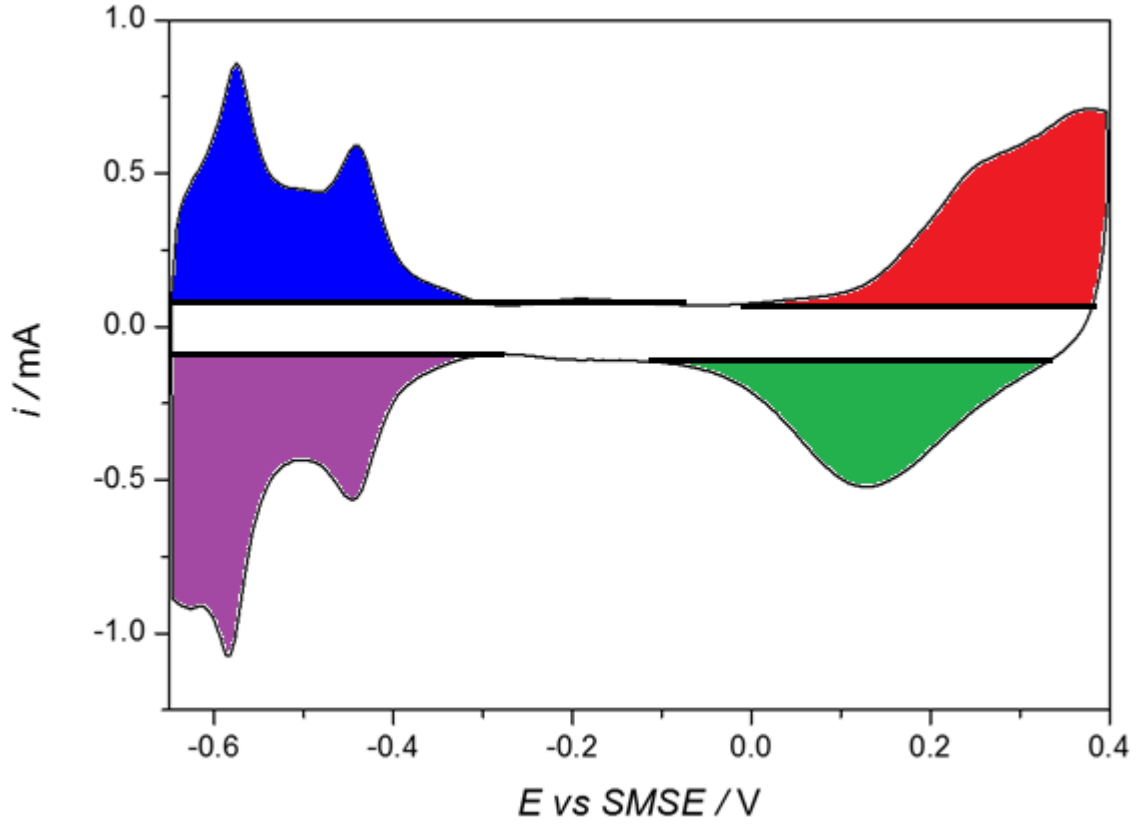

Figure 4. Cyclic voltammogram of a Pt black catalyst painted onto a carbon Toray paper button (11 mm diameter) with a Pt loading of 0.255 mg cm^{-2} in 1 mol dm^{-3} H_2SO_4 measured at a scan rate of 0.01 V s^{-1}. The electrochemical cell was purged with nitrogen gas.

Platinum has been studied electrochemically for decades. In the 1960s, Conway was proposing oxidation steps that are still being discussed to this day. For example Huang *et al.* reported using SERS (surface enhanced Raman spectroscopy) to observe Pt-OH on the surface of a Pt(111) electrode in 2016.[16,17] Angerstein-Kozlowska *et al.* proposed that the initial oxidation is to Pt_4OH_{ads}, which forms at the onset of surface oxidation (red area in Figure 4), followed by Pt_2OH_{ads} and finally $PtOH_{ads}$.[18] The reversibility of these processes is also discussed, the first process is considered to be reversible, and the following processes not. The consequence of the irreversibility of later oxidations is shown as a hysteresis between the peaks in the cyclic voltammograms. Once the whole surface is OH_{ads} covered, the further oxidation of the surface to PtO, at more positive potentials, was proposed. There have been many others including single crystal experiments that have shown the multiple hydrogen features, at more reducing potentials, are crystal face specific.[19] At more positive potentials than where OH is adsorbed on the surface, there is a place exchange where the oxygen penetrates the surface of the metal forming a 3-dimensional oxide structure.[9]

This thesis will address the issue of how features of the platinum voltammogram are affected by the pH of the electrolyte. Van der Niet *et al.* and Gisbert *et al.* have investigated effects of pH on

the features of the platinum voltammogram.[20,21] In both cases the pH range was between 2-12 and well defined surfaces were studied (although Gisbert *et al.* also studied polycrystalline platinum electrodes). The features of the 'hydrogen region' (between 0 V *vs.* RHE and 0.4 V *vs.* RHE) were observed to shift ~50 mV per pH unit in both cases, this is unexpected as a shift of 59 mV would be predicted from the theory. Sheng *et al.* present a study on the hydrogen binding energy on platinum surfaces as a function of pH, and suggested that the hydrogen binding energy increases with increasing pH, in agreement with van der Niet *et al.* and Gisbert.[22] In the presented work (Chapter 3) the solutions used are much more acidic (pH <0), as a result the Hammett acidity function (H_0) will be used to describe the proton donating ability of the solutions. pH is not used since some of the assumptions it is based on are not valid at high concentrations. The Hammett acidity function values have been determined experimentally, all factors, including ionic strength, are accounted for. The Hammett acidity function will be discussed in more detail in Chapter 3.

1.5 X-Ray Absorption Spectroscopy

In this thesis extended X-ray absorption fine structure (EXAFS) and X-ray absorption near edge structure (XANES) has been used to measure platinum nanoparticles, to understand how this material changes as a function of potential. The link between activity of a new material and an independently measurable parameter, or a theoretical calculation, has in the case of the electrocatalytic reduction ORR, been achieved. A correlation has been established between the centre of the oxidation state of the metal, and electrocatalytic activity. X-ray absorption spectroscopy (XAS) offers a direct means to measure such relationships; catalyst oxidation state may be empirically resolved from the X-ray absorption near-edge structure (XANES) region, while coordination number, bond lengths in the particles can be determined from electron backscattering calculations in the extended X-ray absorption fine structure (EXAFS).[23,24]

X-ray absorption spectroscopy (XAS) was first reported by Fricke, who observed oscillations in X-ray absorption spectra.[25] Later, bright tuneable X-ray sources at synchrotrons were built, which increased the development of XAS. Modern XAS theory, advanced by Sayers *et al.,* allowed the local coordination of atoms could be calculated.[26] Throughout the 1970's this field was advanced and the initial EXAFS theory was established, although only single scattering paths were considered.[27,28] From the previously established theory, multiple scattering paths (where the ejected photoelectron scatters off more than one atom before returning to the target atom) have since been included. This allows for a more accurate determination of a samples' structure when fitting beyond the first shell, where multiple scattering paths have similar lengths to single scattering paths.[28,29]

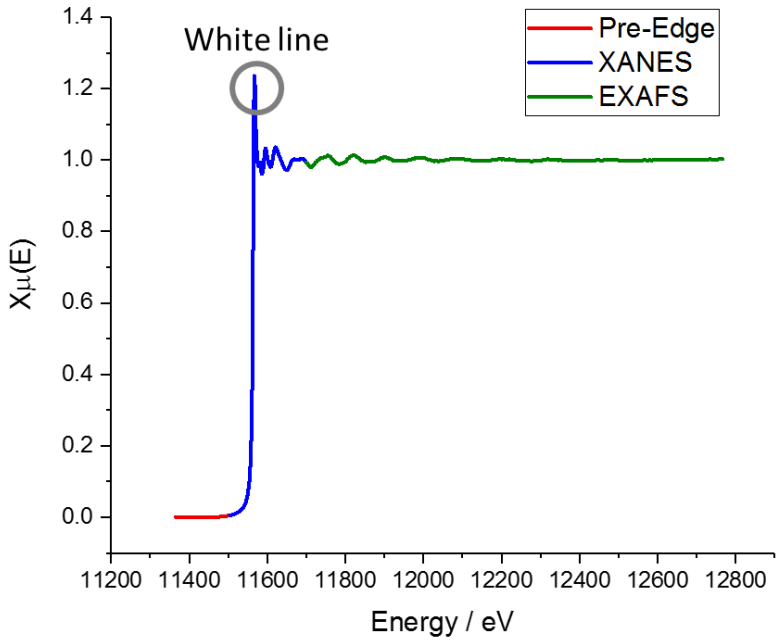

Figure 5. Shows a typical platinum XAS with the three main regions highlighted, pre-edge in red, XANES in blue and EXAFS in green. The white line is in the grey circle.

Figure 5 shows the different regions of an XAS spectrum, the X-ray Absorption Near Edge Structure (XANES) (in blue) and EXAFS (in green). Figure 6 shows a schematic of the electronic configuration of platinum and the L_3 transition that has been measured in this thesis. An incoming x-ray excites a 2p electron, which is ejected as a photoelectron (the photoelectric effect), the core hole is then filled by an electron from the 5d orbital. The drop in energy of the d-electron to the core hole results in a fluoresced x-ray. When the ejected photoelectrons are excited to a higher electron shell, which must be unoccupied, the transition must obey the dipole selection rule ($\Delta\ell = \pm 1$).

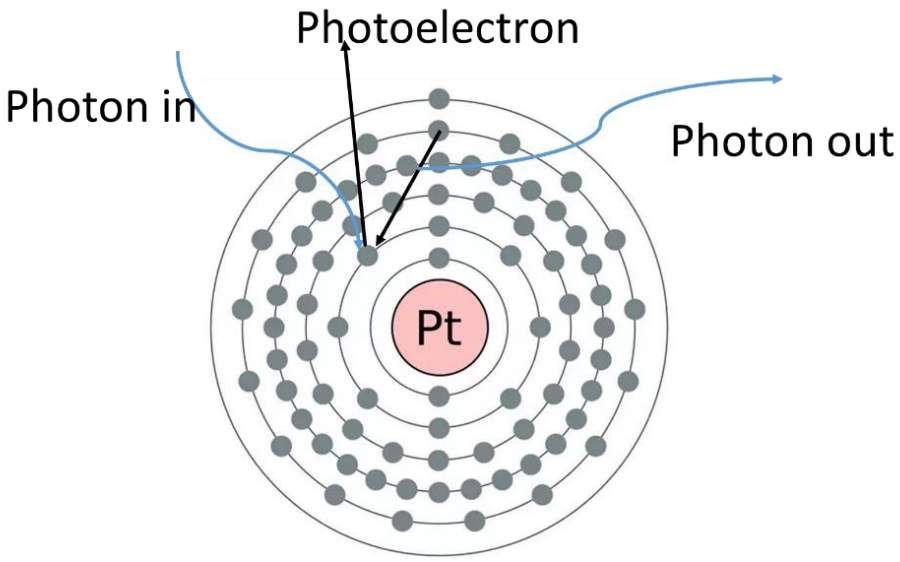

Figure 6. Showing the electronic structure of platinum and the L_3 edge transition of a 2p electron being ejected as a photoelectron and a 5d electron filling the core hole. Blue lines show X-rays, black lines show electron transitions.

1.5.1 Beamline Techniques

Three main types of beamline will be discussed; conventional XAS, HERFD XANES, and EDE. They each measure the same event with differing advantages and disadvantages. Conventional XAS is typically performed in transmission or fluorescence, the measurements take between one to 15 minutes per full XAS spectrum for concentrated samples. HERFD XANES is performed in fluorescence, excess sample can lead to self-absorption, which can affect the data quality. These measurements are slower (up to an hour per XANES region of spectra) but yield much higher energy resolution than conventional XAS. A Johann spectrometer (or Von Hamos analyser), where the fluoresced X-rays travel to a set of analyser crystals that are spherically bent and focus the fluoresced X-rays onto a detector. Control of the position of the analyser crystals and detector allow for very high energy resolution in the spectra, as they diffract the fluoresced beam, ensuring only a very small window of wavelengths are detected. HERFD XAS is a technique where XAS spectra are measured with an instrumental broadening that is lower than the core hole lifetime broadenings. The additional energy resolution doesn't improve the data in the EXAFS region, so EXAFS are not collected using HERFD unless two elements with a similar edge position are being measured, as the emission line can be narrowly selected using the Johan spectrometer.[30] Finally EDE need to be executed in transmission, meaning a greater amount of sample is required, which can add to resistance though the electrode layer. Since all XAS is a bulk technique, all the target atoms are being measured simultaneously, so it is paramount that all the sample is exposed to the same electrochemical potential at the same time. EDE measurements are by far the fastest, meaning "real-time" measurements are possible.[31–34] These techniques will be discussed it more detail including with beamline schematics in Chapter four.

1.5.2 EXAFS

The EXAFS part of the spectrum is from around 150 eV above the edge to over 1 keV above the edge. Local coordination and therefore the materials structure can be determined from this part of the spectrum. EXAFS is based on the statement "The probability of an x-ray being absorbed is enhanced if it leads to constructive interference of the photoelectron at the location of the absorbing atom".[35] The EXAFS equation is based on Fermi's Golden Rule. This rule states that the absorption coefficient is related to both the unaffected core energy level before it interferes with the neighbouring atoms, and the final state in which the core energy level has been affected and a

photoelectron has been ejected.[35] The undulations observed in the EXAFS are due to the ejected photoelectron being scattered off nearby atoms, as a result, bond distances, type of atom, the number of surrounding atoms, and the degree of disorder in the system can all be calculated. The observed EXAFS is the sum of all the multiple photoelectron scattering paths. Each photoelectron scattering path ($\chi_i(k)$) can described as shown in equation 5.

$$\chi_i(k) = \frac{(N_i s_0^2) F_{eff_i}(k)}{kR_i^2} sin[2kR_i + \varphi_i(k)]\, e^{-2\sigma_i^2 k^2} e^{\frac{-2R_i}{\lambda(k)}}$$

Equation 5

$$k = \sqrt{\frac{2m_e(E - E_0)}{\hbar^2}}$$

Equation 6

$$R_i = R_{cif} + \Delta R_i$$

Equation 7

Equations 5-7 show 'the EXAFS equation' and is the equation used to fit the experimental data. Blue terms are generated from multiple photoelectron scattering theory. Red terms contain sample specific information (structural/electronic), and are the terms that can be modified to fit the experimental data. The subscript *i* denotes terms that can change value for each scattering path. F_{effi} is the effective scattering amplitude, $\varphi_i(k)$ is the phase shift, and $\lambda(k)$ is the mean free path of the photoelectron. All these parameters are calculated using the FEFF6 code in the Artimis software package.[29,36]

k is the photoelectron wavenumber. N_i is the degeneracy of the scattering path, S_o^2 the amplitude reduction factor, R_i is the effective half path length of the photoelectron (comprised of R_{cif} — the theoretical half path length, and ΔR_i — the change in half path length). For a single scattering path (with only one scattering atom) R_i is equal to the bond length. σ_i^2 is the mean square of the disorder of the path length, and E_0 is an energy correction parameter, which aligns theory and experimental data. All these terms are fit during the data analysis. Although the amplitude reduction factor differs between elements, it is consistent between different species for the same edge, and is often between 0.7 and 1.0.[37] The physical description of all these properties is given in a final function for χ(*k*)

Benfield, Frenkel and Glasner, Jentys, and Beale have all helped to develop the field of taking the average coordination numbers from EXAFS to show how the size and shape of nanoparticles changes.[38–41] This is done by comparing the ratios of coordination numbers, thus requiring the fits

to be over a number of layers (or shells) of atoms. Mathew *et al.* showed that at using a *k*-range of 12 compared to 21 significantly impacted the quality of the data analysis for platinum EXAFS, demonstrating that fitting shells at a large *k*-range is vital.[42]

1.5.3 XANES

The XANES, as well as being influenced by the local coordination of the absorbing atom, is also impacted by the oxidation state.[23] The two most obvious features that change with oxidation state, are the position of the absorption edge measured in eV, and the intensity of the "white line" (the first peak after the edge on platinum spectra).[43,44] The transition that gives rise to the "white line" in platinum XAS is Pt 2*p*3/2 state to the partially filled 5*d*5/2 state. As atoms are oxidised, the edge position is increased by a few electronvolts, as the remaining core electrons are in lower energy states (therefore harder to excite). Multiple scattering and multiple photon absorption complicate the analysis of the XANES region. The white line intensity has been shown to have a linear relationship to the number of unoccupied 5d states.[45] XANES analysis typically involves comparing the experimental spectra to reference spectra (not to theoretical spectra as in EXAFS).[23]

1.5.4 Electrochemical *in situ* Platinum XAS

Since the X-ray energy of the platinum L_3 edge is sufficient to penetrate through air and water, *in situ* measurements are possible, and this is one of the main advantages of using XAS. The first Pt/C *in situ* measurements were conducted by O'Grady and Koningsberger who, in the 1980's, investigated the XANES of open circuit and operating conditions for H_3PO_4 and CF_3SO_3H fuel cells. They also prepared pellet samples that were exposed to different gaseous environments for EXAFS analysis. It was noted upon analysis of the XANES that electronic structure was affected by the electrochemical potential applied to the sample. The EXAFS showed that as the Pt/C sample (which was partially oxidized to start), was heated in hydrogen gas for one hour the Pt-O bonds were no longer observed. The Pt-Pt bond lengths shortened, also indicating that the sample was no longer oxidised.[42]

More recent studies have shown significantly more detail, for example Safonova *et al.* were able to determine the binding site of CO on a platinum nanoparticle (0.5-3 nm) surface.[46] The support material was Al_2O_3. Analysis of HERFD XANES measurements allow such detail to be determined. The analysis was completed by comparing the experimental spectrum to a number of calculated spectra for different adsorption sites. In this case the CO was in the gas phase and the sample was in a quartz tube reactor. HERFD XANES studies have also been carried out using electrochemical

control in 0.1 M perchloric acid electrolyte of 1.2 nm diameter platinum particles supported on carbon.[47] Merte *et al.* also compared their experimental data to a range of calculated spectra, concluding that there are three distinct potential regimes. Hydrogen chemisorption between 0 V *vs.* RHE and ~0.3 V *vs.* RHE, oxygen chemisorption (as OH or O) between 0.3 *vs.* RHE and 0.96 V *vs.* RHE, and platinum oxide formation at or above 0.96 V *vs.* RHE. Similar analysis will be carried out in this work.

In situ electrochemical measurements by Jackson *et al.* have used conventional XANES to probe the d-band occupancy of platinum nanoparticles on two different support materials, carbon and boron carbide.[48,49] It was observed that there are electronic interactions between the support and the platinum nanoparticles, which affected the hydrogen oxidation reaction activity of the electrocatalysts. The boron carbide proved to be more active for catalysing the hydrogen oxidation reaction than carbon support catalysts. The nanoparticles were between 1-3 nm and the electrolyte used was perchlorc acid.

In situ electrochemical EDE measurements have also been carried out, Mathew and Russell discussed the pros and cons of the EDE experimental setup in 2000. Carbon supported platinum fuel cell catalysts were studied using EDE as well as conventional XAS.[42] Although the speed of acquisition was vastly improved, the data quality suffered as a result, both the XANES and EXAFS regions were distorted. Rose *et al.* when measuring 40 wt% Pd/C, in a time resolved *in situ* electrochemical study, were able to observe the potential dependant palladium lattice expansion (associated with the formation of the β–hydride phase).[50] Not only was a lattice expansion measured, but comparison of H_2SO_4 and D_2SO_4 showed different onset potentials, kinetics, and quantity of β–hydride phase formed.

1.6 Thesis Outline

The remainder of the thesis is presented in the following five chapters, outlined below.

Chapter two is a summary of the samples and chemicals used, equipment and experimental procedure used during the work. Additional details are provided in the appropriate chapters.

Chapter three is the first results chapter, where the characteristic electrochemical signature of platinum is discussed in detail. The surface processes that may be occurring at both the reduction and oxidation of the surface, are also discussed. The work is carried out over a range of pH values from 0 to -6 in two different electrolytes.

Chapter four discusses four different X-ray absorption spectroscopy methods and analyses of platinum on carbon catalysts. The platinum samples are measured using conventional extended

X-ray absorption fine structure (EXAFS) and X-ray absorption near edge structure (XANES), as well as high energy resolution fluorescence detection (HERFD) XANES and energy dispersive EXAFS (EDE). The benefits of each technique will be addressed, as well as the limitations. The results from all three methods will be presented, focusing on the analysis of the materials electronic structure.

Chapter five presents the construction and results of a Design of Experiment (DoE) used to improve the electrode fabrication method for gas sensing electrodes. This chapter was completed in collaboration with City Technology. Five parameters were tested, all suspected of impacting the electrode structure and performance. 32 batches of electrodes were prepared and then tested by both the author and City Technology. The results were all tested using the statistical analysis DoE.

Chapter six concludes the thesis, with some outlines for future work to expand on what has been achieved.

1.7 References

1 C. Technology, History, https://www.citytech.com/index.html, (accessed 8 September 2018).

2 K. K. Kasem and S. Jones, *Platin. Met. Rev.*, 2008, **52**, 100–106.

3 Chan, Y.S.; Tantram, A. D. S.; Hobbs, B. S.; Finbrow, J.R. US4406770A, **1982**.

4 M. Willett, *Sensors*, 2014, **14**, 6084–6103.

5 C. Technology, Lead Andoe Sensor, https://www.citytech.com/loader/frame_loader.asp?page=https://www.citytech.com/technology/02-sensors.asp, (accessed 20 February 2019).

6 E. F. Gibbons, A. H. Meitzler, L. R. Foote, P. J. Zacmanidis and G. L. Beaudoin, *SAE Trans.*, 1975, 84, 825–835.

7 R. Moos, N. Izu, F. Rettig, S. Reiss, W. Shin and I. Matsubara, *Sensors (Basel).*, 2011, **11**, 3439–65.

8 N. Izu, S. Nishizaki, W. Shin, T. Itoh, M. Nishibori and I. Matsubara, *Sensors (Basel).*, 2009, **9**, 8884–95.

9 B. E. Conway, *Prog. Surf. Sci.*, 1995, **49**, 331–452.

10 B. V. Tilak, B. E. Conway and H. Angerstein-Kozlowska, *J. Electroanal. Chem. Interfacial Electrochem.*, 1973, **48**, 1–23.

11 K. J. Vetter and J. W. Schultze, *J. Electroanal. Chem. Interfacial Electrochem.*, 1972, **34**, 131–139.

12 I. E. L. Stephens, A. S. Bondarenko, U. Grønbjerg, J. Rossmeisl and I. Chorkendorff, *Energy Environ. Sci.*, 2012, **5**, 6744.

13 PGM MARKET REPORT FEBRUARY 2018, http://www.platinum.matthey.com/documents/new-item/pgm market reports/pgm_market_report_february_2018.pdf, (accessed 21 May 2019).

14 H. S. Wroblowa, Y. C. Pan and G. Razumney, *J. Electroanal. Chem.*, 1976, **69**, 195–201.

15 N. M. Markovic, T. J. Schmidt, V. Stamenkovic and P. N. Ross, *Fuel Cells*, 2001, **1**, 105–116.

16 V. Stamenkovic, B. N. Grgur, P. N. Ross and N. M. Markovic, *J. Electrochem. Soc.*, 2005, **152**, A277–A282.

17 D. Gilroy and B. E. Conway, *Can. J. Chem.*, 1968, **46**, 875–890.

18 H. Angerstein-Kozlowska, B. E. Conway and W. B. A. Sharp, *J. Electroanal. Chem. Interfacial Electrochem.*, 1973, **43**, 9–36.

19 N. M. Marković, B. N. Grgur and P. N. Ross, *J. Phys. Chem. B*, 1997, **101**, 5405–5413.

20 M. J. T. C. van der Niet, N. Garcia-Araez, J. Hernández, J. M. Feliu and M. T. M. Koper, *Catal. Today*, 2013, **202**, 105–113.

21 R. Gisbert, G. García and M. T. M. Koper, *Electrochim. Acta*, 2010, **55**, 7961–7968.

22 W. Sheng, Z. Zhuang, M. Gao, J. Zheng, J. G. Chen and Y. Yan, *Nat. Commun.*, 2015, **6**, 5848.

23 A. E. Russell and A. Rose, *Chem. Rev.*, 2004, **104**, 4613–4636.

24 A. N. Mansour, J. W. Cook and D. E. Sayers, *J. Phys. Chem.*, 1984, **88**, 2330–2334.

25 H. Fricke., *Phys. Rev.*, 1920, **16**, 202–215.

26 D. E. Sayers, E. A. Stern and F. W. Lytle, *Phys. Rev. Lett.*, 1971, **27**, 1204–1207.

27 E. A. Stern and D. E. Sayers, *Phys. Rev. Lett.*, 1973, **30**, 174–177.

28 P. A. Lee and J. B. Pendry, *Phys. Rev. B*, 1975, **11**, 2795–2811.

29 J. J. Rehr and R. C. Albers, *Rev. Mod. Phys.*, 2000, **72**, 621–654.

30 M. Tromp, Springer, Dordrecht, 2014, pp. 171–188.

31 E. Dartyge, C. Depautex, J. M. Dubuisson, A. Fontaine, A. Jucha, P. Leboucher and G. Tourillon, *Nucl. Instruments Methods Phys. Res. Sect. A Accel. Spectrometers, Detect. Assoc. Equip.*, 1986, **246**, 452–460.

32 R. P. Phizackerley, Z. U. Rek, G. B. Stephenson, S. D. Conradson, K. O. Hodgson, T. Matsushita, H. Oyanagi and IUCr, *J. Appl. Crystallogr.*, 1983, **16**, 220–232.

33 K. R. Dunning, L. N. Watson, D. J. Sharkey, H. M. Brown, R. J. Norman, J. G. Thompson, R. L. Robker and D. L. Russell, *Biol. Reprod.*, , DOI:ARTN 89DOI 10.1095/biolreprod.111.096271.

34 T. Matsushita, in *AIP Conference Proceedings*, 1980, p. 109.

35 S. Calvin, *XAFS for Everyone*, CRC Press, 2014.

36 B. Ravel and M. Newville, *J. Synchrotron Radiat.*, 2005, **12**, 537–541.

37 G. G. Li, F. Bridges and C. H. Booth, *Phys. Rev. B*, 1995, **52**, 6332–6348.

38 R. E. Benfield, *J. Chem. Soc., Faraday Trans.*, 1992, **88**, 1107–1110.

39 D. Glasner and A. I. Frenkel, in *AIP Conference Proceedings*, AIP, 2007, vol. 882, pp. 746–748.

40 A. Jentys, *Phys. Chem. Chem. Phys.*, 1999, **1**, 4059–4063.

41 A. M. Beale and B. M. Weckhuysen, *Phys. Chem. Chem. Phys.*, 2010, **12**, 5562.

42 R. J. Mathew and A. E. Russell, *Top. Catal.*, 2000, **10**, 231–239.

43 Y. Dai, T. J. Gorey, S. L. Anderson, S. Lee, S. Lee, S. Seifert and R. E. Winans, *J. Phys. Chem. C*, 2017, **121**, 361–374.

44 H. Yoshida, S. Nonoyama, Y. Y. T. Hattori and T. Hattori, *Phys. Scr.*, 2005, **2005**, 813.

45 B. Qi, I. Perez, P. H. Ansari, F. Lu and M. Croft, *Phys. Rev. B*, 1987, **36**, 2972–2975.

46 O. V. Safonova, M. Tromp, J. A. van Bokhoven, F. M. F. de Groot, J. Evans and P. Glatzel, *J. Phys. Chem. B*, 2006, **110**, 16162.

47 L. R. Merte, F. Behafarid, D. J. Miller, D. Friebel, S. Cho, F. Mbuga, D. Sokaras, R. Alonso-Mori, T.-C. Weng, D. Nordlund, A. Nilsson and B. Roldan Cuenya, *ACS Catal.*, 2012, **2**, 2371–2376.

48 C. Jackson, G. T. Smith, D. W. Inwood, A. S. Leach, P. S. Whalley, M. Callisti, T. Polcar, A. E. Russell, P. Levecque and D. Kramer, *Nat. Commun.*, 2017, **8**, 15802.

49 C. Jackson, G. T. Smith, M. Markiewicz, D. W. Inwood, A. S. Leach, P. S. Whalley, A. R. Kucernak, A. E. Russell, D. Kramer and P. B. J. Levecque, *J. Electroanal. Chem.*, 2018, **819**, 163–170.

50 A. Rose, O. South, I. Harvey, S. Diaz-Moreno, J. R. Owen and A. E. Russell, *Phys. Chem. Chem. Phys.*, 2005, **7**, 366–372.

Chapter 2: Experimental

In this chapter the chemicals, materials and techniques used in this thesis will be presented.

2.1 List of Chemicals

Chemical	Concentration / Purity	Supplier
Deionised water (H_2O)	Purity define by resistivity (R =18 MΩ cm^{-1})	On site Purite Water Purification System
Gold on Carbon (Au/C)	4 wt%	Dr. Stephen Price (Previous student)[1]
Isopropyl Alcohol ($CH_3CH_2OHCH_3$)	LC-MS	Fluka
Mercury (Hg)	99.999%	Fluka
Mercury(I) Sulfate (Hg_2SO_4)	Aldrich	98%
Nafion® in water	10 wt%	Sigma Aldrich
Nitrogen (N_2)	99.999%	BOC
Perchloric Acid ($HClO_4$)	70% (Suprapur®)	EMD Millipore
Platinum Black (Pt)	HiSPEC 1000	Alfa Aesar
Platinum on Carbon (Pt/C)	20 wt%	Johnson Matthey
Platinum on Carbon (Pt/C)	40 wt%	Johnson Matthey
Sulfuric acid(H_2SO_4)	Concentrated, trace metal analysis (18 mol dm^{-3})	Sigma Aldrich

2.2 Catalyst Electrode Preparation

Electrodes were prepared using two different methods: manually by painting a catalyst suspension onto a substrate, and by printing using an automated machine. Both methods will be described below.

2.2.1 Painting

To produce the electrodes, a catalyst "ink" was painted onto a carbon Toray paper. A catalyst powder typically Pt / C 20wt% was ground in a pestle and mortar for at least 15 minutes or until

no obvious lumps are present. 100 mg of this powder was mixed with 4 mL water, 100 µL IPA and 400 µL Nafion (10 % in H_2O) –the amount of Nafion is equal to carbon by mass. This suspension was then sonicated in an ultrasonic bath for 20 minutes.

This ink was then spread onto a disc of teflonated carbon Toray paper – using a paintbrush - until a desired loading of catalyst material was achieved, this was measured by mass after each coat was allowed to dry on a hot plate at 90 °C. Typical Values of catalyst loading in this work are between 0.25 and 1.5 $mg_{Catalyst}$ cm^{-2}. This would take multiple coats of paint. To minimise the effect of the direction of the paint stroke, the disc was rotated between every layer. Once the desired loading has been achieved the disc was then hot pressed at 175 °C and 10 MPa for 2 minutes protected by a layer of kapton on each side.

2.2.2 Auto Dispensed (City Technology)

In contrast, an automated method has also been used. This method has also been used to prepare electrodes for this work by collaborators (City Technology). This method uses a more viscous ink made of PTFE, platinum and a dispersing agent (Triton X), which is mixed using a Silverson mixer, the amounts are discussed in Chapter 5. This ink is printed using a mobile nozzle in a circular design as shown in Figure 7.

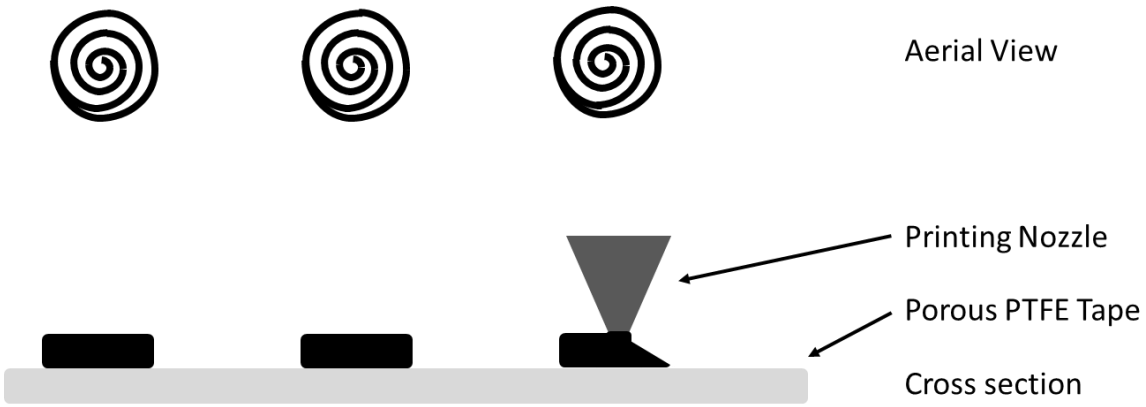

Figure 7. Schematic of electrode printing process. Not to scale, the PTFE layer is approximately 150 microns thick and the catalyst layer ranges from 50-100 microns in thickness. Each electrode is 15 mm in diameter.

Once the electrode material has been printed onto the sheet, the sheet was then heated in an oven at 300 °C. Once dry the electrodes were then pressed.

2.3 Electrochemical Methods

All cyclic voltammetry was conducted using an Autolab PGSTAT101 (including *in situ* potential hold experiments at the synchrotron), controlled using Nova 2.0 software. Impedance

measurements were conducted using a Biologic SP-150 potentiostat/galvanostat controlled using EC-Lab software.

2.3.1 Reference Electrode Preparation

In this work Saturated Mercury Sulfate Electrodes (SMSE) were used as reference electrodes. Two references were prepared in custom designed glassware, one of them is shown in Figure 8.

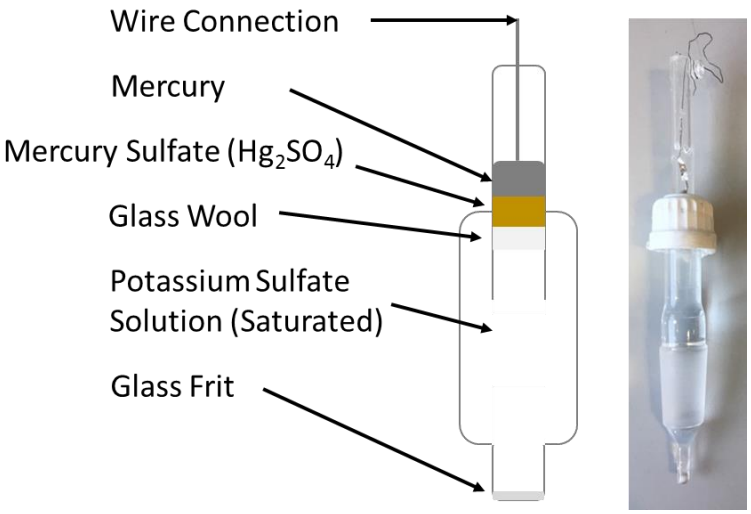

Figure 8. Schematic and picture of SMSE reference electrode. This is 10 cm in total length.

These electrodes were prepared by pouring the mercury into the void in the upturned electrode housing, enough to cover all of the wire connection. Above this, mercury sulfate (Hg_2SO_4) powder saturated with mercury (this was mixed in a pestle and mortar), was packed in to form a 5 mm layer using a wooden dowl. Care was taken to ensure no mercury broke through the layer. This was all sealed using glass wool, again a compact 5 mm layer. The glassware was then filled with saturated potassium sulfate solution and screwed together. The electrodes were left for 2 days before being tested *vs.* a hydrogen electrode (Gaskatel HydroFlex®). The potentials measured were 701 mV and 703 mV *vs*. SHE. The electrodes were routinely calibrated and solutions refreshed when necessary. A commercial Gaskatel HydroFlex® RHE electrode was used for some of the experiments.

2.3.2 Flooded Electrode Cell

Most of the laboratory based experiments were conducted in a three electrode cell as depicted in Figure 9. This design uses a reference electrode luggin capillary, which provides a well-defined point for sensing the potential near to the working electrode. A homemade gold wire loop

working electrode connection and a platinum gauze counter electrode are also used. The signal from the gold electrochemistry is only observable when no painted electrode is mounted. When an electrode is mounted the signal from the gold is swamped and less than the noise, due to the very large disparity in surface area. Although both sides of the painted electrode are in the solution, only one side has the catalyst layer on - the side facing down and near the luggin capillary. The cell was also temperature controlled via the water jacket around the electrolyte, which was regulated using a Grant thermostatic water bath pump.

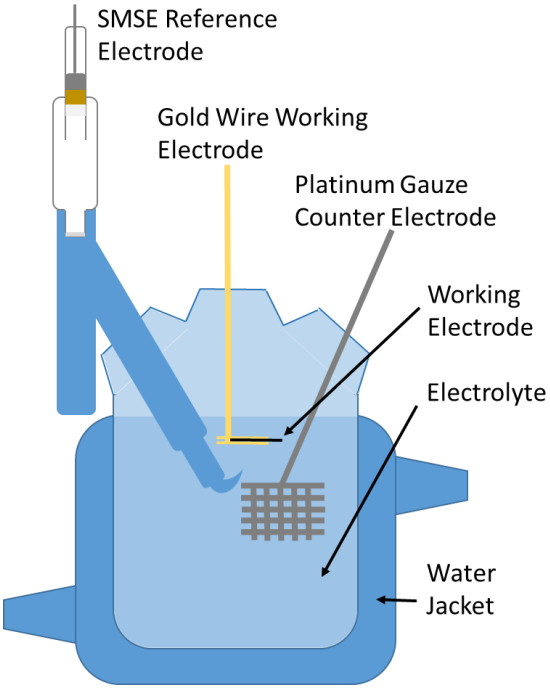

Figure 9. Schematic and picture of SMSE reference electrode

The electrolyte was purged with nitrogen (unless otherwise stated) and a constant stream of nitrogen was flowed over the electrolyte to ensure an oxygen free solution during measurements. To ensure all of the catalyst materials were electrochemically active, the electrodes were 'vacuum filled', which means they were placed in a beaker of deionised water and forced under by an upturned funnel. Then the beaker was placed in a vacuum chamber and the chamber evacuated. This process draws out the gas in the electrodes and ensures liquid fills all the pores of the electrodes. Electrolyte is not used in this process as a way of protecting the electrode, as there is no potential control at this stage.

2.3.3 *In Situ* XAS Cell

The cell shown below in Figure 10 was one that was used to mount discs of catalyst painted carbon paper electrodes while they are probed using X-rays at the synchrotron. The working electrode was a carbon paper-backed painted disc (11 mm) to which a contact was made using a

gold wire (0.1 mm, 99.99%, Sigma Aldrich) connection, which has been flattened. Then the Kapton window is fixed on top with the PTFE spacer ensuring even pressure and minimal pulsing of the window with the flow of electrolyte. The counter electrode was a platinum wire and the reference electrode is connected via an electrolyte filled PTFE tube and supports the homemade electrodes shown in section 2.3.1.[2,3]

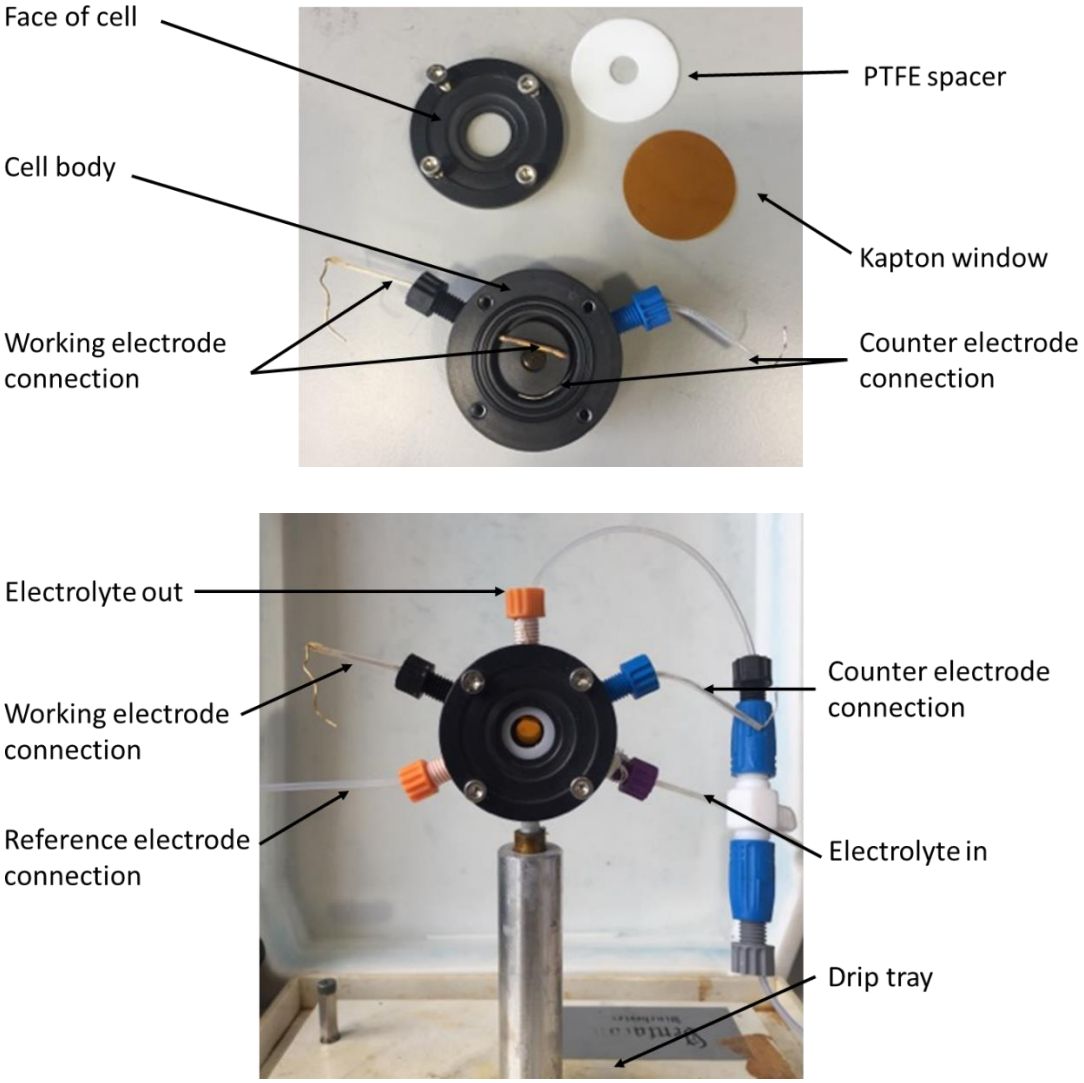

Figure 10. *In suit* electrochemical cell for XAS measurements. The diameter of the whole cell is 40 mm.

Electrolyte can be pumped through the cell via PTFE tubes shown in Figure 10 as electrolyte in (at the bottom of the cell) and electrolyte out (at the top of the cell) this configuration allows any bubbles formed in the cell to leave efficiently without disrupting the experiment. The cell is sealed with two O-rings (Viton) and a Kapton window, there is a PTFE spacer which reduced the pulsing of the window due to the pumping of electrolyte. Electrolyte was needed to be pumped, so a peristaltic pump (Masterflex) was used, as the cell volume is small (<10 ml) so gas bubbles forming can be an issue, as can electrolyte consumption. The cell is a bespoke design and is made by the in house mechanical workshop from 40% glass filled polyphenylene sulphide (this is a very

chemical resistant material, in particular it is acid resistant, which was essential for this work). A cross section of the cell is shown in Figure 11.

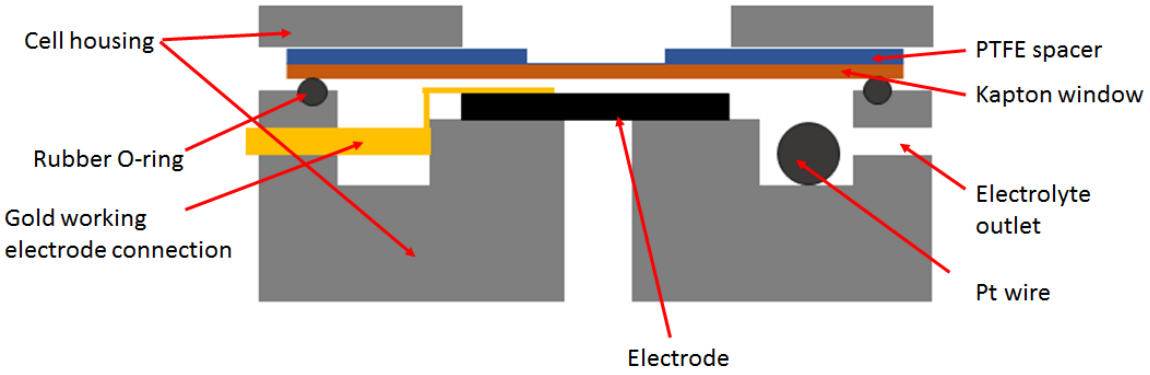

Figure 11. Schematic of the cross section of the *In suit* electrochemical cell for XAS measurements.

2.3.4 Cyclic Voltammetry

Cyclic voltammetry (CV) is one of the most common techniques in electrochemistry, and one that is repeatedly used throughout this work. CV is a method where the potential of the working electrode is cycled between an upper and lower limit, at a set rate, while the current is measured.

Figure 12 shows an example of a cyclic voltammogram of a platinum black coated electrode in 1 mol dm^{-3} sulfuric acid. The double layer charging region, where the current is small and constant, is between -0.3 V *vs* SMSE and +0.15 V *vs.* SMSE on the anodic sweep. There is a small redox peak in this region believed to be due to the carbon support degrading.[4] More positive than +0.15 V *vs.* SMSE oxygen absorbs onto the surface of the platinum. On the cathodic scan the oxygen stripping requires an overpotential and begins at +0.25 V *vs.* SMSE where there is a peak for surface oxide stripping observed around at +0.1 *vs.* SMSE. At potentials below to -0.35 V *vs.* SMSE hydrogen begins to be adsorbed onto the surface (forming Pt-H species), and there are two peaks are attributed to the difference in absorption energies of the two most abundant platinum crystal faces, (100) and (110). The double peak is replicated in the reverse potential direction at the same potentials.

The real surface area can be calculated from these cyclic voltammograms. It was assumed that the double layer charging current is the same for a hydrogen covered surface as it is for the polished Pt surface. Therefore, the baseline for the integration was taken as an extension of the double layer charging current between 0 V and -0.3 V *vs* SMSE. Then the area inside the two lines between -0.65 V *vs* SMSE and -0.3 V *vs* SMSE shown in Figure 12 is proportional to the charge

passed, and equal when divided by the scan rate. This area represents the hydrogen monolayer stripping charge (Q_{strip}).

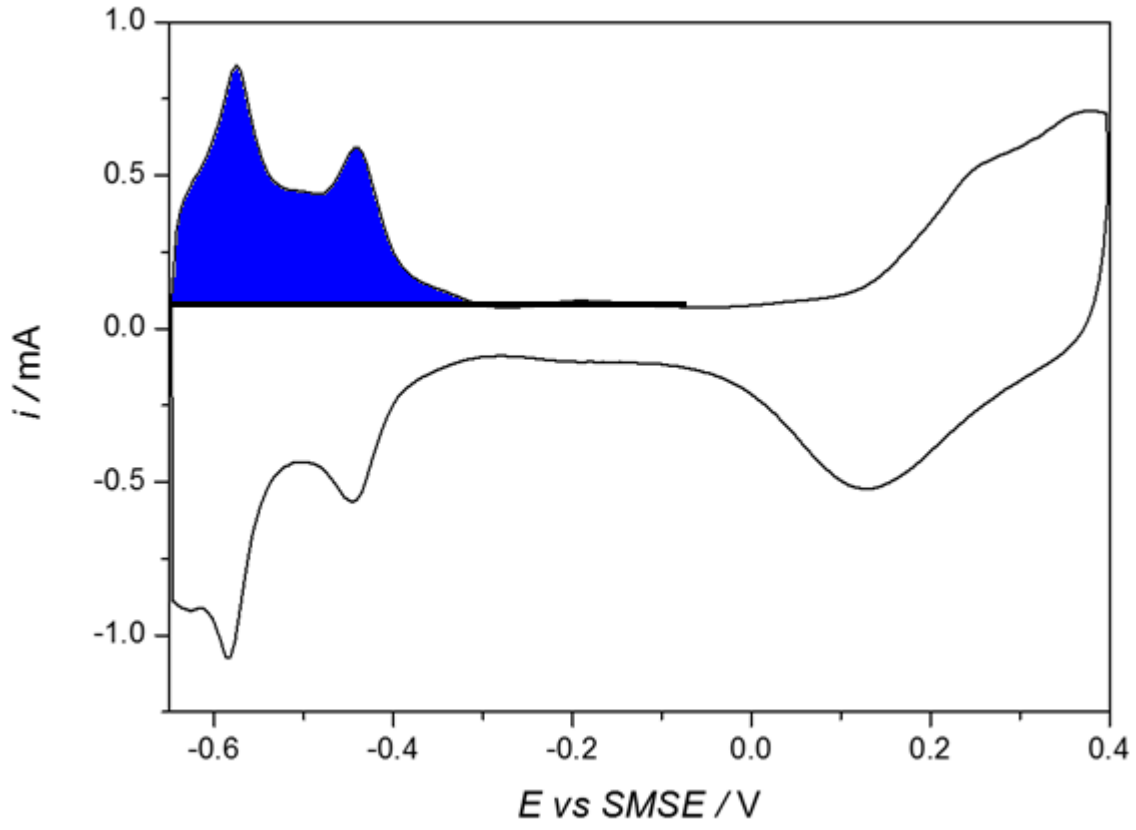

Figure 12. Cyclic voltammogram of a Pt black catalyst painted onto a carbon Toray paper button (11 mm diameter) with a Pt loading of 0.255 mg cm^{-2} in 1 mol dm^{-3} H_2SO_4 measured at a scan rate of 0.01 V s^{-1}. The electrochemical cell was purged with nitrogen gas

The hydrogen stripping peak is proportional to the real surface area. This is because the hydrogen forms a monolayer and this is limited by the real surface area (S_r), or electrochemically active surface area. The reaction, which involves a one electron transfer is shown in equation 8.

$$\boldsymbol{Pt - H \rightarrow Pt + H^{+} + e^{-}}$$

Equation 8

The value for conversion factor was taken from literature to be 210 µC cm^{-2}.[5] Equation 9 shows how the surface area (S_r) was calculated using the peak area (equal to the charge, Q_{strip}).

$$S_r = \frac{Q_{strip}}{conversion\ factor}$$

Equation 9

2.4 *Ex Situ* Sample Preparation

Due to the wavelength of visible light being around 10^3 nm, imaging anything on this scale or smaller is difficult with a traditional microscope. In place of visible light electrons can be used, as the wavelength of an electron can be much smaller and tuneable, depending on its kinetic energy. In this work the accelerating voltage of the electrons in the SEM was ~ 10^1 keV and in the TEM was ~ 10^2 keV, these electrons have a wavelength on the order of 10^2 pm and 10^0 pm respectively. Since the resolution of a microscope is half that of the wavelength of the radiation used, these microscopes can resolve much finer detail than an optical equivalent.

2.4.1 TEM

TEM samples were prepared by adding a very small amount catalyst powder to a vial with 3 mL of IPA. This was then sonicated in an ultrasonic bath for 10 minutes. 10 µL of the resulting suspension was pipetted onto a carbon coated 300 mesh copper grid (Agar Scientific), this was left to dry overnight. The TEM measurements were made using a FEI Tecnai T12 instrument with an accelerating voltage of 100 kV.

2.4.2 SEM and EDX

A FEI/Philips XL-30 Field Emission ESEM was used for the SEM and EDX measurements. Electrodes were prepared for SEM and EDX analysis by cooling with liquid N_2 and cutting with a scalpel, this exposed a cleanly cut cross section of the electrode such that the structure could be probed Figure 13 and Figure 14 show the improvement made by cooling the electrode prior to cutting. When the electrode was not cooled, the electrode material crumbles compared to the sheer cut when it has been cooled. The cut electrodes were then mounted onto SEM stubs using conductive double-sided sticky carbon tape (Agar Scientific).

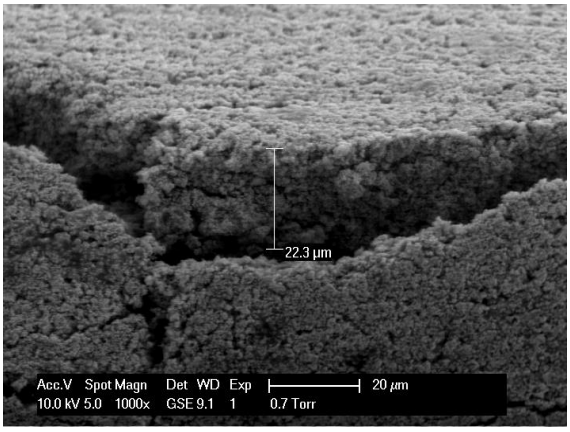

Figure 13. SEM image of electrode cross section cut with scalpel at room temperature

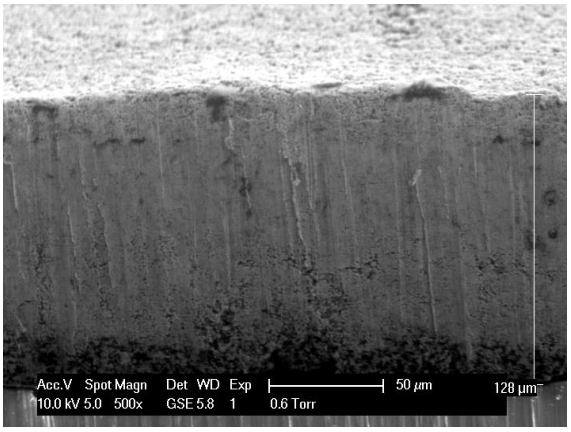

Figure 14. SEM image of electrode cross section cut with scalpel after liquid N_2 cooling

As the electrodes are backed with a porous PTFE tape they are non-conducting therefore the SEM was run in wet mode, meaning there is an atmosphere of water vapour in the chamber (also known as environmental mode). This reduces the charging of the sample being measured. The accelerating voltage of the electron gun was 10 kV.

2.4.3 XAS Pellet Preparation

Pellets were prepared to undergo X-ray Absorption Spectroscopy (XAS) by pressing a mixture of sample material and boron nitride (BN) in a pellet press. The press makes circular pellets of area 0.72 cm^2. The amount of sample material required was calculated by taking the area of the sample holder and dividing this by the total X-ray cross section of all absorbing atoms at a value ~100 eV above the edge being probed. This should give a change in absorbance across the transition of 1. In addition to the sample material boron nitride was added to make the total mass 150 mg. The combined material was ground until homogenous and then pressed using a Specac Pellet Press to 5 ton for 3 minutes.

2.5 References

1 S. W. T. Price, Enhanced Structural Characterisation of Supported Catalysts, University of Southampton, 2011.

2 Wise, A. M. Characterisation of Bimetallic Alloy and Core-Shell Electrocatalysts, University of Southampton, 2012.

3 Price, S. W. T.; Speed, J. D.; Kannan, P.; Russell, A. E. J. Am. Chem. Soc. 2011, 133 (48), 19448–19458.

4 Kangasniemi, K. H.; Condit, D. A.; Jarvi, T. D. J. Electrochem. Soc. 2004, 151 (4), E125–E132.

5 J. Bett, K.Kinoshita, K. Routsis, P. S. J. Catal. 1973, 29 (1), 160–168.

Chapter 3: pH effects on Platinum Electrochemistry

In this chapter the effect of very low pH on the cyclic voltammetry of platinum is reported, specifically the oxidation of platinum and hydrogen adsorption features. At very low pH an apparent non-Nernstian behaviour of the hydrogen adsorption and oxide formation features in the voltammograms was observed. Analysis of the data in this chapter was in response to a problem presented from an industrial partner, where the electrolyte of sulfuric acid containing gas sensors would vary based on environmental conditions. The solution presented resulted in a patent, where the concentration of the solutions could be tracked using features of the Pt voltammogram.[1]

3.1 Introduction

The fundamental understanding of how adsorbates interact with a platinum surface is paramount to understanding how gas sensors, fuel cells, electrolysers and other electrochemical devices operate.[2–4] In particular, the adsorption of hydroxide ions and hydrogen atoms onto a platinum surface in an aqueous environment is central to the reactions of hydrogen evolution and oxidation, oxygen reduction, and the oxidation of carbon monoxide.[5] This chapter will investigate how these processes are affected by the pH the electrolyte. This is of particular importance to gas sensors as they are exposed to air, therefore the concentration of hygroscopic electrolytes (such as sulfuric acid) will vary based on sensor use. Cyclic voltammetry of platinum electrodes will be used to determine the electrolyte concentrations.

3.1.1 Environmental Gas Sensor Problem

Commercial gas sensors that use sulfuric acid have the complication that water can evaporate from or become absorbed by the electrolyte. This process is dependent on the environmental conditions in which the sensor is being used. M. Willett highlighted this issue in 2014, with calculations of the lifetime of gas sensors versus temperature and humidity of the environment they are used in, this is shown in Figure 15.[6] The lifetimes range from 6 months to 4 years, which is a very wide range. These values are based only on electrolyte factors, other issues such as electrode degradation will also have an impact.

As the sensors absorb water from the environment in a high humidity environment, the electrolyte becomes more dilute and occupies more space. This has (in extreme cases) caused sensors to burst. In very dry environments the electrolyte concentration increases, accompanied by an increase in the electrolyte resistance, and connection to the electrodes may be lost. It is also known that key operational parameters such as the response time and sensitivity degrade as a function of water loss.[7] In both cases the solubility of the analyte gases are affected. To improve sensor performance the work in this chapter looks to monitor changes in the electrolyte concentration through monitoring the peaks on a platinum cyclic voltammogram.

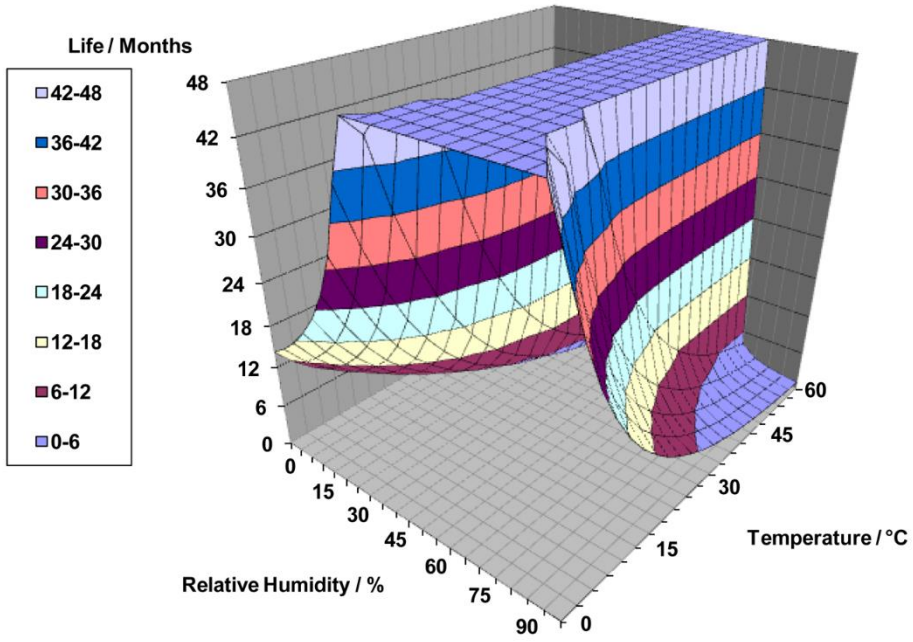

Figure 15. Lifetime predictions for continuous operation at selected temperatures and relative humidities produced by M.Willet.[6]

As previously mentioned, this work also has an impact away from the world of gas sensors. Optimisation of fuel cells and electrolysers also rely heavily on a fundamental understanding of how adsorbates interact with a platinum surface.

3.1.2 Electrochemical Theory

In this work, the peak positions of a pair of redox processes are investigated as a function of pH. The surface oxidation forming a surface oxide and surface reduction to form a hydrogen adsorbed layer will be presented. There are longstanding and well understood relationships between the peak potential of a reaction and the activity of reactants and products. Equation 10 displays the Nernst equation, which can be rearranged to describe this relationship.

$$E = E^{\ominus} - \frac{RT}{nF} lnQ_r$$

Equation 10

Where *E* is the half-cell reduction potential, $E^{\ominus}$ is the standard half-cell reduction potential, *R* is the universal gas constant 8.314 J K^{-1} mol^{-1}, *T* is the temperature, *n* is the number of electrons transferred, *F* is Faraday's constant (96485 C mol^{-1}), Q_r is the reaction quotient. If you input the value of 298 K for temperature this equation can be rewritten as Equation 11.

$$E = E^{\ominus} - \frac{59\ mV}{n} logQ_r$$

Equation 11

Equation 12 shows a generic reaction involving both electron and proton transfer for which the reaction quotient (Q_r) is shown in Equation 13.

$$bOx + ne^- + cH^+ \rightleftharpoons dRed$$

Equation 12

$$Q_r = \frac{{a_{Red}}^d}{{a_{Ox}}^b {H^+}^c}$$

Equation 13

By substituting the reaction quotient for this generic reaction into the Nernst equation you get Equation 14:

$$E = E^{\ominus} - \frac{59\ mV}{n} log \frac{{a_{Red}}^d}{{a_{Ox}}^b {a_{H^+}}^c}$$

Equation 14

And by separating the numerator and denominator of the logarithm this equation can presented as shown in Equation 15:

$$E = E^{\ominus} - \frac{59\ mV}{n} d\ log\ (a_{Red}) + \frac{59\ mV}{n} b\ log\ (a_{Ox}) - \frac{59\ mV}{n} c\ p\mathrm{H}$$

Equation 15

Equations 14 and 15 describe the link between the activity of the reduced species, the oxidised species and the potential at which the process is observed. The activity of every product and reactant in the reaction has an effect on the potential at which it occurs. If a proton is the oxidised

species in the reaction one would expect, as the pH increases, the potential of the reaction to decrease. This is shown by the final term in Equation 6 and describes the pH dependence of this generic electrochemical reaction. If there was a reaction as shown in Equation 16, the pH dependence of this one proton one electron reaction there be -59 mV per pH unit (the activity of a solid is assumed to be 1).

$$Pt + H^+ + e^- \rightarrow Pt - H$$

Equation 16

Since in Equation 15 the coefficient for the number of protons "c" is a numerator of the fraction and the number of electrons "n" is a denominator. To explain any deviation of the gradient from -59mV per pH unit these values would have to be different to each other.

3.1.3 Platinum Surface Adsorbate pH Dependence

A collection of papers from the Koper group have investigated the pH dependence of features in the cyclic voltammogram of platinum related to water dissociation products, starting with a detailed overview of the so called hydrogen region of the platinum voltammogram.[5,8,9] Their work covers a wide, and relatively mild (pH 2-12) range. It was reported that there was a non-trivial pH effect, the expected one proton one electron reaction scheme (Equation 16) could not explain the observed results. With ~-50 mV per pH unit shift in the hydrogen adsorption and desorption peaks being observed, which is a significant deviation from 59 mV pH^{-1}. A number of platinum electrodes were used (different single crystals and polycrystalline surfaces) all observing a similar 'non-Nernstian' behaviour.[9] The explanation for the observed dependence was that the simple process shown in Equation 16 is not sufficient to describe these peaks and more species are involved.

Species such as surface OH^+_{ads} would allow for additional electrons in the reaction leading to a disparity in electrons and protons, which as discussed in the previous section (3.1.1) causes variation in the gradient of a peak position versus pH plot.

Evidence for the presence of OH^+_{ads} goes back to 1973 when Kozlowska *et al.* distinguished the overlapping peaks in the oxide region of the platinum voltammogram, the first of these peaks was attributed to a partial monolayer of adsorbed OH (0.8-0.9 V *vs.* RHE).[10] The following two peaks were assigned to the rest of the monolayer being adsorbed, followed by a place exchange reaction with a multi-layer oxide product.[11–13] The place-exchange mechanism has been further investigates by Nagy *et al.* using X-ray scattering experiments.[14]

Work has been conducted by Huang *et. al.* in which the onset of platinum oxidation has been followed using surface enhanced Raman spectroscopy (SERS).[15] Their work discusses the oxidation of single crystal (111 and 100) platinum surfaces, and concludes that the first species formed, between 0.4 and 0.9 V *vs.* RHE (0.1 M $HClO_4$), is Pt – OH. Such results support the idea that OH^+_{ads} could displace the protons from the surface accounting from the variation in the pH dependence.

3.1.4 Derivative Voltammetry

Since some of the features that will be investigated are very subtle derivative voltammetry will be used. In 2012, Murthy and Manthiram discussed the advantages of using derivative voltammetry, which include but are not limited to: eliminating capacitive currents, so focus is brought to Faradaic processes; as the analysis is more sensitive to changes, onset potentials are easier to determine; and allowing closely placed peaks or shoulders to be resolved from each other.[16] For these three main reasons derivative voltammetry will be used to analyse the voltammograms in this chapter.

Capacitive currents are eliminated as these are relatively constant values, therefore there will be no (or very little) change caused by these processes. Once the derivative of the current vs voltage curve is taken, changes to the current are highlighted, this shows the Faradaic processes, and subtle peaks and shoulders are easier to resolve, as the background currents are removed. There are Figures in section 3.3.1 showing this process.

3.1.5 pH and Hammett Acidity Function

pH is a scale on which it is possible to quantify the acidity or basicity of a solution. Sørensen introduced the concept and the original method of determination was using coloured indicator solutions with a precision of half a pH unit.[17] In 2002 Buck *et. al* published the current standards for the International Union of Pure and Applied Chemists IUPAC, where they define pH as in Equation 17:[18]

$$pH = -log_{10}(a_{H^+})$$

Equation 17

Where a_{H^+} is the activity of the hydrogen ion. The activity is dependent on the molarity and activity coefficient, and at dilute concentrations the activity coefficient is assumed to be one. At higher concentrations the activity coefficient deviates greatly from one. In 1932 Hammett proposed an extension to the pH scale, the Hammett Acidity Function.[19] This function describes the proton donating ability of highly acidic solutions better than pH. As these values have been

determined experimentally, all factors, including ionic strength, are accounted for. This function was re-evaluated by Jorgenson and Hartter who found that below 10 mol dm^{-3} the model needed no modification.[20] This function as it is empirically derived takes into account all factors affecting the proton donating ability of the solution, therefore as long as the same solutions are used no other corrections need to be accounted for. pH values less than zero are very important as it is in these solutions that gas sensors such as those manufactured by City Technology work.

3.2 Experimental

The electrodes that have been used are City Technology printed electrodes, prepared as described in Chapter 2. They have a loading of 8 mg per electrode (20% PTFE and 80% platinum black). The electrodes have been flooded and measured in the glass cell also as described in Chapter 2.

EMD Millipore Suprapur® Perchloric acid 70% was used to prepare the perchloric acid solutions and all the glassware was cleaned thoroughly before use to ensure no contamination. All glassware was cleaned with Purite Water Purification System 18 MΩ cm^{-1} water at least three times, and again with the acid of interest. Concentrated, trace metal analysis (Sigma Aldrich, 18 mol dm^{-3}) sulfuric acid was used for the sulfuric acid solutions. All measurements were versus a RHE reference electrode, and a platinum gauze was used for the counter electrode.

Since the RHE is based on the one electron one proton reaction between hydrogen and protons as discussed in the introduction, it would be expected to shift with pH by 59 mV per pH unit. Therefore, during the analysis of this work a 59 mV per pH unit shift has been applied, so the results can be considered versus SHE (standard hydrogen electrode), the standard for electrochemistry.

The voltammograms reported here were analysed using the Origin 2017 software package. The differentiation tool was used sequentially to yield the first and then second derivative of the current *vs.* potential. A 20 point Savitzky–Golay smoothing function was applied at each stage, this is a type of moving average smoothing function where a low order polynomial was fitted to the data via a least squares method. This makes sure the data is not distorted more than necessary. Smaller ranges (<20) were tried but didn't smooth the data enough for a clear zero point to be determined on the second differential graph. The peak fitting was also performed using Origin 2017 and the Multiple Peak Fit tool and the Gaussian peak function.

3.3 Results and Discussion

3.3.1 Platinum Cyclic Voltammogram Reference Points

The Platinum CV was described in section 2.3.4. For this chapter the focus will be on the "strong" hydrogen desorption peak at around -0.45 V *vs.* SMSE (marked by the red line) and the inflection of the oxide formation peak at around 0.25 V *vs.* SMSE on the anodic sweep of the voltammogram (marked by the red dot in the circle), shown in Figure 16.

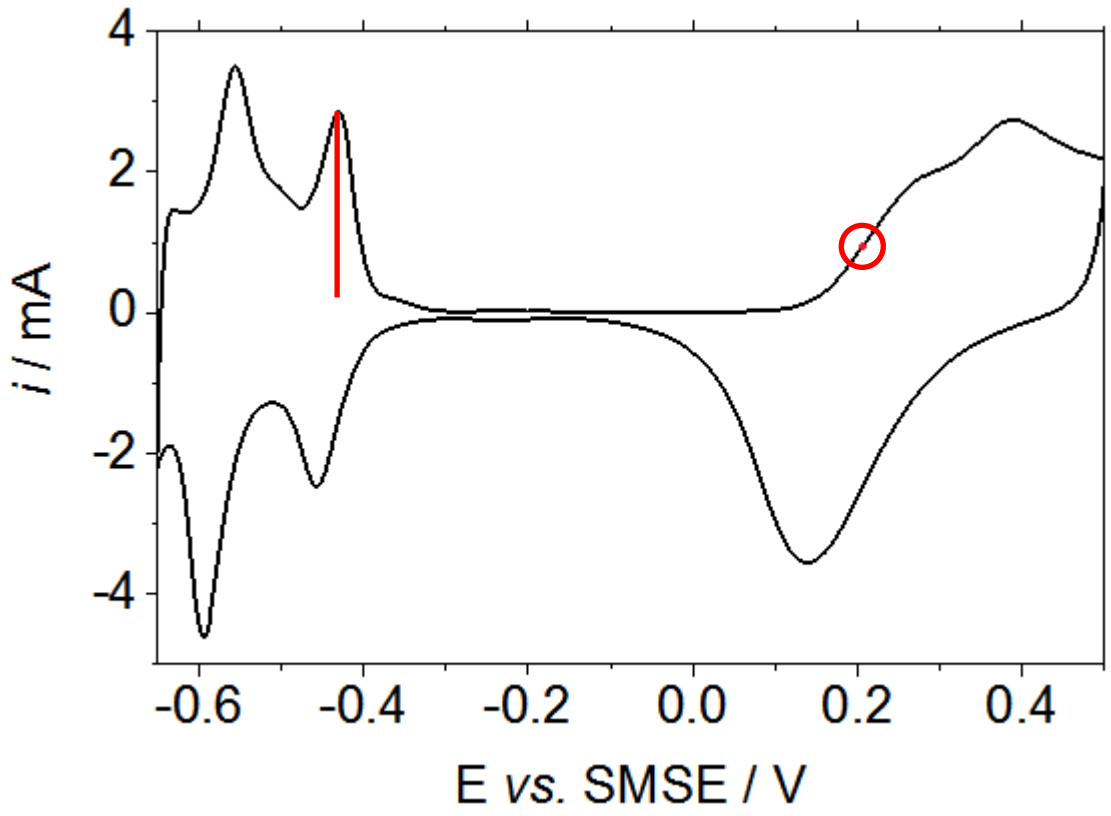

Figure 16. Cyclic voltammogram of a City Technology printed Pt black (8 mg loading) electrode in 3 mol dm^{-3} H_2SO_4 measured at a scan rate of 2 mV s^{-1}. The cell was kept at 25°C with a thermostatic water bath. The electrochemical cell was purged with nitrogen gas for 15 minutes before the experiment and gas was supplied over the solution during the measurement. The above voltammogram is the second cycle. The red dot in the circle approximately shows the first inflection point, and the re line point out the "strong" hydrogen desorption peaks.

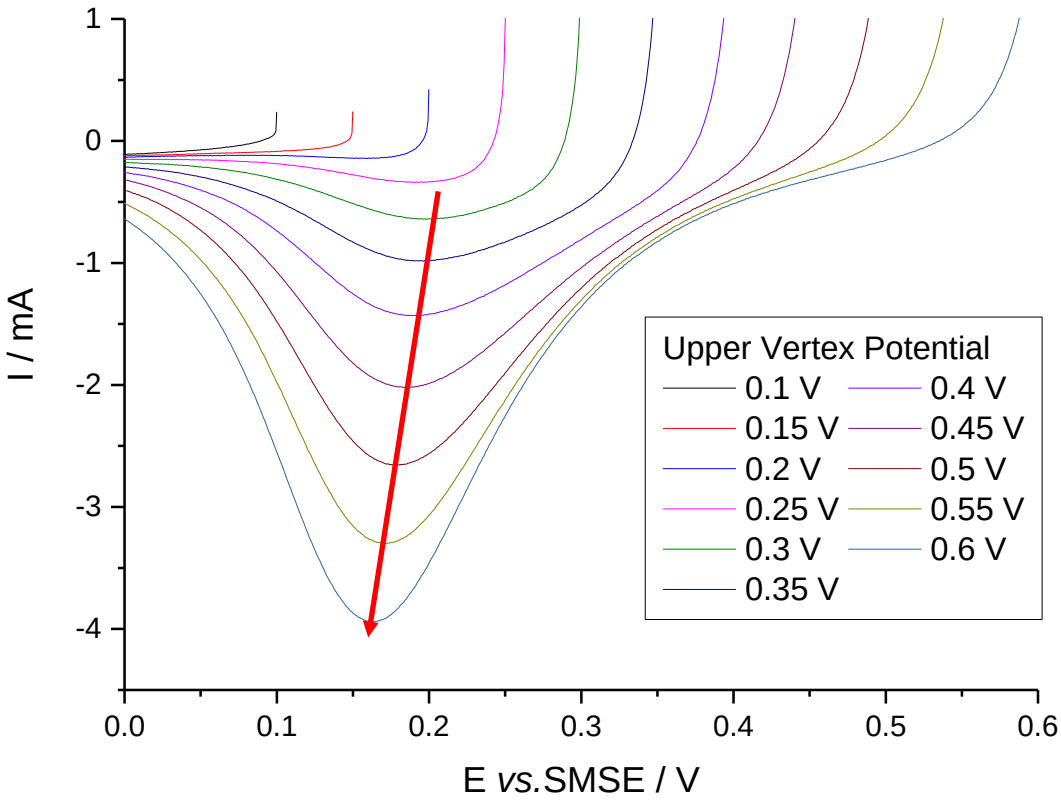

Figure 17. Cathodic sweep showing the platinum oxide reduction wave while increasing the upper limit of the voltammogram in 5 mol dm^{-3} sulfuric acid using a SMSE reference electrode. Scans were run at 2 mV s^{-1}. The red arrow shows the change of the peak with increasing vertex potential.

Figure 17 shows the oxide stripping region of the cathodic sweeps of voltammograms where the upper vertex was increased by 50 mV increments. It should be observed that the platinum oxide stripping peak shifts by approximately -50 mV. This shift is the reason why the oxide stripping peak is unsuitable to be used as a point of reference on the voltammogram, as it would require a defined upper potential limit to achieve. The total shift in the peak with a concentration change in the electrolyte between (1 and 10 mol dm^{-3}) and a fixed upper vertex limit was ~100 mV (shown in Figure 19). So the shift observed in Figure 17 and illustrated in Figure 18, where the peak potential is plotted *vs.* the upper vertex potential is much too large to be overlooked, as it could give false values.

The platinum oxide reduction wave was initially considered as a point of interest. This was rejected as a reference point for two main reasons; the peak potential of the oxide stripping is dependent on the anodic limit of the voltammogram, and the reaction involves many different PtO_x species being reduced.

Therefore, the first platinum oxidation inflection point was chosen as the reference point. By choosing the first inflection point, the reaction being observed can be isolated to the first step of platinum oxide formation (shown in Figure 16 by the red circle). There is more reproducibility with

this point as it does not depend on the upper vertex of the scan like the stripping peak. This point was chosen as the point at which the second derivative of the current is equal to zero, which is simple for an automated process to determine.

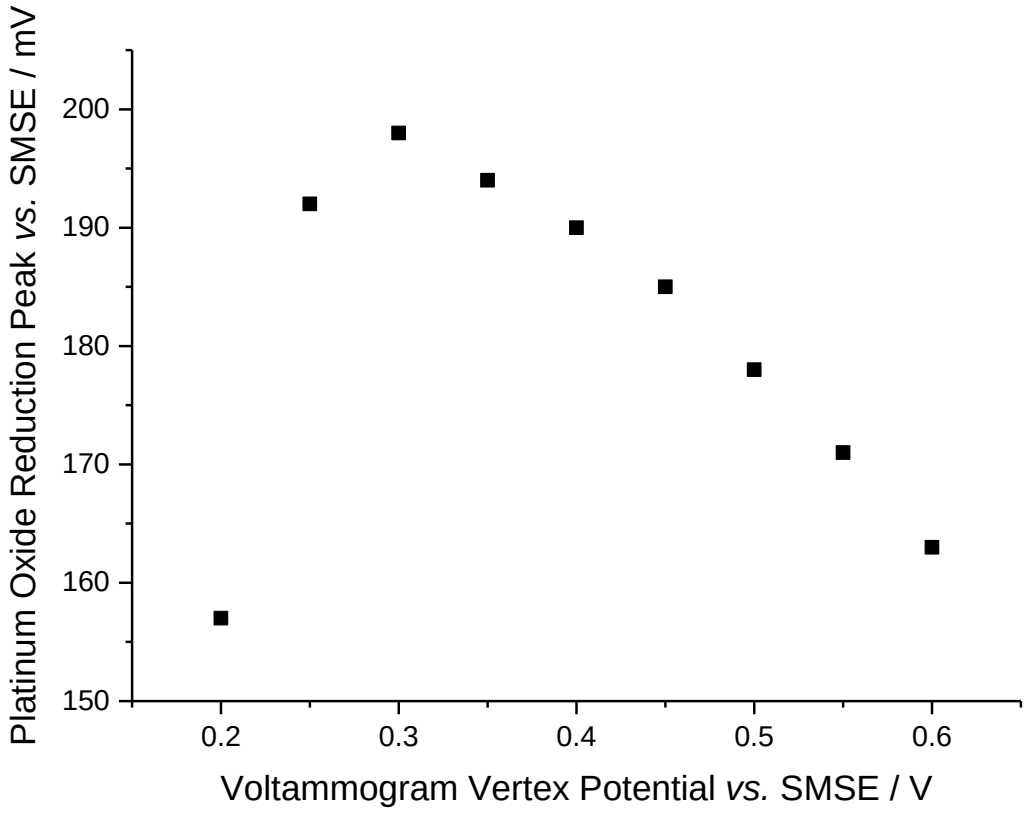

Figure 18. A plot of the platinum oxide reduction peak potential as a function of the upper vertex of the voltammogram. Voltammograms shown in Figure 17 (results for 0.1 and 0.15 are omitted as there was no zero point observed in the derivative voltammograms).

Since the particular industrial use for this work is in a two electrode cell with a quasi-reference electrode, platinum electrodes are used as both a counter and reference electrode, a single point on the voltammogram was unsatisfactory for calculating the solution concentration, as the reference electrode is not at a fixed potential. This is because the reference electrode will drift with solution and other environmental factors such as temperature. For this reason, the second hydrogen desorption peak was used as a second point of reference on the voltammogram. This point was chosen as the reaction being investigated is well understood and the peak potential shifts a very small amount with pH *vs.* RHE (~10 mV per pH unit) as discussed by Gisbert *et al.* and der Niet *et al.*[8,9]

Cyclic voltammograms were carried out in a standard three electrode cell. Figure 19 shows the voltammograms of a platinum black seven sulfuric acid solutions from 1 mol dm^{-3} to 10 mol dm^{-3} measured at a scan rate of 2 mV s^{-1} using a platinum gauze counter electrode and a saturated mercury sulfate reference electrode. The most obvious points to note are the consistent shift in

platinum oxidation wave to higher potentials with a greater concentration of electrolyte, and the more static nature of the hydrogen desorption features. These two observations make the basis for this chapter.

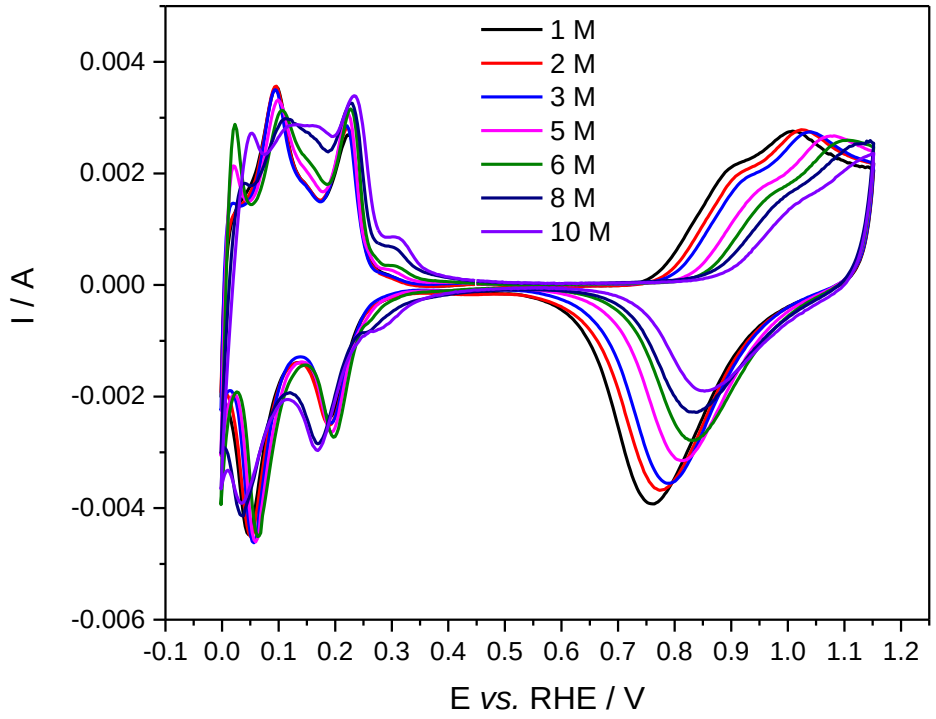

Figure 19. Voltammograms of a platinum black electrode in seven sulfuric acid solution from 1 mol dm^{-3} to 10 mol dm^{-3}. Counter electrode was a platinum gauze and reference electrode was a RHE. The cell was kept at 25°C with a thermostatic water bath. The electrochemical cell was purged with nitrogen gas for 15 minutes before the experiment and gas was supplied over the solution during the measurement. The above voltammograms are each the second cycle.

Looking at the hydrogen desorption features there are many subtle changes, but the peak positions of the two sharper desorption peaks shift only a small amount. There is the increase in intensity of the peak between the two sharpest, around 0.15 V *vs.* RHE, which has been observed by Lezna *et al.*. Lezna *et al.* also observed a growing peak with concentration of electrolyte more positive of the hydrogen features.[21] The small shoulder peak at 0.3 V *vs.* RHE was attributed to (bi)sulfate adsorption by Kolics, it is expected that it would grow with increasing concentration of (bi)sulfate.[22]

The inflection point of the platinum oxidation wave was selected as a point of reference. This point has been determined by the peak of the first derivative, or the point at which the second derivative is zero (as this was found to be more reproducible).

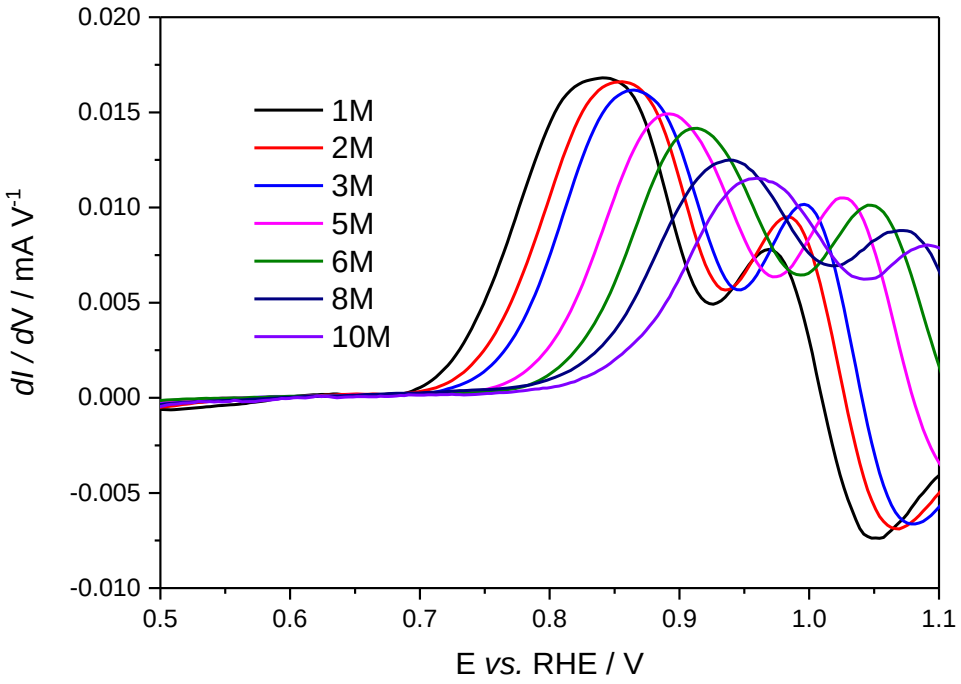

Figure 20. Plot of the 1st derivative voltammogram for a range of concentrations of sulfuric acid. Counter electrode was a platinum gauze and reference electrode was a RHE. The cell was kept at 25°C with a thermostatic water bath. The electrochemical cell was purged with nitrogen gas for 15 minutes before the experiment and gas was supplied over the solution during the measurement. The raw voltammograms were each the second cycle.

Figure 20 shows a plot of a section of the first derivative of the voltammograms shown in Figure 19, the section is from the anodic sweep between -0.2 until 0.5 V *vs.* SMSE. It is clear from this graph that the first peak is shifting noticeably with concentration of the electrolyte. To quantify this shift, the second derivative has been taken and plotted in Figure 21, where the point at which the lines cross zero are clear (shown as red circles in Figure 21). The data in Figure 21 has been cut off past the zero point to aid the visual representation, as the plots overlap each other.

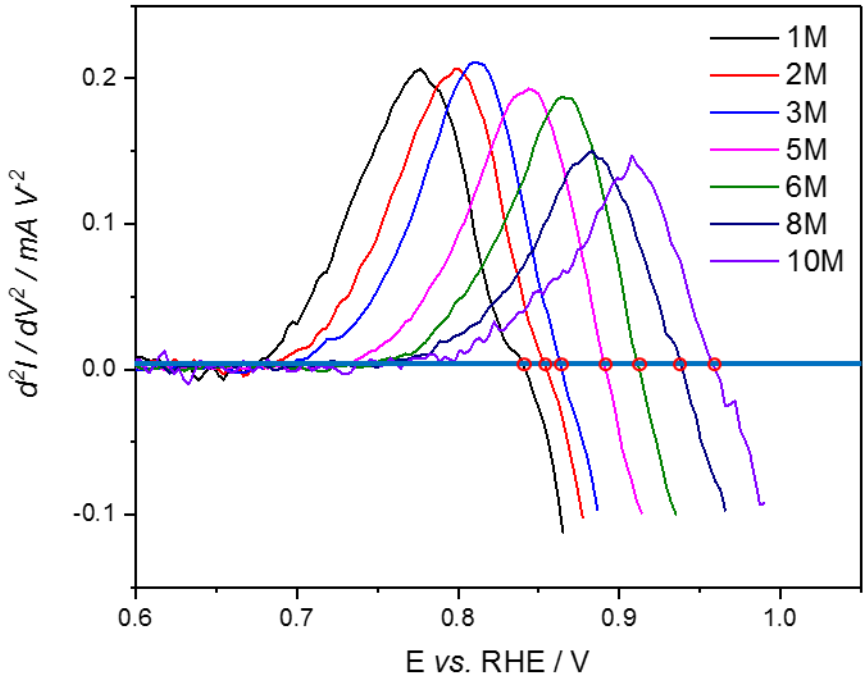

Figure 21. Plot of the 2nd derivative voltammogram for a range of concentrations of sulfuric acid. The blue line is equal to zero and the red dots show the points measured. Counter electrode was a platinum gauze and reference electrode was a RHE. The cell was kept at 25°C with a thermostatic water bath. The electrochemical cell was purged with nitrogen gas for 15 minutes before the experiment and gas was supplied over the solution during the measurement. The raw voltammograms are each the second cycle.

3.3.2 Platinum Cyclic Voltammogram – Perchloric Acid

Although sulfuric acid is the electrolyte of choice, percholoric acid will also be studied. Sulfuric acid has effects from sulfate interaction with the surface as shown in section 3.3.1, perchloric acid is considered to have a non-coordinating anion. Gloaguen discussed the role of anions, in particular that the hydrogen peaks are more pronounced in the presence of sulphate over perchlorate.[23] Figure 22 shows the voltammograms of a platinum black electrode in seven perchloric acid solutions from 1 mol dm^{-3} to 10 mol dm^{-3} measured at a scan rate of 2 mV s^{-1} using a platinum gauze counter electrode and a RHE reference electrode. The most obvious points to note are the consistent shift in platinum oxidation wave to higher potentials with a greater concentration of electrolyte (and similarly the platinum oxide reduction wave), and the less significant shift of the hydrogen features.

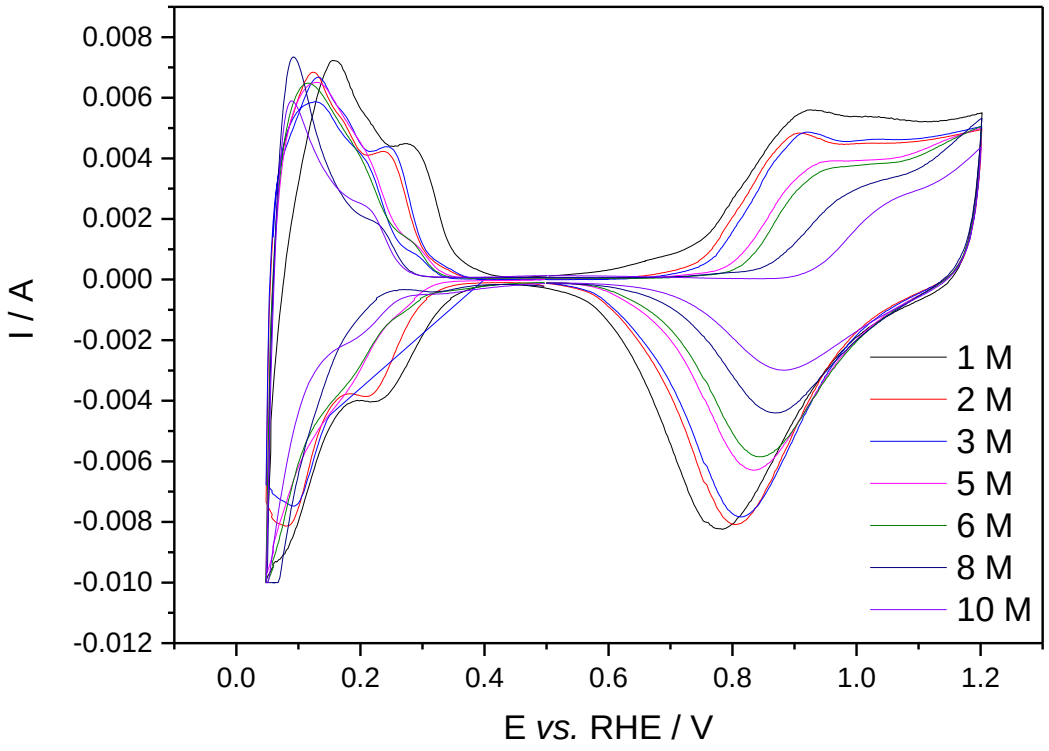

Figure 22. Voltammograms of seven perchloric acid solution from 1 mol dm^{-3} to 10 mol dm^{-3}. Counter electrode was a platinum gauze and reference electrode was a RHE. The cell was kept at 25°C with a thermostatic water bath, the scans were run at 5 mV s^{-1}. The electrochemical cell was purged with nitrogen gas for 15 minutes before the experiment and gas was supplied over the solution during the measurement. The above voltammograms are each the second cycle.

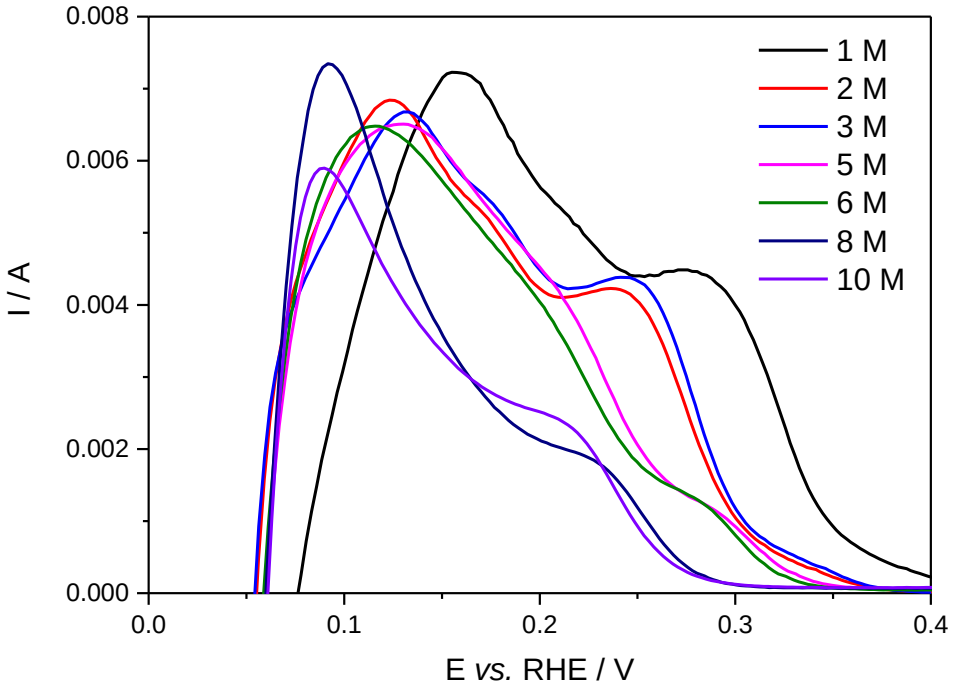

Figure 23. Cathodic sweep of voltammograms from Figure 22 between -0.05 V and -0.4 V vs. RHE

Figure 23 shows in more detail the hydrogen desorption peaks of the voltammograms. It is worth noting that the features are not well defined at high concentrations of acid, in part due to overlap from the oxidation of evolved hydrogen gas. This is more of an issue at higher concentrations as the evolution of hydrogen gas requires a lower overpotential in these solutions, meaning more is produced. It is also worth noting that although the hydrogen features do vary with potential, the change in this peak position with solution concentration is small, at least compared to the changed previously seen in the platinum oxidation shown in Figure 22. The peak potentials were plotted versus the pH (using the standard definition of pH and assuming a_{H20}=1) and the Nernst equation can then be applied to calculate the ratio of protons and electrons in the electrochemical process (shown in Figure 25). It can be observed that the trend is linear (R^2 of 0.88, ignoring the anomalous point for 6 mol dm^{-3}) for the strong peaks. The point for the 6 mol dm^{-3} solution has very subtle peaks as a result is was hard to isolate the strong hydrogen peak for this voltammogram (shown in Figure 24, where the 6 mol dm^{-3} is compared to 2 mol dm^{-3}). The linearity for the weak peaks is much less strong with an R^2 value of only 0.49. The gradients for these plots are 61 and 38 mV pH^{-1} for the strong and weak peaks respectively, which when converted onto the SHE scale, is 2 and -21 mV pH^{-1}. These values are not in agreement with previous work where approximately 10 mV pH^{-1} has been reported.[9] It would mean there is no pH dependence of the strong peak, and the reaction for the weak peak would have 3:1 ratio of protons to electrons, which would be hard to explain.

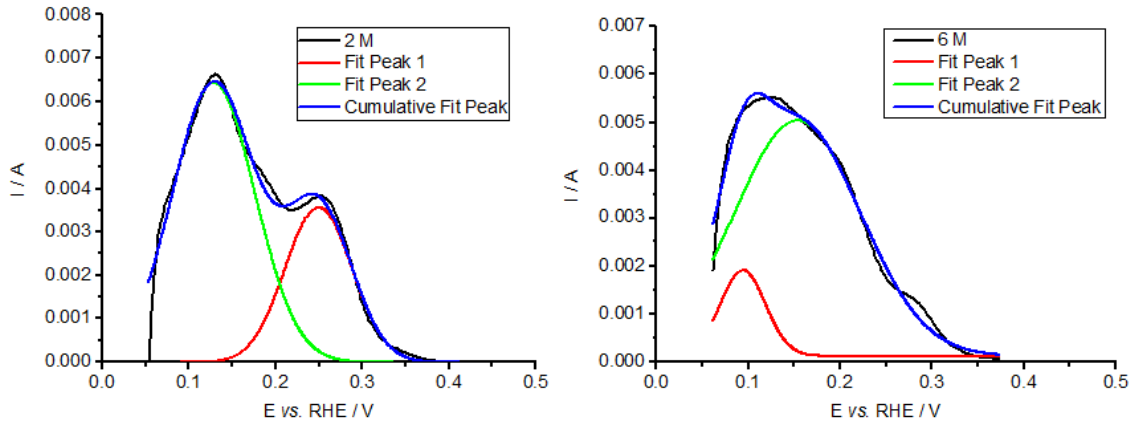

Figure 24. Shows the peak fitting for two of the voltammograms on the left 2 mol dm^{-3} and on the right 6 mol dm^{-3}.

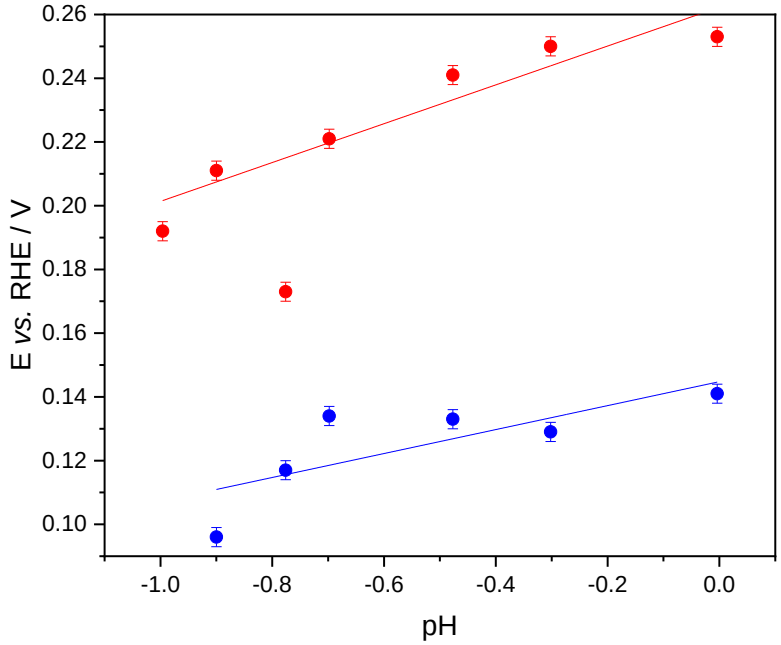

Figure 25. Plot showing the relationship between the hydrogen peaks and pH of the perchloric acid electrolyte. Blue dots are the weak peaks and the red dots are the strong peaks.

The relationship between the oxide inflection point and the pH is even more confusing. Figure 25 shows two clear regions that have vastly different gradients. The region from pH 0 to -0.8 has a gradient of -79 mV pH^{-1} and the region from -0.8 to -1 has a gradient of -541 mV pH^{-1}, when converted onto the SHE scale this becomes -600 and -138 mV pH^{-1}. Meaning that in the pH range from 0 to -0.8 the reaction would have 2.3 electrons per proton, but in the region more negative than -0.8 there would be 10 electrons per proton in the reaction which is very unlikely.

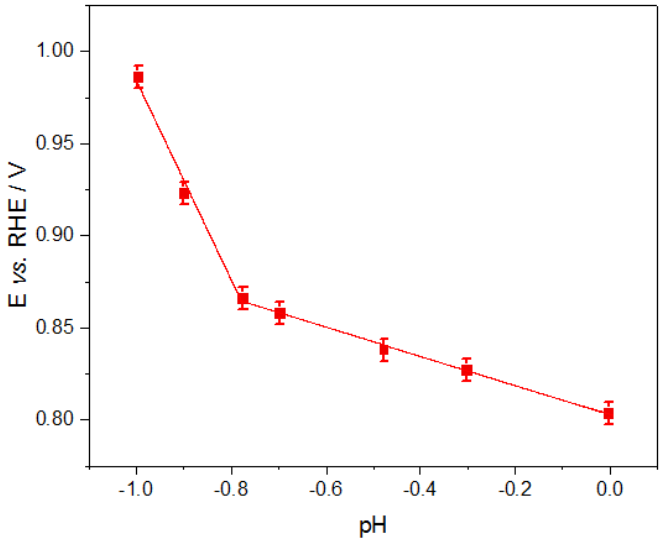

Figure 26. Plot showing the relationship between the platinum oxide inflection point and pH of the perchloric acid electrolyte.

In order to explain these results, the resistivity of the solution was investigated. Figure 27 shows the resistivity of both perchloric and sulfuric acid (sulfuric acid was included as it is used in

experiments later in the chapter). Both acids exhibit resistivities between 3 and 1.25 Ω cm, although based on the maximum current drawn in any of the voltammograms and the resistance measured in the solution of highest resistivity the IR drop was only calculated to be 4 mV, leading to the greatest variation in IR drop to be ~2 mV. This was based on the luggin capillary being 1 cm from the working electrode. This effect was considered to be negligible and not the cause of the observed irregularities.

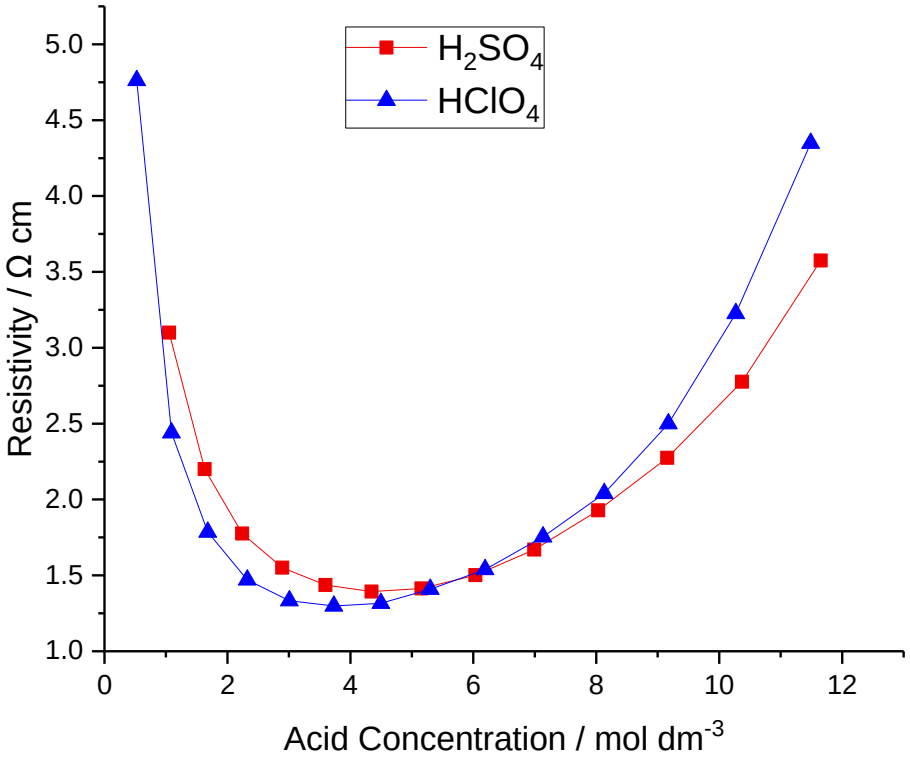

Figure 27. Shows how the resistivity of perchloric acid (blue) and sulfuric acid (red) varies as a function of concentration.[24,25]

3.3.3 Application of Hammett Acidity Function

The pH calculations used in Figure 25 and Figure 26 assumed that the activity coefficient of the protons is equal to 1. This assumption is only valid in dilute solutions. In more concentrated solutions of acid the Hammett acidity function (H_0) should be used in place of pH and is a much better descriptor of the proton donating ability of the solution.[19,26] H_0 being the empirically determined activity of protons for these solutions. Figure 28 shows how the Hammett acidity function varies relative to the concentration of perchloric acid, highlighting the need for much more negative values (compared to pH) to accurately describe the proton donating ability of the more concentrated solutions (the H_0 values have been taken from Paul and Long's work in 1957).[27] It is worth noting that H_0 is not linear function of acid concentration.

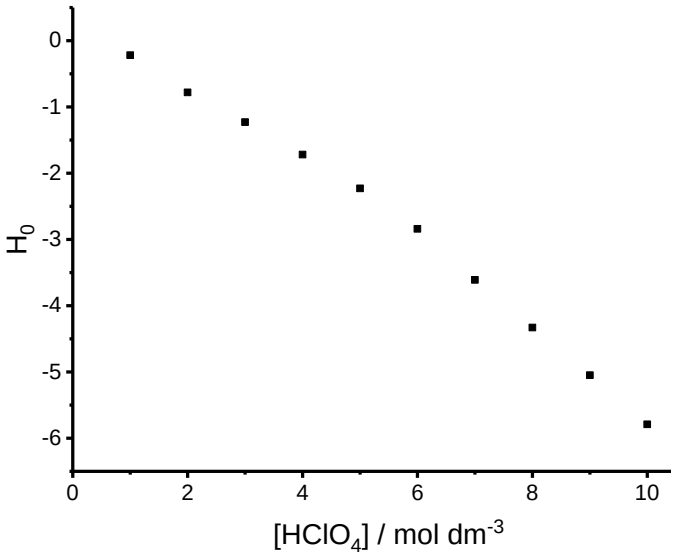

Figure 28. Graphs showing the relationship between concentration and the Hammett acidity function for perchloric acid

Figure 29 is plotted *vs.* H_0, following the work of Huang who plotted the half wave potential vs. pH,using the Hammett acidity function for solutions more acidic than pH 1. [26] Figure 29 shows data for the hydrogen region of the perchloric acid cyclic voltammograms, the trendlines shown have been generated using all the points except the starred point. The reason the 10 mol dm^{-3} point is omitted from the weak H plot is due to the peak being too close to the vertex of the voltammogram and as a result the peak is hard to isolate. The other point not used for the trendlines is the strong hydrogen peak for the 6 mol dm^{-3} as discussed earlier it was difficult experimentally to isolate.

The trendlines shown in Figure 29 have a gradient of 10 and 11 mV H_0^{-1} for the strong and weak peaks respectively. This is in excellent agreement with work by Gisbert *et. al* and Niet *et. al* where single crystal (Pt(533)) and polycrystalline platinum surfaces were studied and found to have a slope of 10 and 11 mV.[8,9] Both the previous studies investigated solutions between pH 2 and 12, so this work is an extension of the range currently in the literature. Comparing the trendlines in Figure 29 to that in Gisbert's work for the same peaks, not only is the gradient very similar, but the y-intercept is too. The variation in the gradient from what would be expected for a one electron one proton process, was explained as a multi-electron process where some of the surface is covered by OH or O shown in Equation 18.

$$H_{ad} + [x+y]H_2O \rightleftharpoons x(O_{ad}) + y(OH_{ads}) + [2x+y+1](H^+ + e^-)$$

Equation 18[8]

Although, Equation 9 does not account for variation in the gradient from the expected values, as there is still parity between protons and electrons. To explain any variation in the gradient form 0

mV pH^{-1} *vs.* RHE (-59 mV pH^{-1} *vs*. SHE) there must be a disparity between the number of protons and electrons, and therefore another charged species (remembering the reference electrode is shifting with solution concentration). With SHE being 0 V and RHE being equal in 1 M strong acid, and the deviation being -59 mV pH^{-1} *vs*. SHE. A partially charged species like OH^{+}_{ads} could account for observed disparity as shown in Equation 19, analogous to H_3O^+, commonly used to denoted acid solutions. Huang *et al.* observed the coordination of anions in the solution to the surface of platinum at potentials immediately more positive than the hydrogen peaks. This interaction could stabilise a positively charged surface species.

$$H_{ad} + xH_2O \rightleftharpoons x(OH^+_{ad}) + [2x+1]e^- + [x+1]H^+$$

Equation 19

The gradient calculated in Figure 29 of ~11 mV pH^{-1} unit (measured against a RHE scale) would be a gradient of -48 mV per pH unit on a SHE scale. This is due to the 59 mV shift in the reference electrode. This would mean the overall reaction has a ratio of 1.2 electron to each proton (59 / 48 = 1.2). Therefore taking Equation 19 and inputting the value of 1.2 generates Equation 20.

$$[2x+1] = 1.2[x+1]$$

Equation 20

The coverage calculated for the gradient observed in Figure 29 would be 25% of the amount of $Pt - H_{ad}$ there was to start with, with the remaining surface not having an oxide species on the surface. Biegler *et al*. has discussed in depth that only 77% of the surface Pt sites are covered by hydrogen.[28]

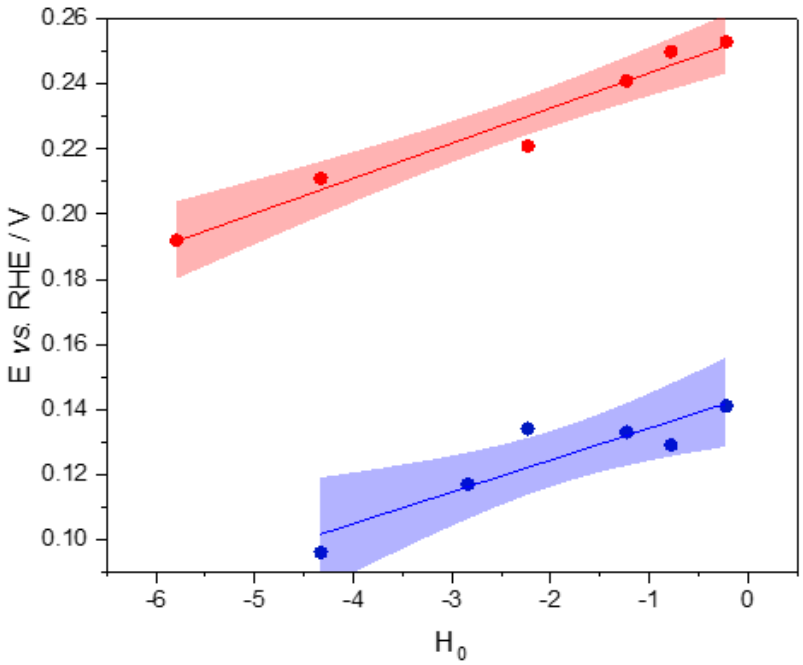

Figure 29. Plot showing the relationship between the hydrogen peaks and Hammet acidity function of the perchloric acid electrolyte. Blue dots are the weak peaks and the red dots are the strong peaks. The coloured bands indicate the 95% confidence limit of the trendlines.

To further highlight the agreement of the results presented here with the literature, the data points shown in Figure 29 have been plotted again alongside the points reported by Gisbert *et al.* It is clear to see from Figure 30 that the trend is continuous over the extended pH range with R^2 values of 0.99 and 0.96 for the strong and weak peaks respectively. The gradients shift slightly to 14 and 10 mV pH^{-1} meaning there may be different processes occurring in each case, but it is reasonable to suggest that at more positive potentials (where the strong hydrogen peaks are) there is more oxide replacing the previously hydrogen covered surface amounting to 33% OH^{+}_{ads}. The change in gradient is only small though and may also be explained as experimental error or as a slight offset between the two experiments as slightly different conditions and materials have been used. It should be remembered that highly porous electrodes have been used here compared to polished electrodes in the previous work.

Interestingly, the same reaction is occurring at the electrode surface over a very wide pH range (-5 to +12), the potential at which the process occurs shifts, but the process is the same. This is slightly surprising as it might be reasonable to suggest different surface coverage of surface adsorbates over this range as pH -5 is highly acidic and pH 12 is very basic.

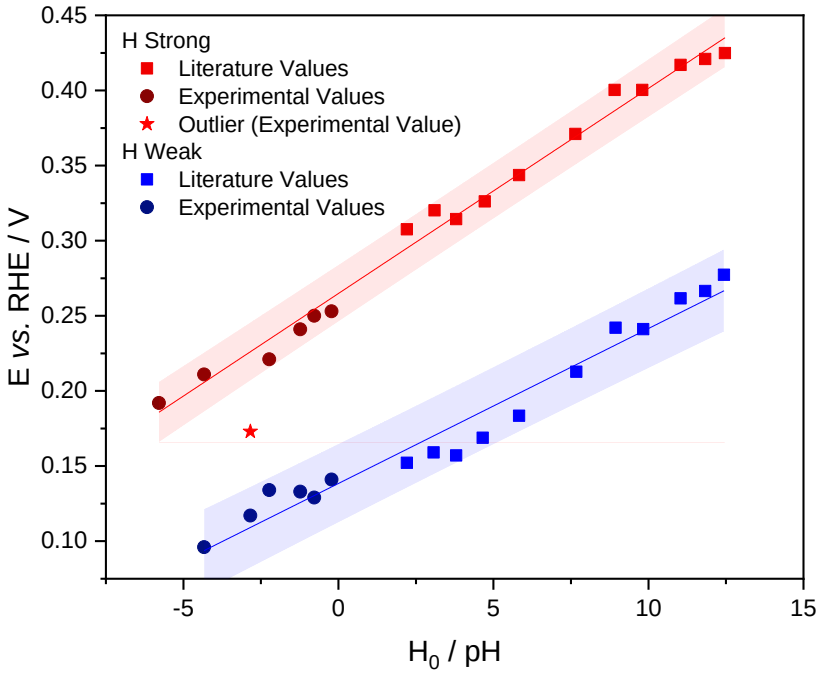

Figure 30. Plot showing the relationship between the hydrogen peaks and Hammet acidity function of the perchloric acid electrolyte, and values published by Gisbert et al. versus pH. The coloured bands indicate the 95% confidence limit of the trendlines.

3.3.4 Platinum Cyclic Voltammogram – Perchloric Acid – Oxide Formation

Now the results of the oxide region of the voltammogram will be presented and discussed. The oxide region of the voltammogram is from 0.5 V *vs.* RHE and more positive (see Figure 22). Using the Hammett acidity function greatly helps to explain the results of the oxide inflection point, making them much more easily understood. Figure 28 shows the inflection point plotted against H_0. Not only is the data now linear (one line with R^2 of 0.98) but the gradient is also more consistent with a value of -31 mV pH^{-1} *vs.* RHE (-90 mV pH-1 vs. SHE). When using the Nernst equation to calculate the ratio of protons and electrons the value is 1.5:1.

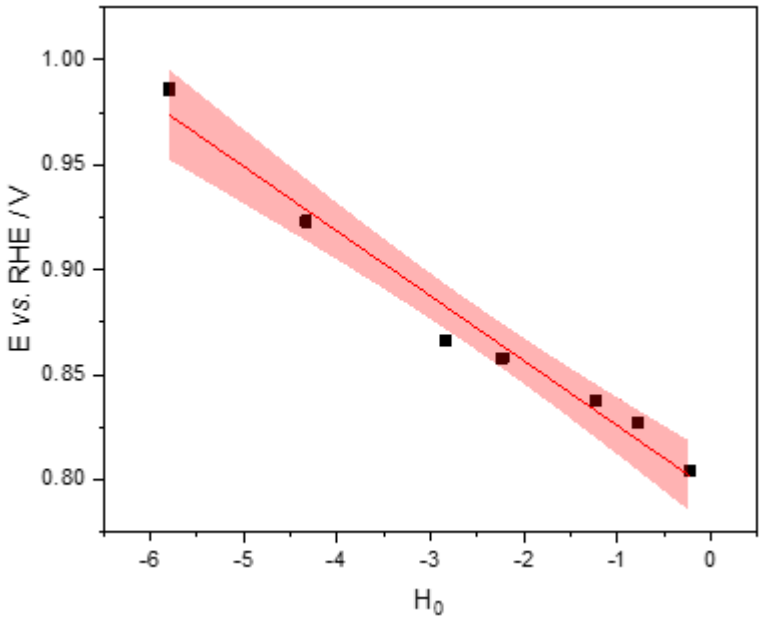

Figure 31. Plot displaying the shift in potential of the inflection point of the platinum oxidation for perchloric acid vs the Hammet acidity function. The coloured band indicates the 95% confidence limit of the trendline.

As previuosly discussed, the only way to account for the gradient not being -59 mV pH^{-1} *vs.* SHE is with a disparity in the number of protons and electrons in the electrochemical process. Equation 21 shows a process that could account for the gradient of Figure 31. Inputting the value of the gradient would require there to be 50% of the surface covered in OH^{+}_{ads} (the same species seen in the hydrogen region). It is reasonable to suggest this, as the results from the hydrogen peaks suggested 25-33% coverage at significantly less positive potentials, as the potential is moved more positive, the environment becomes more oxidising.

$$y(OH^{+}_{ad}) + xH_2O \rightleftharpoons [x + y](O_{ad}) + [y + 2x]\,H^{+} + 2x\,e^{-}$$

Equation 21

The OH^{+}_{ads} would need stabilising and this could be done by perchlorate anions, spectroscopic studies suggest this is the case with the perchlorate Surface Enhanced Raman signal being observed by Huang.[15] Huang also noted that this peak was replaced by platinum oxide peaks at potentials greater than 1 V *vs.* RHE for a pH 1 solution. It should be remembered that in this work the inflection point and not the peak potential has been reported, peak potentials would be more positive.

3.3.5 Platinum Cyclic Voltammogram – Sulfuric Acid

The same experiments were conducted using sulphuric acid and the raw data are displayed in Figure 22. The hydrogen peaks and the oxide inflection point were again investigated, and plotted versus the Hammett acidity function for sulphuric acid.

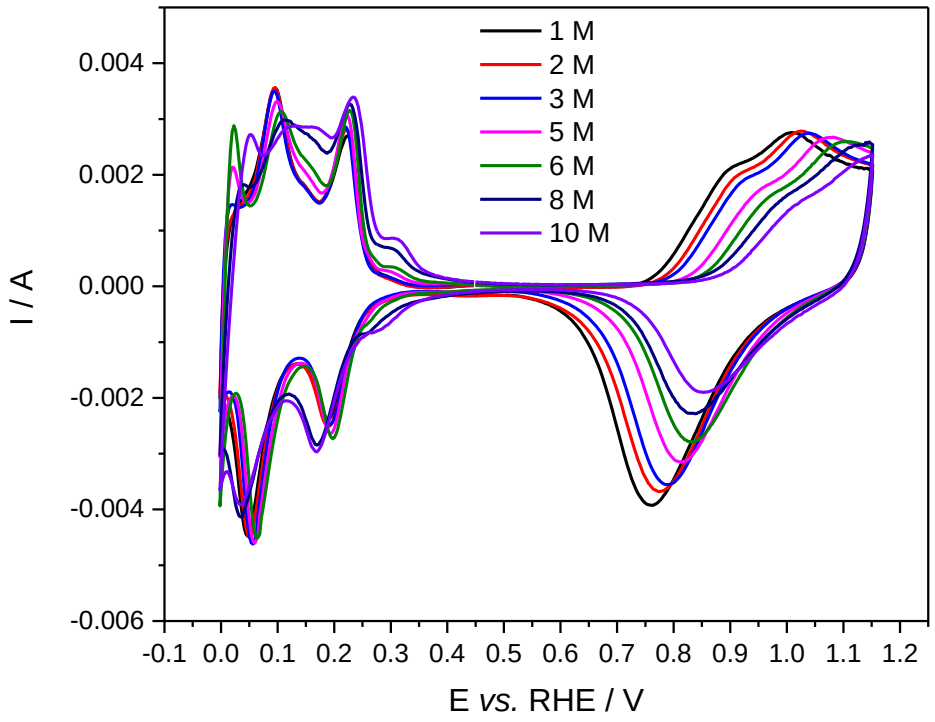

Figure 22. Voltammograms of seven perchloric acid solution from 1 mol dm^{-3} to 10 mol dm^{-3}. Counter electrode was a platinum gauze and reference electrode was a RHE. The cell was kept at 25°C with a thermostatic water bath, the scans were run at 5 mV s^{-1}. The electrochemical cell was purged with nitrogen gas for 15 minutes before the experiment and gas was supplied over the solution during the measurement. The above voltammograms are each the second cycle.

It is worth noting that the weak hydrogen desorption peak is less well defined at high concentrations of acid, this is in part due to overlap from the evolution of hydrogen gas. This is more of an issue at higher concentrations, as the evolution of hydrogen gas requires a lower overpotential in these solutions meaning more is produced.

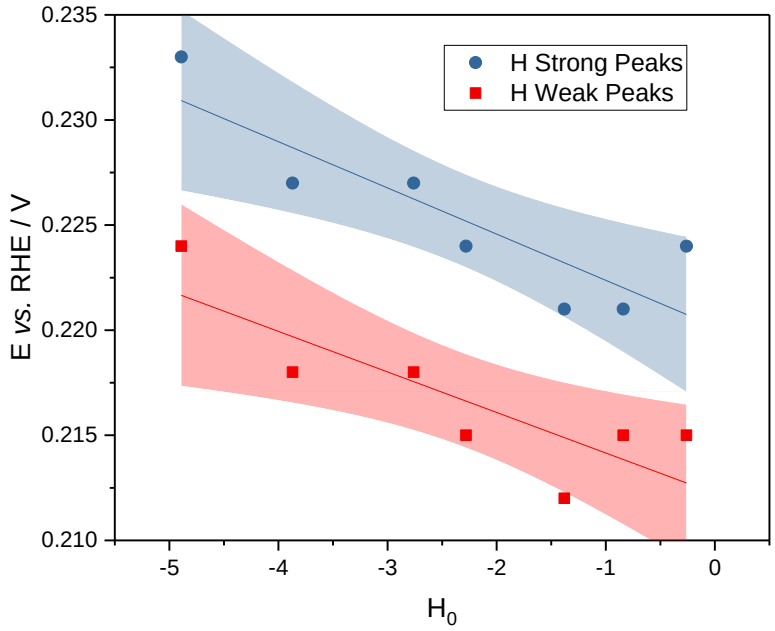

Figure 32. Plot showing the relationship between the hydrogen peaks and Hammet acidity function of the sulfuric acid electrolyte. The coloured bands indicate the 95% confidence limit of the trendlines.

The hydrogen peak dependence on H_0 is shown in Figure 32, where it can be clearly observed that both data sets have a similar gradient. When comparing these results to the results in perchloric acid (Figure 29) it is obvious that there is a different process occurring as the scale of the y-axis is much smaller for the sulphuric acid results. The gradient has also changed sign. Both the gradients in Figure 32 are 2 mV pH^{-1} when plotted versus RHE, which when plotted against SHE, is equivalent to -57 mV pH^{-1}. This suggests that the process for the sulphuric acid involves a very similar number of protons and electrons (57/59 is very close to one). This would support a one electron one proton process similar to Equation 22.

$$Pt - H \rightarrow Pt + H^+ + e^-$$

Equation 22

The explanation for the two different processes could be the competitive adsorption at the platinum surface, as sulfate anions will specifically adsorb to the surface and perchlorate anions will not. This means there are no free surface sites for oxidation of the surface in sulphuric acid. In 1996 it was reported that at between 0 and 0.1 V *vs.* Ag/AgCl (~0.2 - 0.3 *vs.* RHE) in 5 to 0.1 mmol dm^{-3} that bisulfate adsorbs to a platinum surface, therefore it is reasonable to predict that at lower pH and a similar potential there is bisulfate on the surface of platinum electrodes.[29] As it was shown the bisulphate adsorption shifts to lower potentials at lower pH.

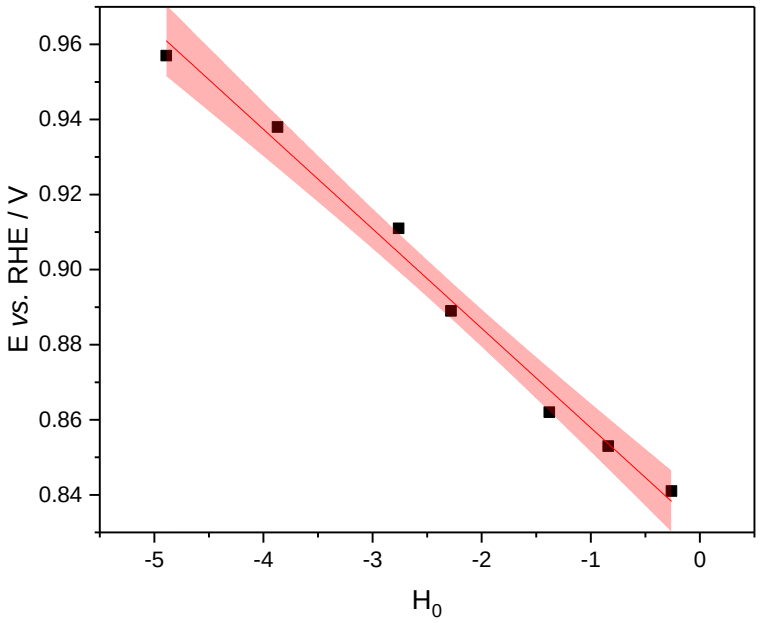

Figure 33. Plot displaying the shift in potential of the inflection point of the platinum oxidation for sulphuric acid vs the Hammet acidity function. The coloured band indicates the 95% confidence limit of the trendline.

Figure 33 shows that there is a very close relationship between the oxide inflection point and Hammett acidity function in sulphuric acid (R^2 is 0.99). The gradient is -27 mV pH^{-1} when plotted using values versus RHE which is -86 mV pH^{-1} when using values for SHE. If it is assumed the same process is occurring as for perchloric acid (Equation 21) then 48% of the surface would have OH^{+}_{ads}. Meaning that between the hydrogen region 0-0.25 V *vs.* RHE and the oxide inflection point there must be water dissociation on the platinum surface in either as a chemical (no electron transfer to the electrode) or unobservable electrochemical process. As discussed with the perchloric acid it is not unreasonable to suggest oxide species populating the surface of the electrode as the potential is moved more positive, but given the difference in the hydrogen region it might be expected that there is more of a difference in the oxide region too.

3.3.6 Platinum Cyclic Voltammetry – An Acid Concentration Measurement

Returning to the motivation of the work - trying to monitor the electrolyte concentration change in gas sensors without a fixed reference electrode - Figure 34 was generated showing the oxide inflection point and strong hydrogen peak for the concentrations of sulphuric acid used in the sensor.

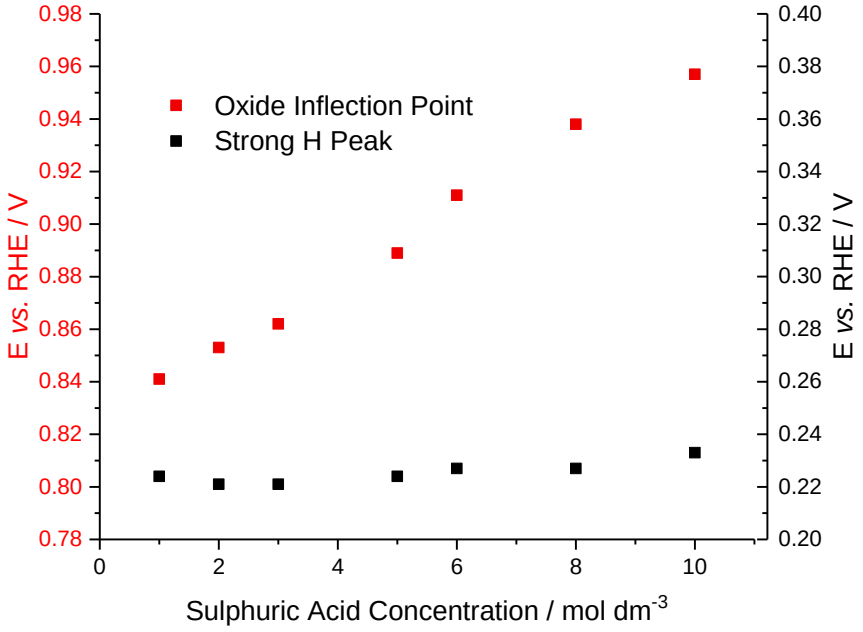

Figure 34. Potential of platinum oxide inflection (red squares using left hand y-axis) and strong hydrogen desorption peak (black squares using right hand y-axis) vs. sulfuric acid concentration

The potential difference highlighted in Figure 34 is enough to make a calculation of the concentration of the electrolyte concentration without the use of a fixed reference electrode. It is notable that although the strong hydrogen desorption peak is not completely static, the change in this peak with solution concentration is small, at least compared to the changed previously seen in the platinum oxidation. This difference is highlighted in Figure 34, where the potential of each process is plotted on the same graph (while there are two y-axes, as the peaks are in different parts of the voltammogram, the scales are the same). As long as there is no drift in reference electrode potential over one scan, the strong hydrogen peak can be a reference for the oxide inflection point to be measured against. Figure 35 is a calibration plot showing how the difference in peak potentials changes as a function of electrolyte concentration. This is a very linear dependence around the starting concentration in the gas sensor cells of 5 mol dm^{-3} (the R^2 value for the line of best fit is 0.99).

In a gas sensor this could work by running a cyclic voltammogram and measuring the strong hydrogen desorption peak and the inflection of oxide formation. The potential difference between these peaks will then be compared to the calibration plot to inform the user about any changes in concentration of electrolyte. This will lead to improved sensor performance as faulty sensors can be identified more quickly.

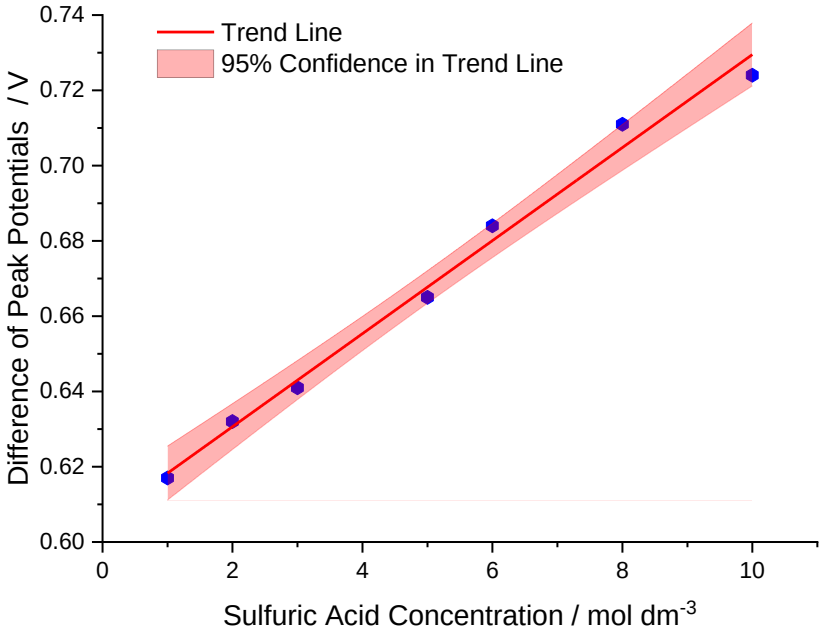

Figure 35. Graph showing the peak separation between the strong hydrogen desorption peak and the platinum oxide inflection point as a function of sulfuric acid concentration.

The trendline equation that describes this relationship is displayed in Equation 23 along with the statistical error calculated using the 95% confidence limit.

$$\Delta V = (0.0124 \pm 0.0015)[H_2SO_4] + 0.606 \pm 0.008$$

Equation 23

This can be rearranged to make the concentration of acid the focus of the equation, thus allowing this to be calculated from the peak separation. It should not be forgotten that although these two equations (23 and 24) are based purely on the empirical work presented herein, theoretical explanations for the relationship are accounted for, as discussed earlier in this chapter.

$$[H_2SO_4] = \frac{\Delta V - 0.606 \pm 0.008}{0.0124 \pm 0.0015}$$

Equation 24

3.4 Conclusions

The task of discovering a method for electrolyte calibration of sulfuric acid electrolytes using a platinum electrode without a stable reference electrode was completed. Comparison of the strong hydrogen desorption peaks with the inflection point of the platinum oxidation wave yielded a linear relationship with respect to concentration. The empirical formula produced is shown in Equation 25.

$$[H_2SO_4] = \frac{\Delta V - \ 0.606 \ \pm 0.008}{0.0124 \ \pm 0.0015}$$

Equation 25

These observed discrepancies from the Nernst equation were initially hard to understand, but by using the Hammett acidity function in place of pH (due to high acid concentrations) helped explain the processes. The hydrogen peaks shifted -48 mV pH^{-1} in strong agreement with the literature, when using perchloric acid. When using sulfuric acid there was very little shift from the predicted value of -59 mV pH^{-1} with an observed value of -57 mV pH^{-1}. The reactions shown in Equations 26 and 27 have been proposed for perchloric and sulfuric acid respectively.

$$H_{ad} + xH_2O \rightleftharpoons x(OH)^+_{ad} + [2x+1]e^- + [x+1]H^+$$

Equation 26

$$Pt - H \rightarrow Pt + H^+ + e^-$$

Equation 27

Despite the different process proposed in the most negative region of the voltammograms for the different acids, the platinum oxide inflection point showed a similar response for both. Equation 28 has been suggested as a likely reaction accounting for the disparity between the number of electrons and protons needed to satisfy the results.

$$y(OH^+_{ad}) + xH_2O \rightleftharpoons [x+y](O_{ad}) + [y+2x]\ H^+ + 2x\ e^-$$

Equation 28

In conclusion, for perchloric acid the surface is hydrogen covered between 0 V and approximately 0.2 V *vs.* RHE. At this point the hydrogen is desorbed and 25-33% of the surface is covered with OH^+_{ads}. Going more positive the surface becomes 50% OH^+_{ads} covered and at the oxide inflection point the surface hydroxide and water react with the platinum surface to make higher order

oxides. The process is the same when using sulfuric acid apart from the surface is not immediately covered with OH^{+}_{ads} when the H_{ads} desorbs, due to sulfate and bisulfate adsorption.

It should be remembered along with these conclusions that the electrodes used were not well defined surfaces, but samples from a gas sensor which are highly porous. As a result, not only has it been proved that the pH range over which these peak shifts can be predicted is now wider, but non ideal electrodes can detect these changes. Meaning that the application of this theory can be immediately realised.

3.5 References

1 Leach, A. S.; Russell, A. E. WPO, WO2018/059717Al, 2016.

2 M. Wienecke, M.-C. Bunescu, M. Pietrzak, K. Deistung and P. Fedtke, *Synth. Met.*, 2003, **138**, 165–171.

3 M. K. Debe, *Nature*, 2012, **486**, 43–51.

4 M. Bernt, M. Singer and H. A. Gasteiger, *Meet. Abstr.*, 2017, **MA2017-01**, 1382–1382.

5 X. Chen, I. T. McCrum, K. A. Schwarz, M. J. Janik and M. T. M. Koper, *Angew. Chemie Int. Ed.*, 2017, **56**, 15025–15029.

6 M. Willett, *Sensors*, 2014, **14**, 6084–6103.

7 M. Willett and Martin, *Sensors*, 2014, **14**, 6084–6103.

8 M. J. T. C. van der Niet, N. Garcia-Araez, J. Hernández, J. M. Feliu and M. T. M. Koper, *Catal. Today*, 2013, **202**, 105–113.

9 R. Gisbert, G. García and M. T. M. Koper, *Electrochim. Acta*, 2010, **55**, 7958–7965.

10 H. Angerstein-Kozlowska, B. E. Conway and W. B. A. Sharp, *J. Electroanal. Chem. Interfacial Electrochem.*, 1973, **43**, 9–36.

11 B. V. Tilak, B. E. Conway and H. Angerstein-Kozlowska, *J. Electroanal. Chem. Interfacial Electrochem.*, 1973, **48**, 1–23.

12 M. A. H. Lanyon and B. M. W. Trapnell, *Proc. R. Soc. A Math. Phys. Eng. Sci.*, 1955, **227**, 387–399.

13 N. Sato and M. Cohen, *J. Electrochem. Soc.*, 1964, **111**, 512.

14 Z. Nagy and H. You, *Electrochim. Acta*, 2002, **47**, 3037–3055.

15 Y.-F. Huang, P. J. Kooyman and M. T. M. Koper, *Nat. Commun.*, , DOI:10.1038/ncomms12440.

16 A. Murthy and A. Manthiram, *J. Phys. Chem. C*, 2012, **116**, 3827–3832.

17 W. B. Jensen, *J. Chem. Educ.*, 2004, **81**, 21.

18 R. P. Buck, S. Rondinini, A. K. Covington, F. G. K. Baucke, C. M. A. Brett, M. F. Camoes, M. J. T. Milton, T. Mussini, R. Naumann, K. W. Pratt, P. Spitzer and G. S. Wilson, *Pure Appl.*

Chem., 2002, **74**, 2169–2200.

19 L. P. Hammett and A. J. Deyrup, *J. Am. Chem. Soc.*, 1932, **54**, 2721–2739.

20 M. J. Jorgenson and D. R. Hartter, *J. Am. Chem. Soc.*, 1963, **85**, 878–883.

21 R. O. Lezna, N. R. de Tacconi and A. J. Arvía, *J. Electrochem. Soc.*, 1979, **126**, 2140.

22 A. Kolics and A. Wieckowski, , DOI:10.1021/jp003536f.

23 F. Gloaguen, J.-M. Léger and C. Lamy, *J. Electroanal. Chem.*, 1999, **467**, 186–192.

24 H. E. Darling, *J. Chem. Eng. Data*, 1964, **9**, 421–426.

25 L. H. Brickwedde, *J. Res. Natl. Bur. Stand. (1934).*, 1949, **42**, 309.

26 W.-S. Huang, B. D. Humphrey and A. G. MacDiarmid, *J. Chem. Soc. Faraday Trans. 1 Phys. Chem. Condens. Phases*, 1986, **82**, 2385.

27 M. A. Paul and F. A. Long, *Chem. Rev.*, 1957, **57**, 1–45.

28 T. Biegler, D. A. J. Rand and R. Woods, *J. Electroanal. Chem. Interfacial Electrochem.*, 1971, **29**, 269–277.

29 S. Thomas, Y.-E. Sung, A. H. S. Kim and A. Wieckowski, , DOI:10.1021/JP9606321.

Chapter 4: *In situ* XAS measurements of Platinum nanoparticles for electrocatalysis of oxygen

In this chapter Pt/C electrodes have been measured using extended X-ray absorption fine structure (EXAFS) and X-ray absorption near edge structure (XANES), to understand how this material changes as a function of potential. It has long been the aim of research in both catalysis and elecrocatalysis to establish criteria (structure/property relationships) that would allow the prediction of the activity of a new material based on either an independently measureable parameter or a theoretical calculation. Recently this goal appears to have been achieved, at least in the case of the electrocatalytic reduction of oxygen (ORR), where a correlation has been established between the centre of the oxidation state of the metal, and electrocatalytic activity. This relationship of activity to catalyst oxidation state and catalyst−oxide bond lengths and strengths follows from structure−property/ structure−rate correlations established by the application of the Sabatier principle of heterogeneous catalysis.[1] X-ray absorption spectroscopy (XAS) offers a direct means to measure such relationships; catalyst oxidation state may be empirically resolved from the X-ray absorption near-edge structure (XANES) region, while coordination number, bond lengths in the particles can be determined from electron backscattering calculations in the extended X-ray absorption fine structure (EXAFS).[2,3]

Both the oxygen reduction reaction and oxygen evolution reaction are important for oxygen pump sensors. These reactions are both catalysed by platinum, so understanding these reactions is very important for future catalyst design, which could use new materials or optimise the use of platinum, which is rare and expensive.

4.1 Introduction

This work comprehensively investigates 2 nm platinum carbon supported nanoparticles over a wide potential range. When working with electrochemical XAS it is very important to use small particles as XAS is a bulk technique. Therefore, to be able to resolve changes of the particles' surface caused by the electrochemical potential control, the surface to bulk ratio needs to be as large as feasibly possible.

In this chapter a variety of synchrotron based XAS methods will be used to characterise the electrochemical oxidation of platinum on carbon catalysts. XANES and HERFD-XANES provides information regarding oxidation state and the nature of the oxide formed. EXAFS provides

information about the overall structure. Use of all these techniques provides additional understanding of the details of the oxide formation process.

As these measurements all use hard X-rays measurements can be conducted *in situ* as opposed to other techniques such as X-ray Photoemission Spectroscopy (XPS). Both XAS and XPS can probe the electronic structure of materials, but as XAS uses much harder X-rays *in situ* measurements are significantly more practical.

4.1.1 Platinum High Energy Resolution Fluorescence Detection (HERFD) XANES

In HERFD XANES the effective core−hole lifetime is greatly reduced relative to conventional XAS. The effect of HERFD XANES when used at the Pt L_3 edge is to enhance features observed in conventional XAS.[4] In particular, changes in the near the "white line" can be resolved more clearly. The "white-line" at the Pt L_3 edge arises from $2p_{3/2}$ to 5d transitions, and its intensity has been shown to be proportional to the unoccupied 5d electron density of states,[5] which is very sensitive to changes in the chemical environment of the Pt atoms. Chemisorbed oxygen species and Pt oxides are as a result more readily differentiated using HERFD XANES than with conventional XAS methods.

Previous work has been conducted investigating electrochemical platinum HERFD spectra, but not over such a comprehensive range of potentials.[4] The previous work by Merte *et.al.* shows HERFD XANES for 1.2 nm Pt particles over a range of potentials and compares these experimental spectra to FEFF8 (a DFT code commonly used simulate XAS spectra) calculated spectra. Metre *et al.* concluded that the HERFD XANES allowed the chemical state of the platinum nanoparticles to be divided into three regions. Hydrogen chemisorption between 0 V *vs.* SHE and ∼0.3 V *vs.*RHE, oxygen chemisorption (as OH or O) between 0.3 and 0.96 V *vs.* RHE, and platinum oxide formation at or above 0.96 V *vs.* RHE. This is the only example of electrochemical *in situ* HERFD XANES in the literature of platinum nanoparticles. There have been other studies of electrochemical *in situ* measurements, for example Pt/Rh alloys have been investigated and the surface oxide formation probed.[6] However, there have been other examples of platinum nanoparticle HERFD XANES, such as Tromp and Safonova's investigation into the adsorption of gaseous CO molecules onto Pt nanoparticles.[7,8] They were able to use the very high-energy resolution to determine the adsorption site of this adsorbate on the surface of the metal, demonstrating the power of the technique. Gorczyca *et.al.* used HERFD XANES to quantify the coverage of hydrogen on Pt nanoclusters at a combination of different pressures and temperatures, again presenting the significant sensitivity of this method.[9] HERFD has even been shown to have the power to

deconvolute EXAFS of elements that have edges very close in energy, although this is a very slow method, taking 6 hours per measurement.[10]

4.1.2 Platinum Extended X-ray Absorption Fine Structure (EXAFS)

In this work EXAFS has been used to calculate the size of Pt nanoparticles. Initial theoretical studies of FCC crystal systems were conducted by Benfield and Fritsche, where the effect of cluster size on the first shell coordination was studied.[11,12] Benfield also included work on how different geometries affect the coordination numbers. This was followed by Montejano *et al.* who conducted a more thorough investigation into cluster size and geometry; cuboctahedral, isoctahedral, body centred and primitive were all considered.[13] In 1999, Jentys continued this work and discussed the affect size has on coordination numbers out to the fifth shell of atoms around the target atom.[14] Glasner *et al.* computed definite coordination numbers for the first six nearest neighbours for a number of geometries and clusters up to 1000 atoms in size.[15] Therefore, this technique, as a method of particle size evaluation, is best used on smaller particles of up to 1000 atoms. More recently, Beale investigated the theoretical EXAFS of FCC HCP and BCC crystal structures as well as discussed bimetallic analysis, this however, is beyond the scope of this work, where only a monometallic system is studied.[16] In summary, these studies suggest that the mean coordination numbers for small clusters changes significantly, but the values tend to bulk like values around 1000 atoms.

This thesis used two different techniques for measuring platinum EXAFS. The differences between the two techniques have been highlighted by Mathew *et al*. in 2000. [17] They compared the spectra from conventional EXAFS and EDE, importantly reporting that the EXAFS are artificially reduced in intensity when the *k* range was reduced from 21 to 12 $Å^{-1}$. When considering the EDE results then, it is important to remember the data collection method may impact the analysis. They also reported that the white line was reduced by a ratio of 1 : 0.71 when comparing conventional EXAFS to EDE, as well as an increase in experimental broadening, which will impact on the analysis of the XANES. HERFD XAS is a technique where XAS spectra are measured with an instrumental broadening that is lower than the core hole lifetime broadenings, whereas the instrumental broadening of the conventional XAS is greater and even greater again for EDE.[18]

4.1.3 Platinum Hydrogen XANES Features

Mukerjee has published a number of papers using the delta-mu (Δμ) method, where the relative changes in XAS spectra are compared by subtracting spectra from each other.[19–21] This method has been used to elucidate surface processes by subtracting the 'bulk' spectra, as a result this

method could be very useful in understanding the hydrogen features of the XANES spectra as these are very subtle.[22]

There have been reports of chemisorbed hydrogen casuing a broadening of the first absorption peak at 10 eV above the edge, or a high energy shoulder in the white line.[22,23] First reported by Samant *et al.* who detected the shoulder using heterogeneous Pt catalysts that were measured in different gas environments. This feature is observed by Merte *et al.* in an electrochemical *in-situ* experiment between -0.04 and +0.2 V *vs.* RHE, Pt nanoparticles of 1.2 nm were used in their study. In this work, these features will also be investigated, although might appear less significant as the particles are larger so the surface to bulk ratio is smaller.

4.1.4 Chapter Outline

In this chapter three different XAS techniques will be used to measure the same particles under the same potential control region. How these particles surfaces change under both oxidising and reducing conditions will be investigated. The use of conventional XAS will act as a baseline for the work, HERFD offers higher energy resolution in the XANES region and therefore will be able to detect more elusive features. The EDE measurements will allow more realistic timescales for applications (such as gas sensors) to be investigated. Comparison of the high time resolution spectra and high-energy resolution spectra will provide a complete XAS analysis of this electrocatalyst.

4.2 Experimental

4.2.1 Transmission Electron Microscopy

The 20 wt% Pt/C catalyst that was used in the work was supplied by Johnson Matthey (Sonning Common) and has an average particle size of 2 nm determined by TEM. This was chosen, as a high surface to bulk ratio/small particle size is needed for changes in the XAS to be clearly observed. Transmission electron microscopy (TEM) was performed on an FEI Tecnai 12 at 80 kV and images of this catalyst are shown in Figure 36. The particle size distribution was obtained by measuring 174 particles as shown in Figure 37 and two similar TEM images.

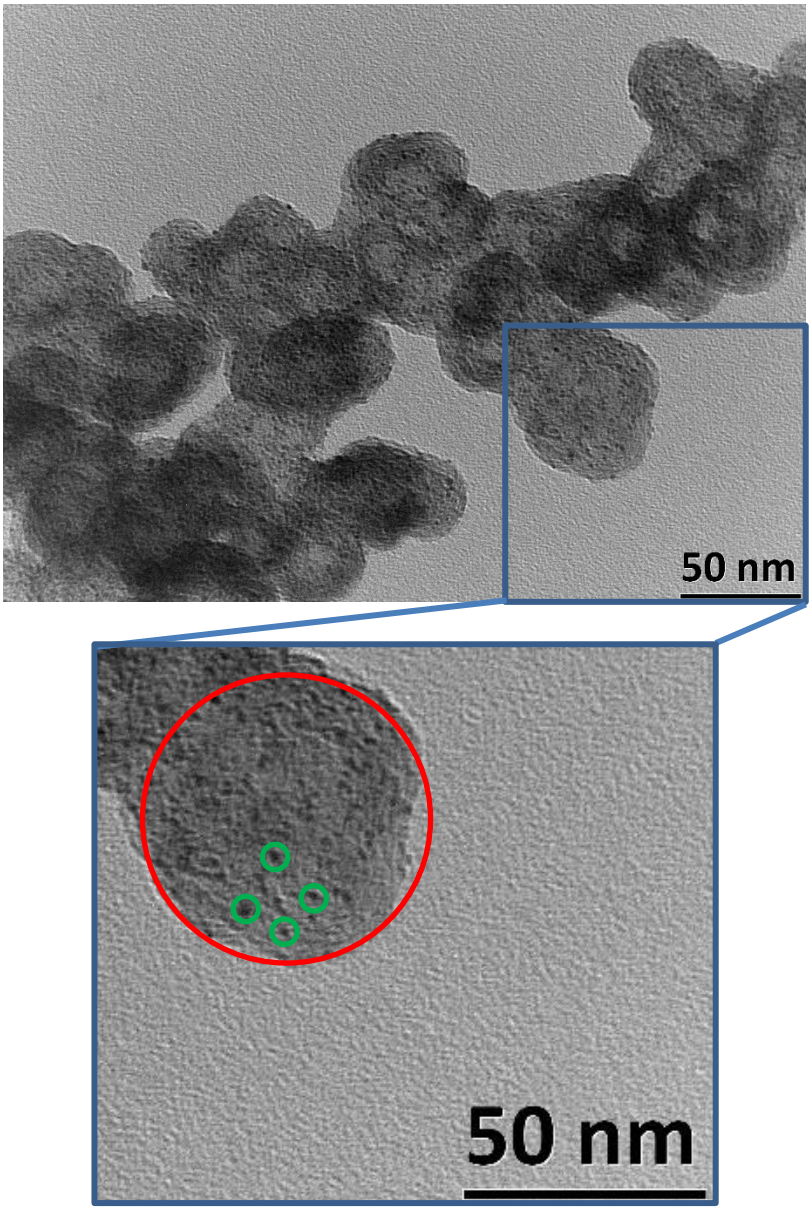

Figure 36. TEM image of Pt/C sample measured using FEI Tecnai 12 at 80 kV at 30,000 times magnification. The small black spots are the platinum particles and the larger grey regions the carbon

support, more clear on the zoomed in region where the red circle shows a grey carbon mass and the green circles highlight four of the smaller black spots of Pt particles.

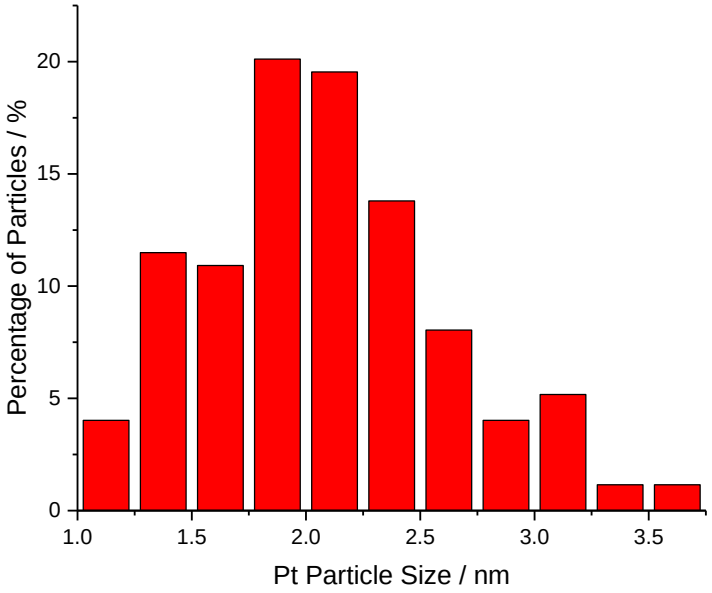

Figure 37. Particle size distribution of the Pt/C catalyst from TEM images (Figure 36 and two others), these measurements were conducted using ImageJ software.

The translucent grey masses in Figure 36 are the carbon support particles that are on the order of 50-100 nm and the darker black spots are the Pt particles that have been measured (three images were used to form the size distribution in Figure 37 to ensure this was a fair representation, one of the images is shown in Figure 36). The images were manually measured using the measurement tool in ImageJ software.

4.2.2 High Energy Resolution Fluorescence Detection (HERFD) vs. Total Fluorescence Yield (TFY) vs. Energy Dispersive EXAFS (EDE)

In situ electrochemical XAS studies typically use fluorescence detection instead of transmission. This is due to the quantity requirements of transmission measurements, meaning it is very hard to produce a high quality electrode with enough material. There is a balance to be struck between loading (lower loadings have lower resistance and the electrochemistry is better) and having enough of a sample to get a large enough signal from the X-rays. The reason lower loadings have better electrochemistry is the currents are lower, meaning a lower IR drop. This normally means that fluorescence detection is used, as it is a more sensitive technique. Total Fluorescence Yield (TFY) works by getting a fluorescence detector close to the sample, to maximise the solid angle (as the x-rays are fluoresced in 360° solid angle), and selecting only the photons being from the target

metal (using an energy discriminating detector), this experimental design is shown in Figure 38. In contrast high energy resolution fluorescence detection (HERFD) uses a Johann spectrometer where the fluoresced X-rays travel to a set of analyser crystals which are spherically bent and focus the emitted X-rays onto a detector. Control of the position of the analyser crystals and detector allow for very high energy resolution in the spectra, as they diffract the fluoresced beam ensuring only a very small window of wavelengths are detected. Figure 39 shows the beamline schematic for the Johann spectrometer and Figure 40 shows how this looks on beamline I20 at Diamond Light Source. The path of the fluoresced X-ray is though a He filled bag, helium is chosen as it is inert and has a small X-ray cross section, this can be seen as the black bag in Figure 40.

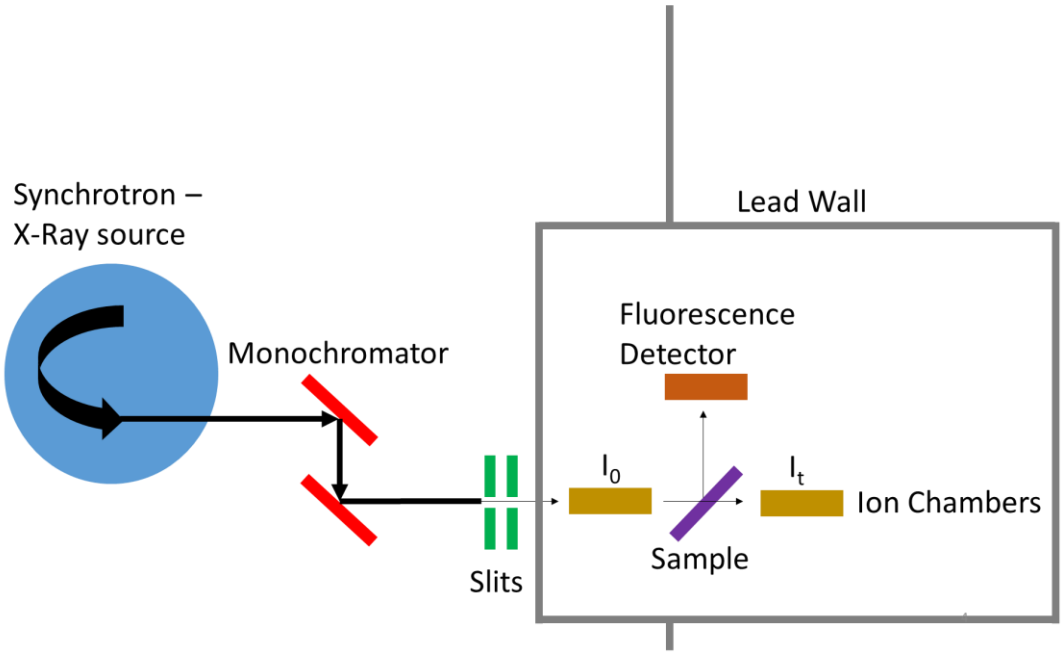

Figure 38. Schematic of B18, a conventional XAS beamline.

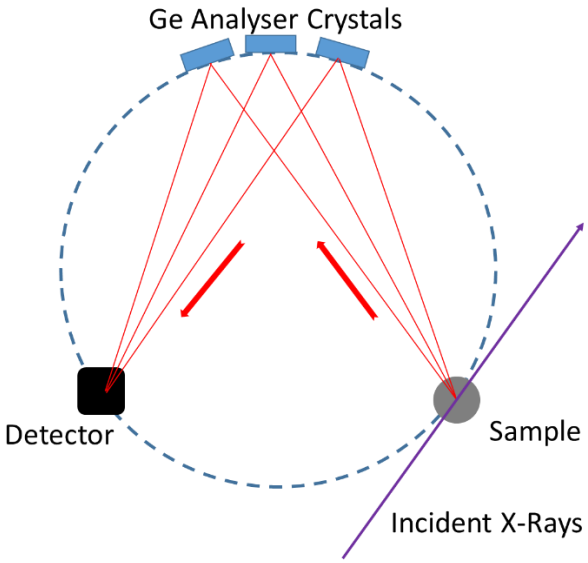

Figure 39. Schematic of Johann Spectrometer. Purple line shows the incident beams and red lines show emitted X-rays (arrows show the direction of the X-rays).

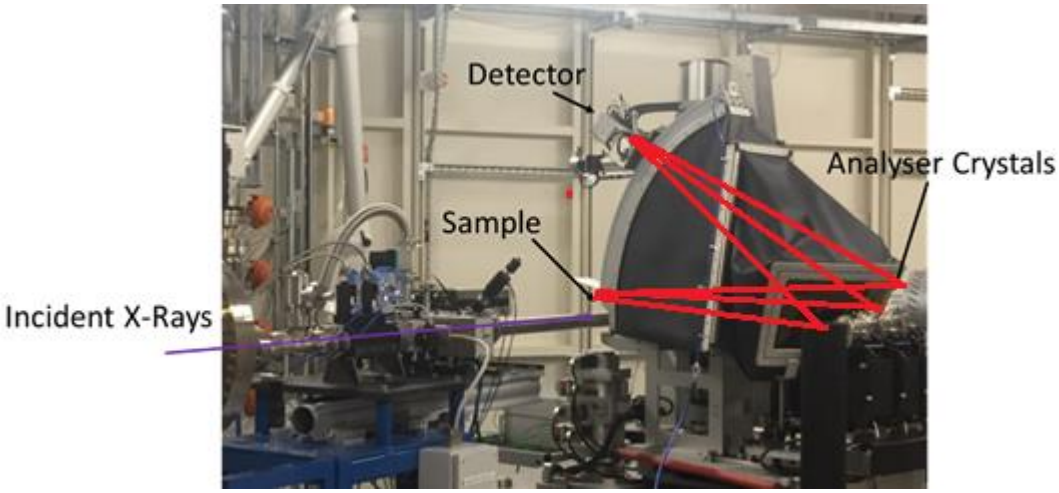

Figure 40. Picture of Beamline I20 at Diamond Light Source. Red lines show the path of the X-rays.

Safonova *et. al.* showed in 2006 how the Johann spectrometer used to collect HERFD XANES increases the spectral resolution significantly for Pt XANES over total florescence's yield.[8] In the work presented here, HERFD XANES measurements will be used to elucidate the surface processes occurring at the Pt electrolyte interface. To do this a deconvolution of the peaks in the XANES region was required, which was only possible due to the higher energy resolution of HERFD.

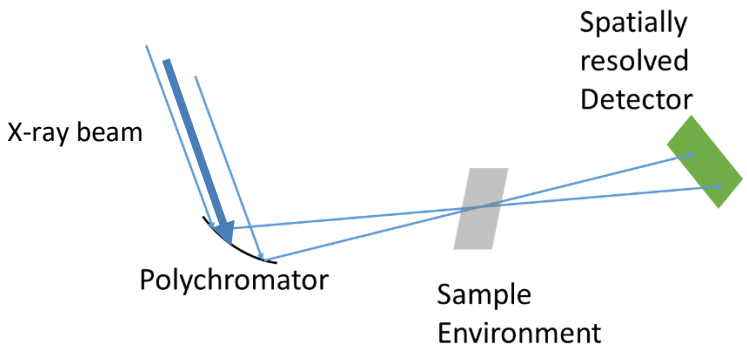

Figure 41. Schematic of an EDE beamline.

The X-ray measurements were carried out at Diamond Light Source using beamline B18 for the EXAFS measurements, I20-EDE for the Energy Dispersive EXAFS measurements, and I20 -Scanning for the HERFD (XANES) measurements. The samples have been prepared by painting catalyst inks onto teflonated Toray carbon paper as described in chapter 2. These electrodes were then electrochemically cycled between -0.65 and 0.4 V *vs.* SMSE for 20 cycles at 20 mV s^{-1}, to ensure the electrochemical response was reproducible.

These samples were loaded into the electrochemical cell, depicted in section 2, for measurement. Both the B18 and I20-scanning measurements were conducted in fluorescence mode, using a Ge detector. The I20-EDE measurements used a FReLoN detector (CCD detector), whilst the B18 measurements used a Ge solid state detector.[24] The beam, for I20-scanning and B18, has been normalised using the incident X-rays that have been measured using an ion chamber upstream of the sample. I20-scanning used a four bounce Si(111) crystal monochromator, this in contrast to the Si(1 1 1) double crystal monochromator used in B18. The synchrotron was running in a 10 min top-up mode with a ring current of 300 mA and an energy of 3 GeV.

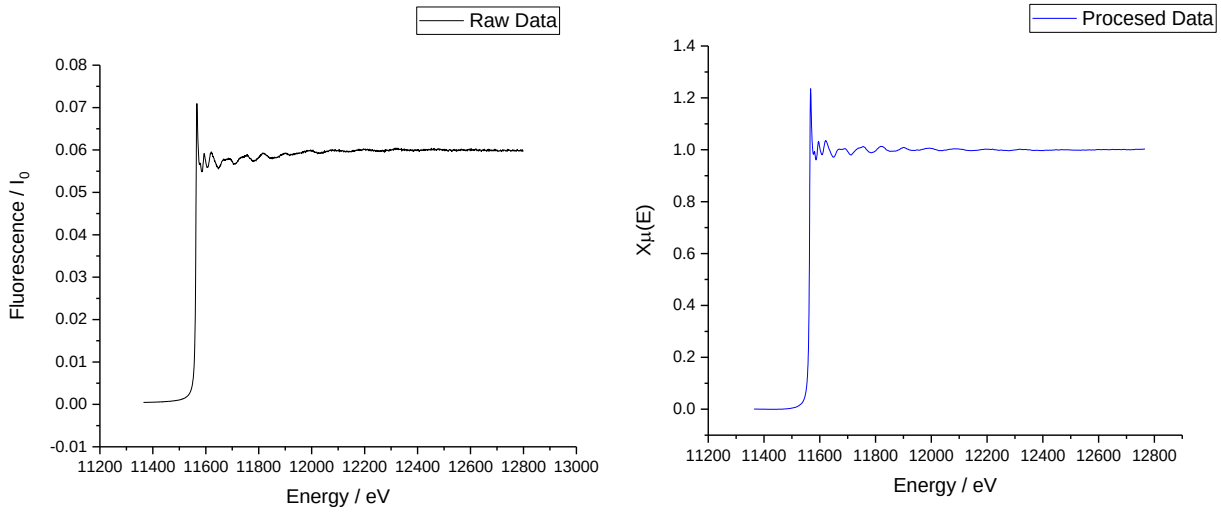

Figure 42. Left- plot showing the raw data of fluorescence over incident intensity *vs.* incident energy. Right – plot showing the result of 4 raw files merged together and the resulting data has been normalised to 0 for the pre-edge and 1 for the post edge

The data were processed and analysed using the Demeter software package, using the Athena program for the processing and XANES analysis and the Artemis program for the EXAFS analysis.[25] The data were aligned to the documented value for edge position (Pt L_3 – 11564 eV) by comparison to a Pt foil. The data were merged as four measurements were made for each potential on B18 (two were made for each potential on I20), then normalised so that the pre edge line is zero and the post edge line is set to one.[26] Figure 42 shows raw and processed data for -600 mV *vs.* SMSE for data collected at B18.

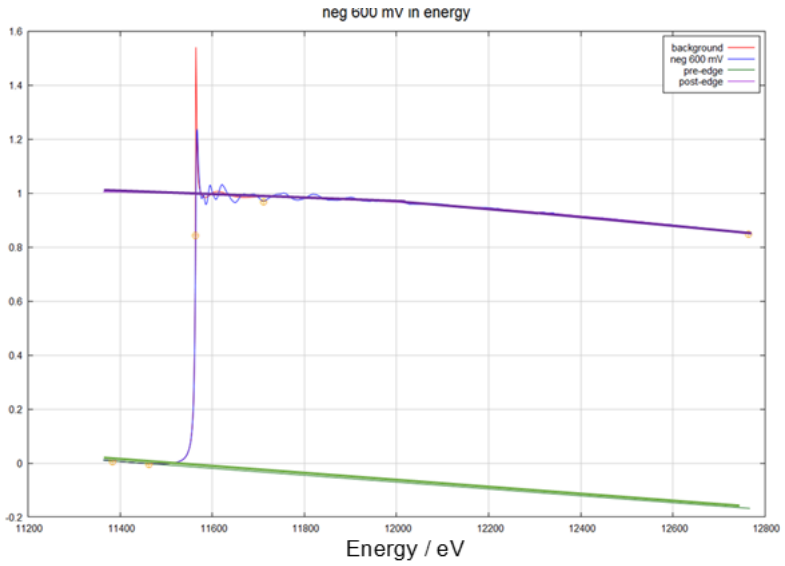

Figure 43. This plot shows how the pre- and post-edge lines are fitted to the merged data.

Figure 44 shows the two main areas of interested with the XANES in blue and EXAFS in green, the same processed spectrum from Figure 42 has been used. The XANES has information about the

oxidation state of the material and the EXAFS has information about the local coordination of the material being measured.

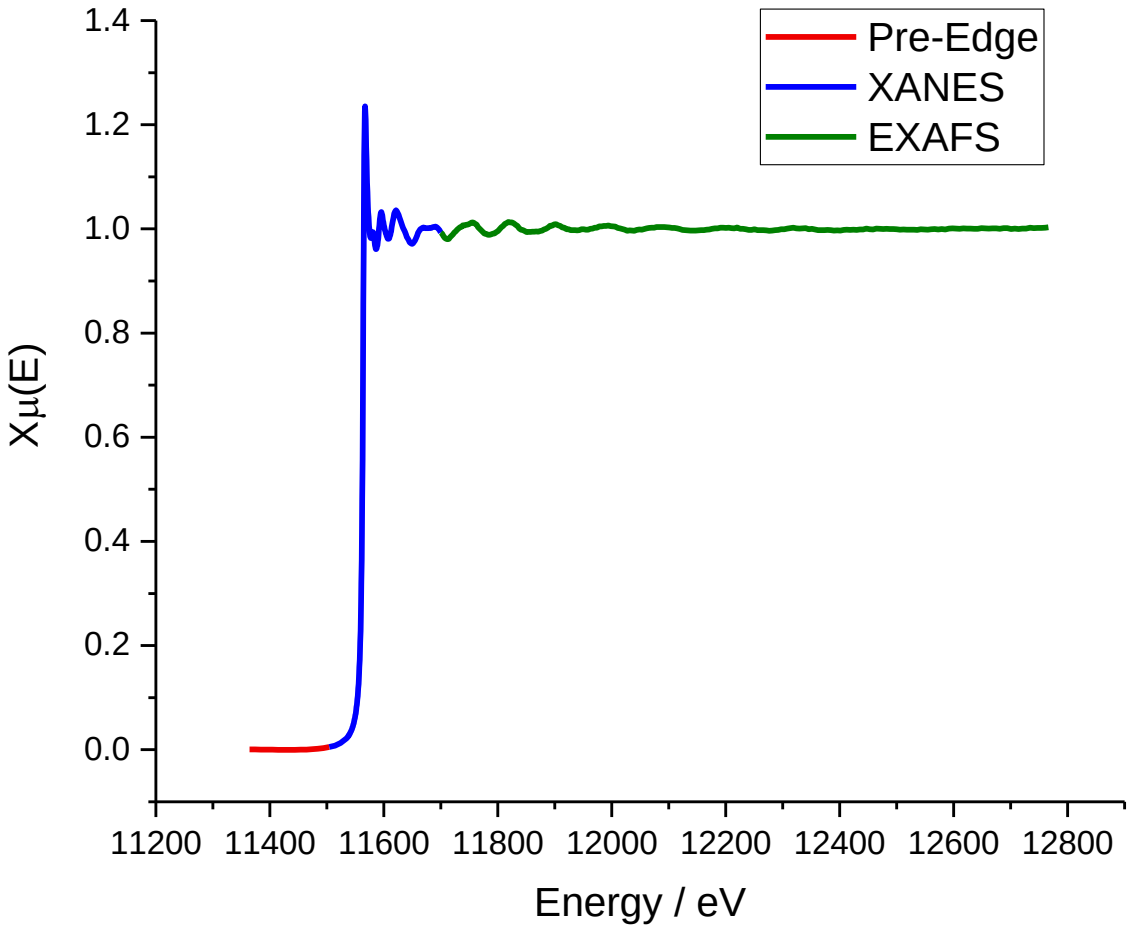

Figure 44. Shows the processed data from Figure 42 with the three main regions highlighted, pre-edge in red, XANES in blue and EXAFS in green.

When presenting EXAFS data, the background function is subtracted and the energy scale is converted from eV to $Å^{-1}$ this is known as k-space and the conversion is shown in equation 29:

$$k = \sqrt{2m_e(E - E_0)/\hbar^2}$$ **Equation 29**[27]

Where m_e is the mass of an electron, E is the previous energy scale (eV), E_o is the edge position and ħ is reduced planks constant. When viewing the data in *k*-space typically the data is shown *k*, k^2 and k^3 weighted, this is done by multiplying the data by x-axis to the appropriate power. This allows the EXAFS undulations to be more easily observed, as in each plot different parts of the spectra are highlighted. Figure 45 shows the EXAFS k^2 weighted using the same data as the previous figures. When the data is fit to a model the data are fit in *k*-space and *R*-space. *R*-space is the Fourier transform of *k*-space, and can loosely be considered a radial distribution function of atoms around the target atom. However, this is not a true radial distribution function, as there are not only single scattering paths contributing to the signal, but also multiple scattering paths. *R*-

space can help to visualise changes, but conclusions should only be drawn once the EXAFS have been fit to calculated spectra, Figure 46 shows the *R*-space for the data shown in Figure 45.

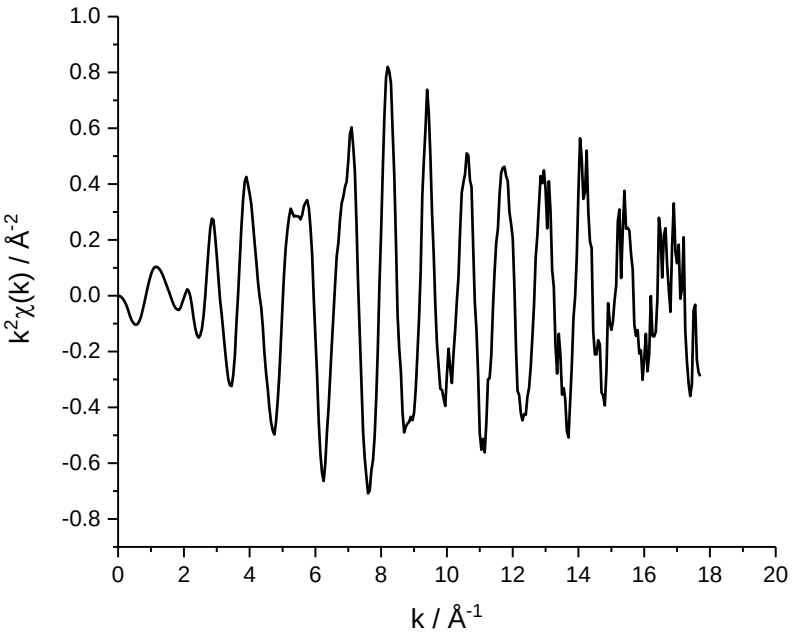

Figure 45. Showing the k^2 weighted EXAFS of Pt/C electrode while at -600 mV *vs.* SMSE in 1 mol dm^{-3} perchloric acid electrolyte.

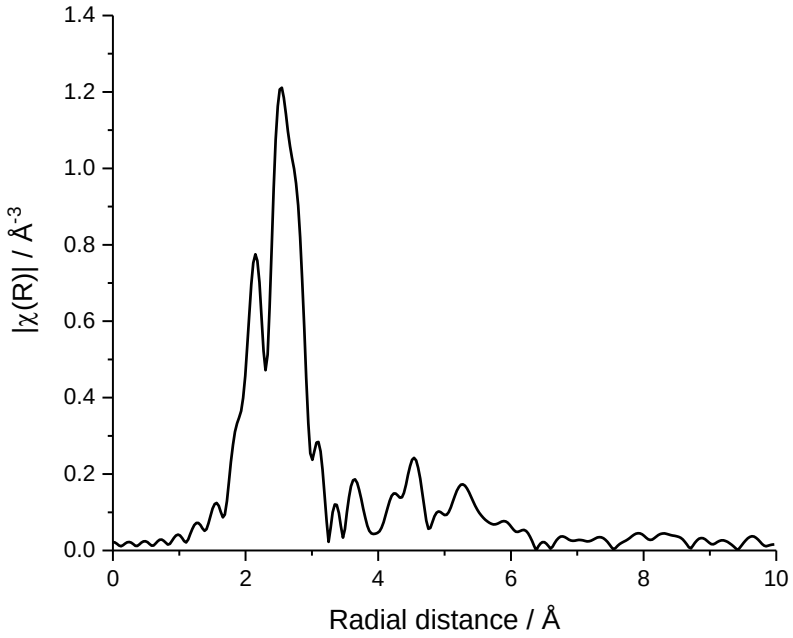

Figure 46. Showing the *R*-space EXAFS of the data shown in Figure 45 of Pt/C electrode while at -600 mV *vs.* SMSE in 1 mol dm^{-3} perchloric acid electrolyte.

The XANES in this work collected using B18 have been analysed using a linear combination fitting (LCF) producing a theoretical spectra using reference data (Pt foil and PtO_2) to match to the

sample data. Analysis was conducted using the Athena software package. Figure 47 shows the XANES for spectra collected by TFY (black) and HERFD (red), it is clearly observed that there are features at similar energies but there is significantly less experimental broadening in the HERFD spectra. This is largely observed in the XANES region and the spectra are almost identical at energies greater than 100 eV above the edge.

All of the fits in this chapter will be compared by the quality of the R-factor. The R-factor is a goodness of fit parameter calculated using equation 30:

$$R = \frac{\Sigma F_{obs} - F_{fit}}{F_{obs}}$$

Equation 30

Values below 0.05 will be considered good fits, this is a 95% confidence limit.

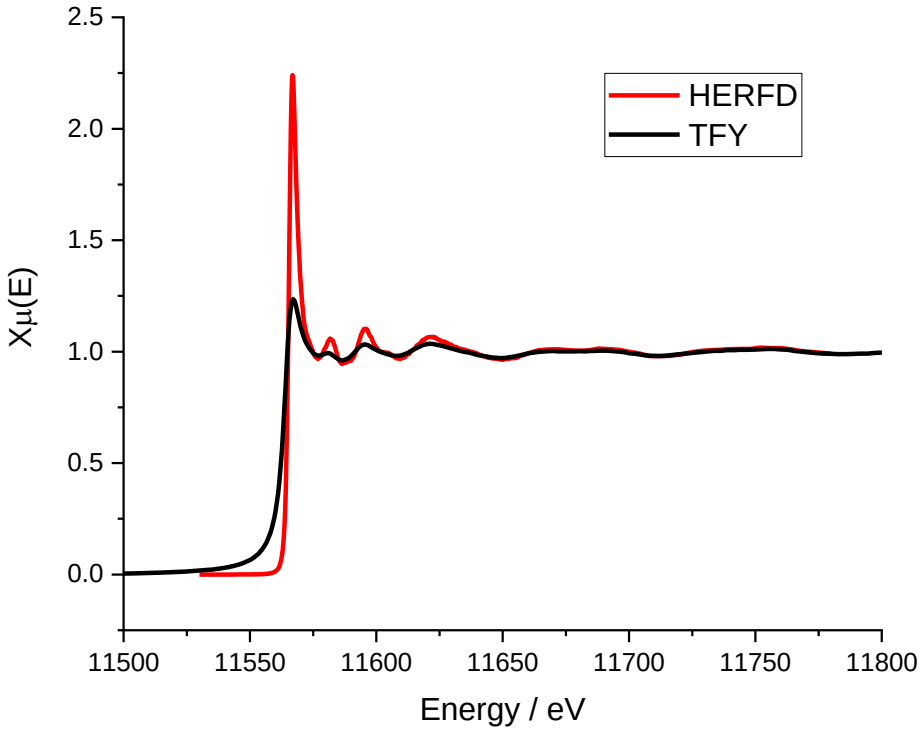

Figure 47. Black line shows data for Pt/C at -600 mV *vs.* SMSE for data collected at B18. Red line shows data for Pt/C at -600 mV *vs.* SMSE for data collected at I20. Only the XANES have been shown, as this is all that was collected on I20.

The spectra collected at +400 mV *vs.* SMSE highlight the use of the increased resolution. A fit using only two reference spectra is sufficient for the low resolution spectra (B18), but not the HERFD spectra (I20). Figure 48 and Figure 49 show the LCF for the TFY and HERFD data respectively. There is a reasonably good fit for the low resolution data (R-factor of 0.002), but there are large disparities for the HERFD data (R-factor of 0.059). For this reason the spectra

collected using TFY have been fit using only a 2 reference fit (using experimental reference spectra), but the HERFD data have been fit using DFT calculated spectra of intermediate oxides. Simulations were run using FDMNES to produce theoretical spectra, which have been compared to the measured data. An example of the code used is shown below (this example is for PtO_2):

```
"Range
-2. 0.2 3. 0.5 20. 2. 40.
Radius
5.0
Gamma_hole
3
Relativism
SCF
Edge
L3
Absorber
1
Molecule
       1          1          1          90 90 90
  78   0.000000   0.000000   0.000000   !    0.000000
  8    0.89489   -1.54990    1.04025    !    2.07006
  8   -0.89480    1.54995   -1.04025    !    2.07006
  8   -1.78979    0.00010    1.04025    !    2.07013
  8   -0.89480   -1.55005   -1.04025    !    2.07013
  8    0.89489    1.55010    1.04025    !    2.07021
  8    1.78988   -0.00005   -1.04025    !    2.07021
  78   2.68468    1.55000    0.00000    !    3.10000
  78  -2.68468    1.55000    0.00000    !    3.10000
  78   0.00000    3.10000    0.00000    !    3.10000
  78   2.68468   -1.55000    0.00000    !    3.10000
  78  -2.68468   -1.55000    0.00000    !    3.10000
  78   0.00000   -3.10000    0.00000    !    3.10000
  8   -0.89480    1.54995    3.12075    !    3.59751
  8    0.89489   -1.54990   -3.12075    !    3.59751
  8   -0.89480   -1.55005    3.12075    !    3.59756
```

```
  8   -1.78979    0.00010   -3.12075    !    3.59756
  8    1.78988   -0.00005    3.12075    !    3.59760
  8    0.89489    1.55010   -3.12075    !    3.59760
  8   -1.78979   -3.09990    1.04025    !    3.72757
  8   -3.57948   -0.00005   -1.04025    !    3.72757
  8    3.57957    0.00010    1.04025    !    3.72766
  8    1.78988    3.09995   -1.04025    !    3.72766
  8   -1.78979    3.10010    1.04025    !    3.72775
  8    1.78988   -3.10005   -1.04025    !    3.72775
 78    0.00000    0.00000    4.16100    !    4.16100
 78    0.00000    0.00000   -4.16100    !    4.16100
  8   -3.57948   -0.00005    3.12075    !    4.74887
  8   -1.78979   -3.09990   -3.12075    !    4.74887
  8    1.78988    3.09995    3.12075    !    4.74894
  8    3.57957    0.00010   -3.12075    !    4.74894
  8    1.78988   -3.10005    3.12075    !    4.74901
  8   -1.78979    3.10010   -3.12075    !    4.74901
  8    0.89489   -4.64990    1.04025    !    4.84814
  8   -3.57948    3.09995   -1.04025    !    4.84814
  8    3.57957   -3.09990    1.04025    !    4.84818
  8   -0.89480    4.64995   -1.04025    !    4.84818
  8   -4.47446   -1.54990    1.04025    !    4.84821
  8   -3.57948   -3.10005   -1.04025    !    4.84821
  8   -4.47446    1.55010    1.04025    !    4.84827
  8   -0.89480   -4.65005   -1.04025    !    4.84827
  8    3.57957    3.10010    1.04025    !    4.84831
  8    4.47455    1.54995   -1.04025    !    4.84831
  8    0.89489    4.65010    1.04025    !    4.84834
  8    4.47455   -1.55005   -1.04025    !    4.84834

! keywords for the convolution
 Convolution
E_cut
-.9
```

Ecent

60

Estart

-20

End”

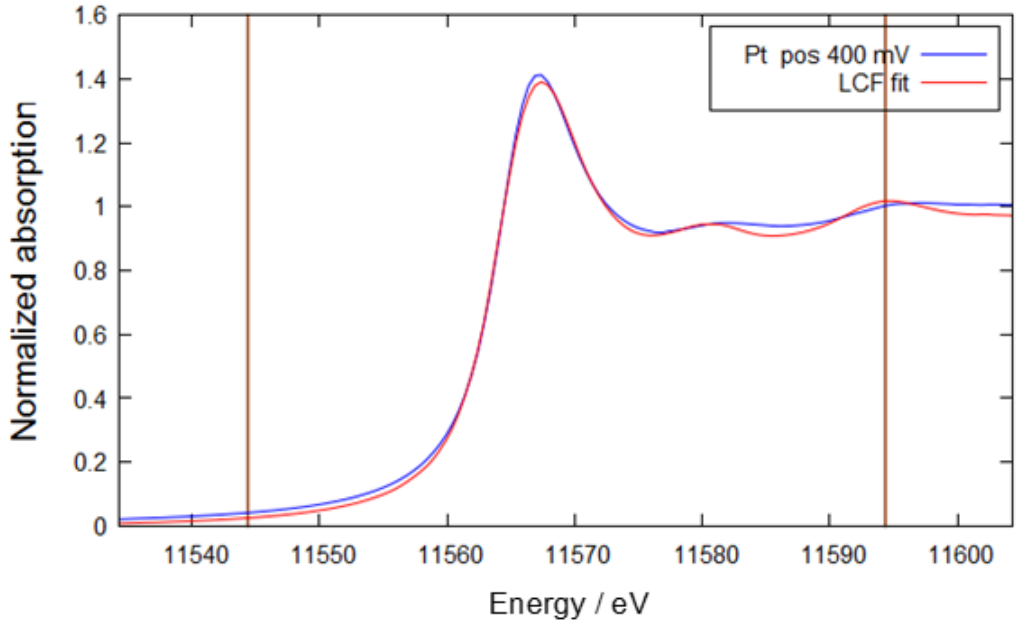

Figure 48. Blue line shows data for Pt/C at +400 mV *vs.* SMSE for data collected at B18. Red line shows the results of the LCF, vertical brown lines show the energy region over which the data have been fit.

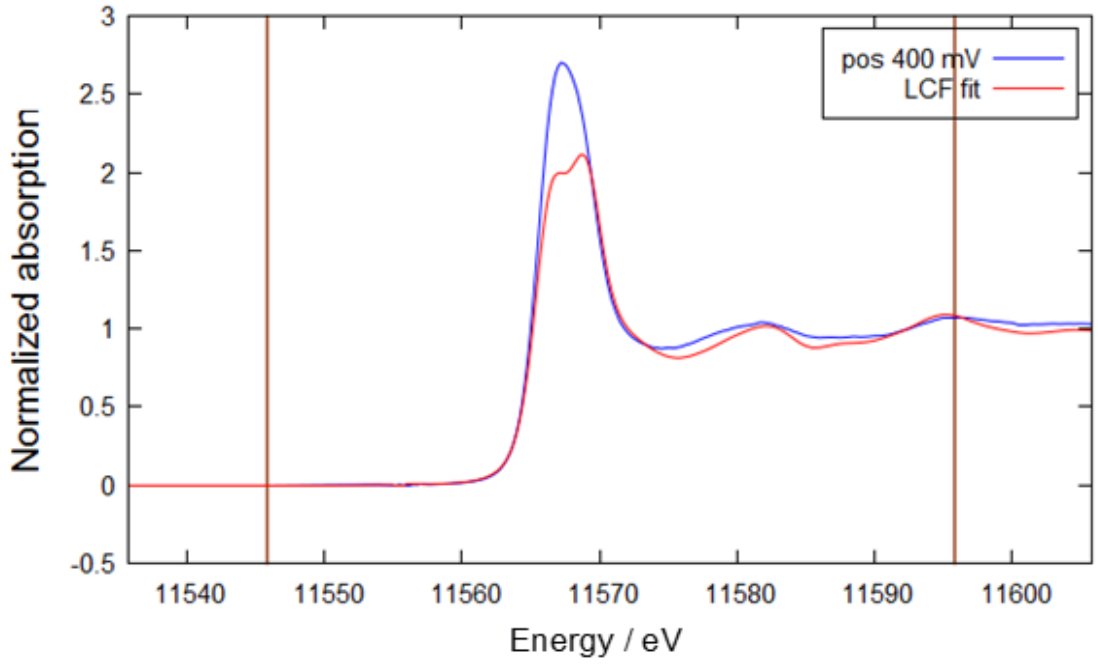

Figure 49. Blue line shows data for Pt/C at +400 mV *vs.* SMSE for data collected using I20. Red line shows the results of the LCF, vertical brown lines show the energy region over which the data have been fit.

4.3 Results and Discussion

4.3.1 EXAFS Oxide Measurements – B18

Here the EXAFS data have been fit to calculated spectra across the whole range of potentials measured and from these fits the average platinum oxidation state has been calculated. The data have been processed as described in the experimental section of this chapter. Figure 50 (top image) shows the k^2 χ weighted data for the reference spectra, and Figure 51 shows the k^2 χ weighted data for all the potentials (both in k-space). Although it is very hard to draw any quantitative conclusions from the data in this form, it is clear that there are potential dependent changes, in the average coordination environment around the Pt atoms. This is to be expected, because, as the nanoparticles are oxidised, the oxygen atoms are incorporated into the structure changing the environment. The *R*-space data are shown in Figure 52 for the sample data (Figure 50 bottom - for the reference data). More qualitative analysis can be conducted using the R-space representation of the spectra. Comparing the two extremes (-600 mV and + 600 mV *vs.* SMSE) there are clear differences, the first main peak in spectra from the most reduced spectrum (negative potential limit of the experiment, -600 mv *vs.* SMSE) is at ~ 2 Å and a second peak is observed around 2.7 Å, in contrast at the most oxidising potential (+600 mV *vs.* SMSE) has a first shell peak 1.6 Å with much smaller peaks at 2 and 2.7 Å. Although *R*-space should not be considered a radial distribution function, they are related and these changes can be associated with changes to the closest neighbour. This is likely to be the change from a Pt bulk structure to a structure including oxygen atoms, since the Pt-O bond is shorter than a Pt-Pt bond, these changes are clearly observable in the R-space reference spectra (Figure 50 bottom image). It should also be noted that there is a gradual change from the Pt foil structure to the PtO_2 structure starting from +200 mV *vs.* SMSE.

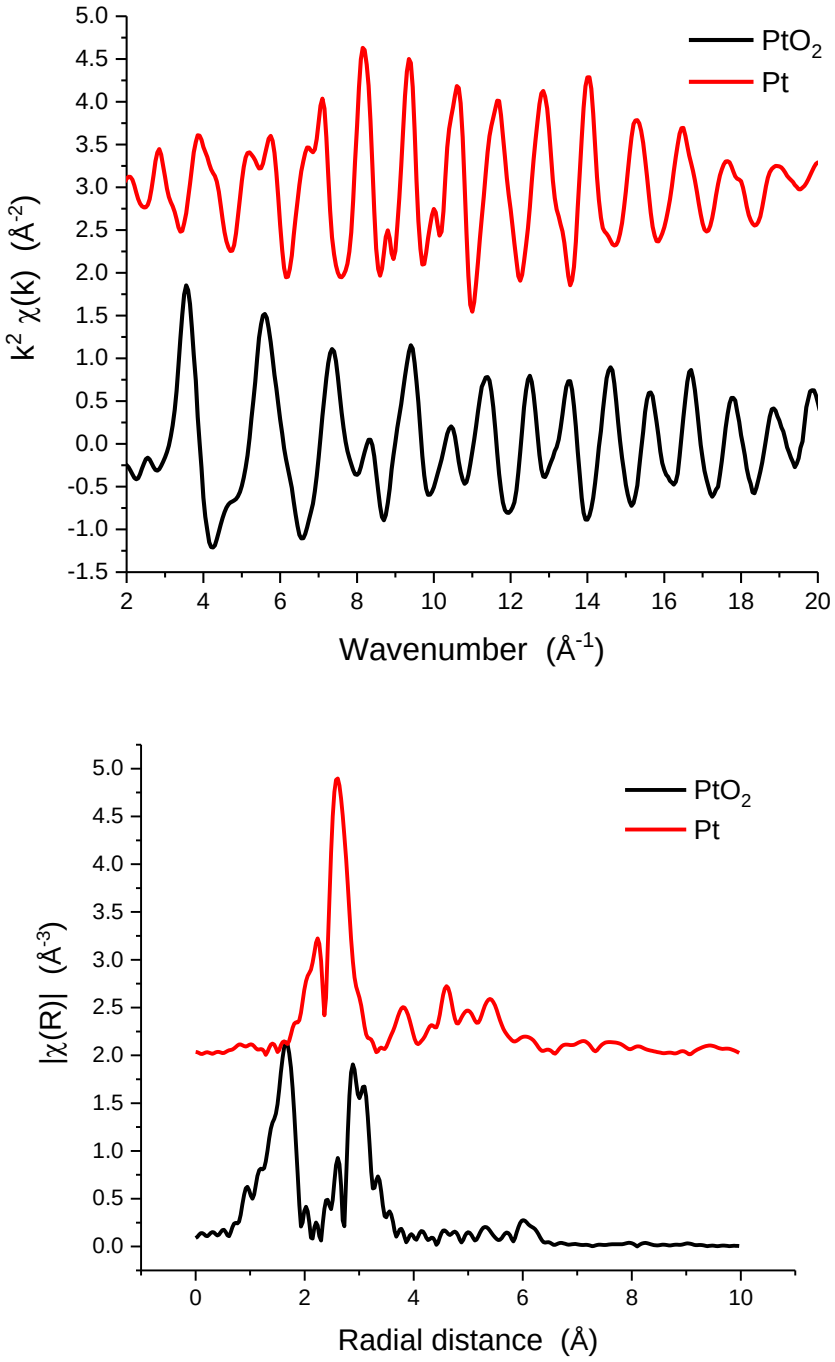

Figure 50. Top K^2–weighted EXAFS spectra of Pt foil (red – offset by 3) and PtO_2 (black) measured at Pt L_{III} edge, bottom – the Fourier transform of the EXAFS data presented in *R*-space, these are not phase corrected (Pt offset by 2).

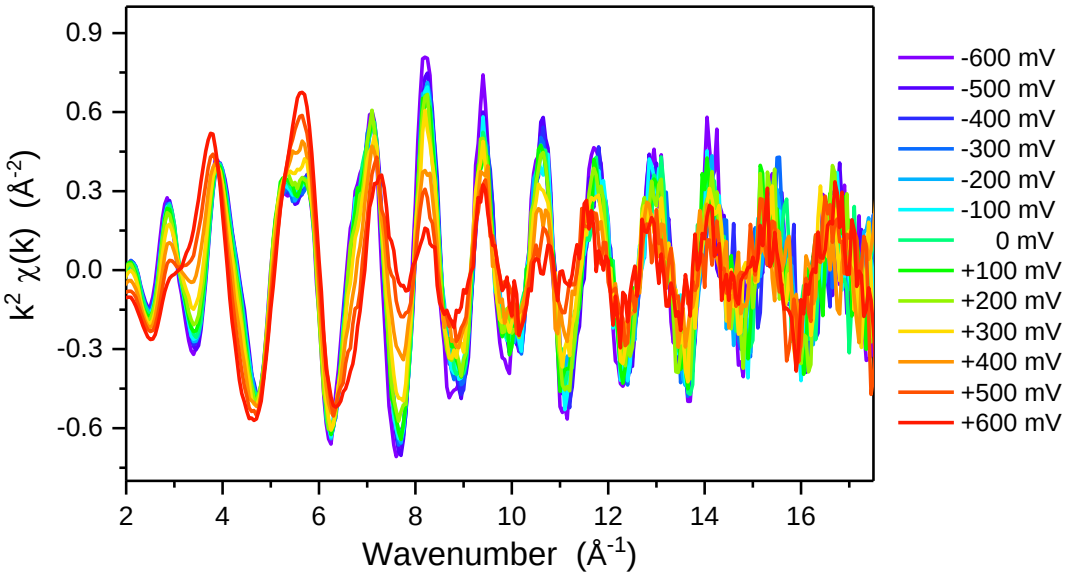

Figure 51. K^2–weighted EXAFS spectra of Pt/C measured at Pt L_{III} edge, held at potentials between -600 mV and +600 mV *vs.* SMSE

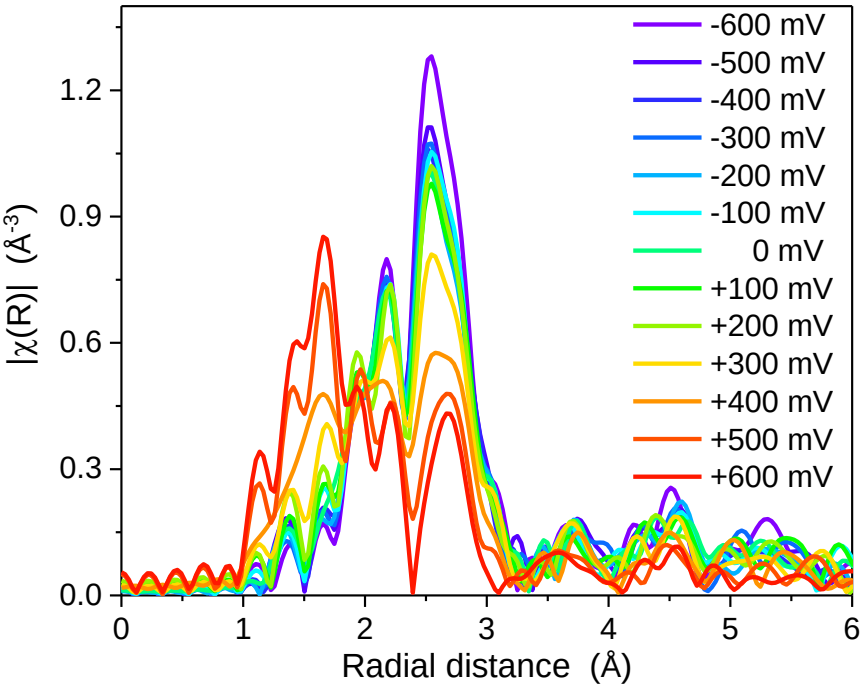

Figure 52. Fourier transform of the EXAFS spectra from Figure 51, presented in R-space, these are not phase corrected.

The EXAFS data were fitted using the Artemis program of the Demeter software package. The fitting model was based on the model developed by Inwood in 2017, a model that minimises the number of parameters being fit by the software, though recognising the symmetry of the FCC system.[26] Table 1 shows the fitting model developed by Inwood for a Pt nanoparticle and Figure 53 is a schematic showing what some of these scattering paths look like.

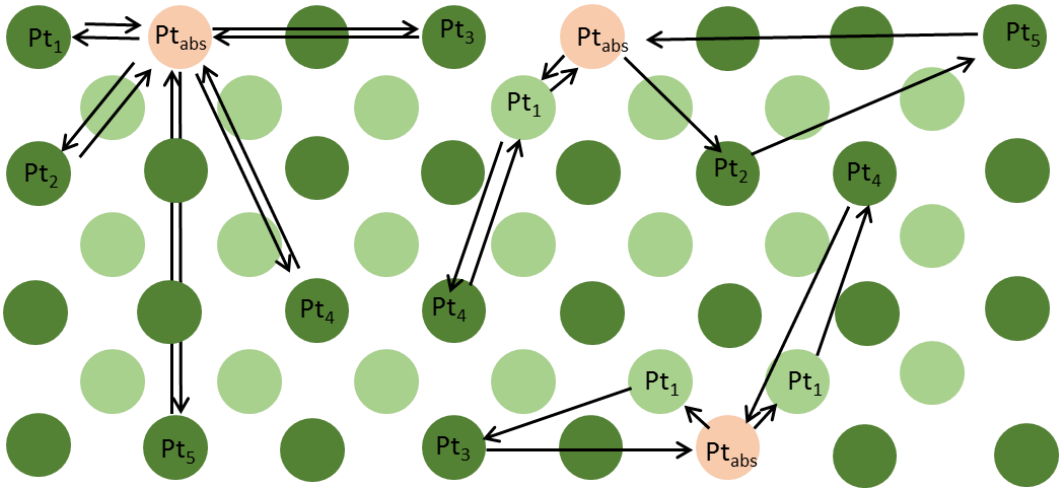

Figure 53. Schematic showing most of the scattering paths featured in Table 1. Single scattering paths are on the left and multiple scattering paths are on the right. The pink circles, labelled Pt_{abs} represent the absorbing atoms, the dark green circles depict Pt atoms in the same plane as the absorbing atom, and the pale green circles represent Pt atoms beneath the plane.

Table 1. Lists the constrained model used to fit the data with minimal variables.

Scattering path	*N*	σ^2
Pt_{abs}-Pt_1-Pt_{abs}	*N1*	*SS1*
Pt_{abs}-Pt_2-Pt_{abs}	*N2*	*SS2*
Pt_{abs}-Pt_3-Pt_{abs}	*N3*	*SS3*
Pt_{abs}-Pt_4-Pt_{abs}	*N4*	*SS4*
Pt_{abs}-Pt_{1a}-Pt_{1b}-Pt_{abs} (acute triangle)	1/3 $N1^2$	1.5 *SS1*
Pt_{abs}-Pt_{1a}-Pt_{1c}-Pt_{abs} (obtuse triangle)	1/3 $N1^2$	*SS1*+ ½ *SS3*
Pt_{abs}-Pt_1-Pt_3-Pt_{abs} (obtuse triangle)	1/3 *N1* * *N3*	*SS1*+ ½ *SS3*
Pt_{abs}-Pt_{1a}-Pt_{1d}-Pt_{abs} (non-forward, linear)	1/12 $N1^2$	2 *SS1*
Pt_{abs}-Pt_1-Pt_4-Pt_{abs} (forward, linear)	1/6 *N1* * *N4*	*SS4*
Pt_{abs}-Pt_{1a}-Pt_{1d}-Pt_{abs} (forward through absorber, linear)	1/12 $N1^2$	2 *SS1*
Pt_{abs}-Pt_{1a}-Pt_4-Pt_{1a}-Pt_{abs} (double forward, linear)	1/12 *N1* * *N4*	*SS4*
Pt_{abs}-Pt_{1a}-Pt_3-Pt_{1a}-Pt_{abs} (dog-leg)	1/6 *N1* * *N3*	4 *SS1*

Four additional scattering paths were included to account for the surface oxide formed when the material is at highly oxidising potentials (300- 600 mV *vs*. SMSE). Table 2 shows the additional scattering paths used. Three of these are the three nearest neighbours from the PtO_2 structure two Pt – O paths and one Pt – Pt path, the final path is a Pt – Pt path from bulk Pt allowed to have a different bond length from those in the Inwood model. The variation in the Pt – Pt bond length is very important as it accounts for the interface between the Pt and PtO_2 structures where it is reasonable to expect an intermediate bond length, due to the oxidised platinum having a smaller radius.

Table 2. Additional variables to the model used to fit the oxidised samples

Scattering path	***N***	σ^2
Pt_{abs}-O_1 -Pt_{abs}	O1	SSO1
Pt_{abs}-Pt_1- Pt_{abs}	PtO	SSO1
Pt_{abs}-O_2 -Pt_{abs}	O2	SSO1
Pt_{abs}-Pt_1- Pt_{abs}	In	SSIn1

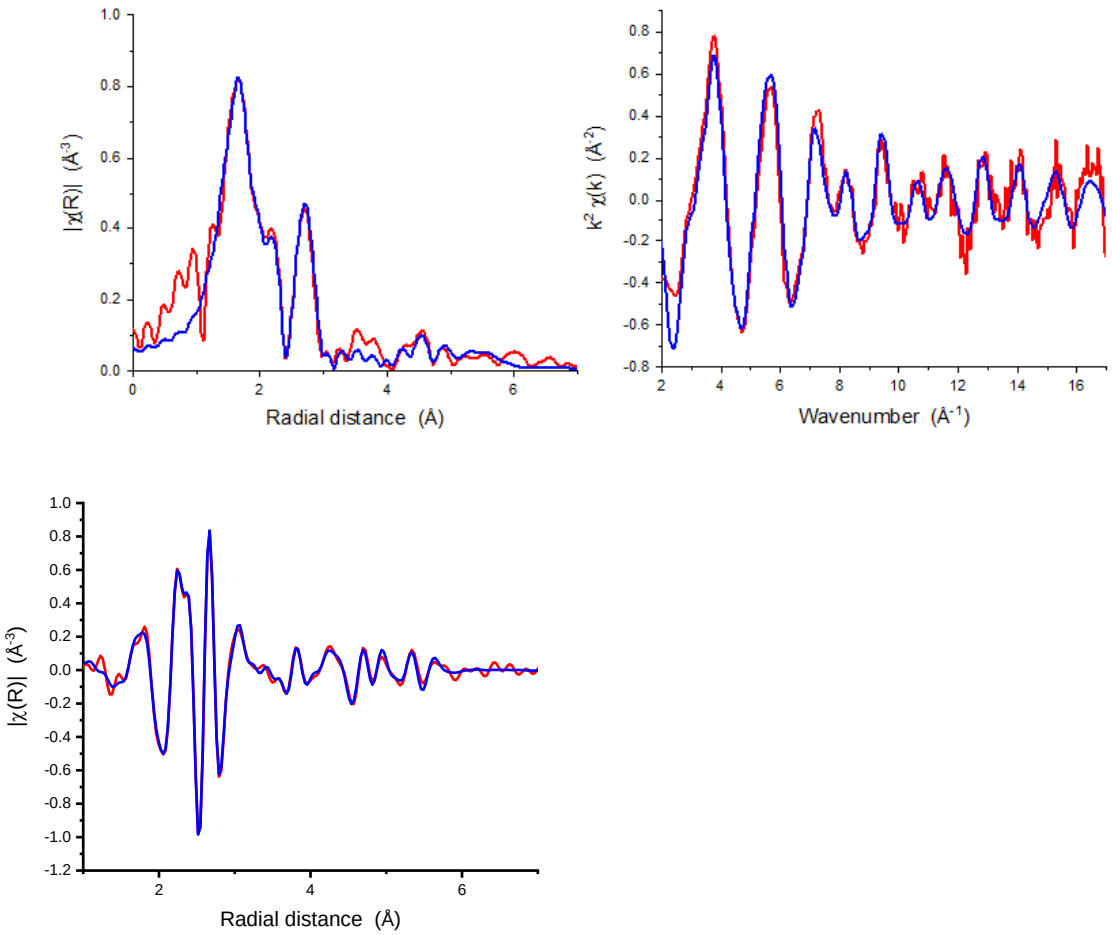

Figure 54. EXAFS data and fits of +600 mV *vs.* SMSE. Top right - *R*-space of K^2–weighted (red line – data, blue line - fit), top left - magnitude of K^2–weighted k-space (red line – data, blue line - fit) and bottom left - real K^2–weighted k-space (red line – data, blue line - fit).

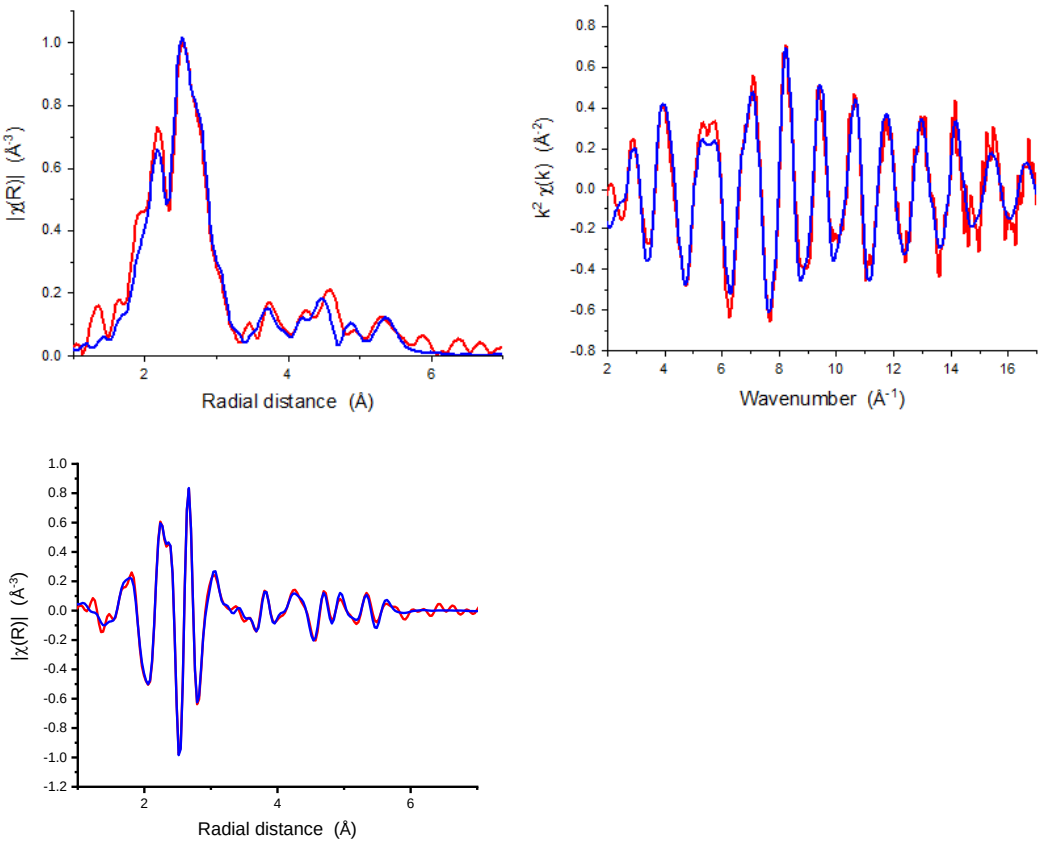

Figure 55. EXAFS data and fits of -200 mV *vs.* SMSE. Top right - *R*-space of K^2–weighted (red line – data, blue line - fit), top left - magnitude of K^2–weighted k-space (red line – data, blue line - fit) and bottom left - real K^2–weighted k-space (red line – data, blue line - fit).

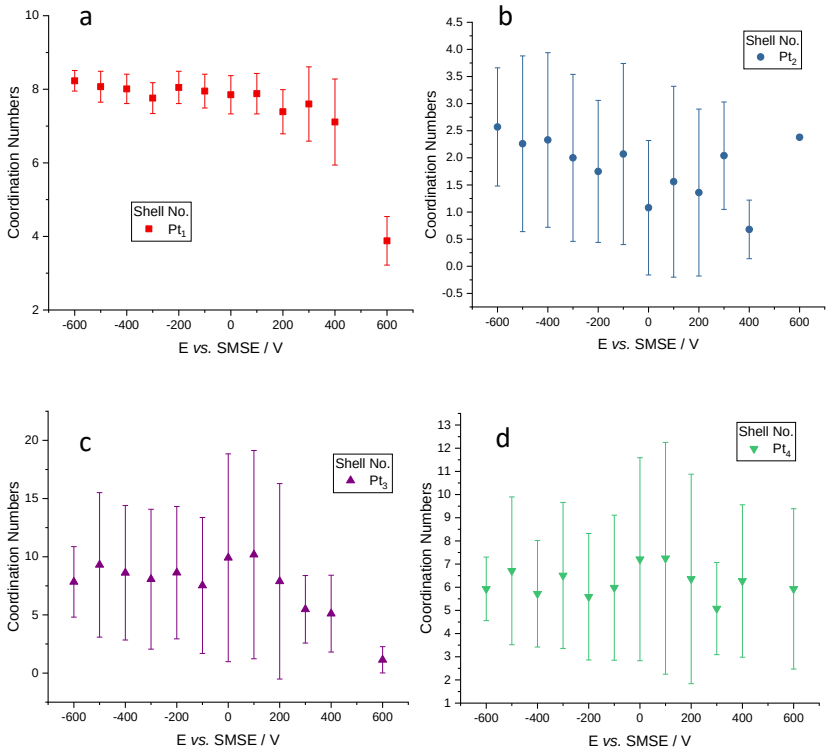

Figure 56. Showing the coordination numbers as a function of potential for the Pt shells 1 to 4 (a to d respectively). The R-factors ranged between 0.01 and 0.06.

Figure 54 and Figure 55 show the data and fits for two spectra a spectrum at +600 mV *vs.* SMSE where there is the most oxide in the sample, and at -200 mV *vs.* SMSE which is similar to bulk platinum. Figure 56 displays the results of the EXAFS fitting and Figure 57 for the 1st and 3rd Pt-Pt coordination number ratio. These values are important as they allow an estimate of the particle size to be calculated according to the model by Jentys (shown in Table 4), where the particles are assumed to be spherical.[14] The ratio decreases from 2 (the bulk value, when CN1 is 12 and CN2 is 24) as the particle gets smaller. In this experiment the particle is not getting smaller, but the amount of the particle that can be described as pure Pt is decreasing. This suggests that the Pt is being oxidised to a "core-shell" like structure, where the core is pure Pt and the shell is Pt oxide (PtO_2 for this model). An alternate explanation is that some of the Pt particles are fully oxidised to PtO_2, whilst some remain unchanged as Pt. However, this explanation is not consistent with other electrochemical measurements of the catalyst electrodes, such as the electrochemical stripping of a H_{ads} monolayer in this work, and has thus been rejected. Table 3 shows the results of the EXAFS fits for the -200 and +600 mV *vs.* SMSE. It should be noted that there are larger errors for the coordination numbers further from the absorbing atom. The Pt-O paths have only been incorporated into the fits for the most positive potentials, as it is not reasonable to include Pt-O bonds at the more reducing potentials (when the Pt-O paths were included in the analysis of these data meaningful results were not obtained with some impossible coordination numbers).

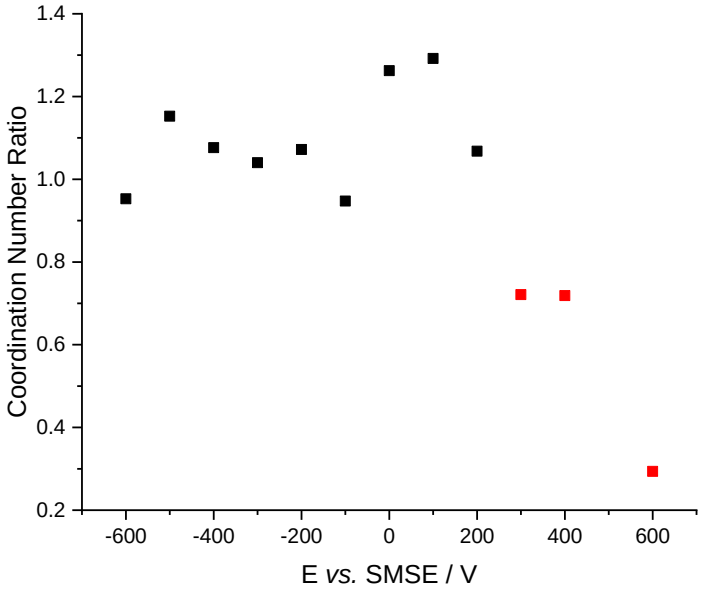

Figure 57. Showing the ratio of the 1st and 3rd coordination numbers for Pt. The red points indicate where the oxide paths were included.

Table 3. The results of the EXAFS fitting for -200 mV (a double layer value) and +600 mV (most oxidised) *vs.* SMSE. * The calculated error was unrealistically small and therefore has not been included.

Parameter	-200 mV *vs.* SMSE	+600 mV *vs.* SMSE
N1	8.05 ± 0.44	3.88 ± 0.66
N2	1.75 ± 1.31	2.38*
N3	8.63 ± 5.69	1.14 ± 1.13
N4	5.59 ± 2.73	5.93 ± 3.46
O1	N/A	2.95 ± 0.20
O2	N/A	6.88 ± 1.85
In	N/A	1.37 ± 0.68
R-factor	0.03	0.02

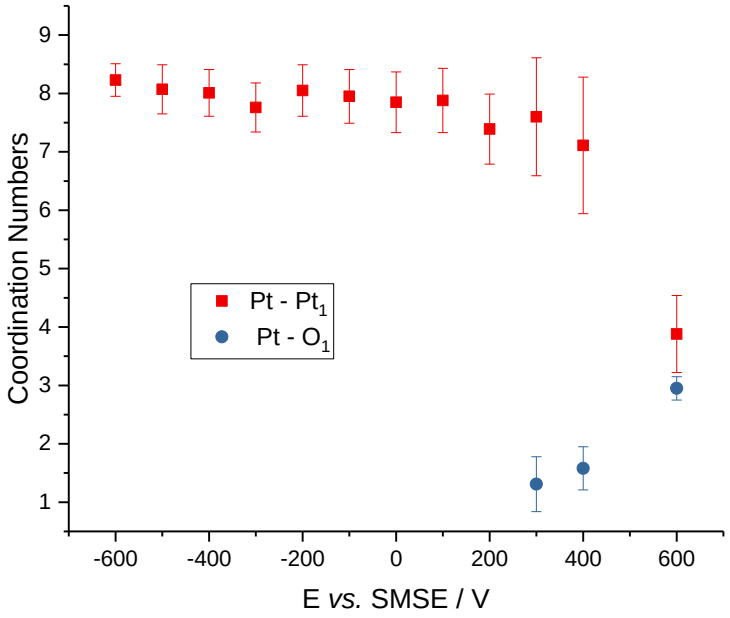

Figure 58. Coordination numbers for the Pt-Pt$_1$ and Pt-O$_1$ shells to show the onset of oxide formation (Pt-O$_1$) and contraction of the Pt core size (Pt-Pt$_1$).

Observing Figure 56, Figure 57 and Figure 58 it should be noted that there is very little change to the EXAFS fitting results between the potentials -600 and +100 *vs.* SMSE with the CN1 8.9-9.1 (Figure 56 a) and the ratio fluctuating around 1.1 (Figure 57). There is a contribution from the oxide as the potential increases past 200 mV *vs.* SMSE. When the potential is at 200 mV *vs.* SMSE the fit of the Pt is still more representative than the fit including oxygen neighbours, but the CN1 for the Pt-Pt starts to fall. This decrease in seen again for 400 mV and even more so for 600 mV *vs.* SMSE, and on its own suggests that the particle is getting smaller. Table 4 shows predicted coordination numbers for a range of particle sizes and the change observed in Figure 58 (based on CN1) would suggest going from a ~2 nm particle to one less than 1 nm in size.

Using an alternative model, one proposed by Beale, which uses only the 1st shell coordination number to estimate the size of the particle a similar result is obtained.[16] Where the Pt is assumed to be spherical and starts as a 1.5-2 nm sphere and gradually gets smaller. The amount of the particle which can be described as Pt is only 0.3-0.6 nm, which is similar but smaller than the Jentys model predicts.

There are two main caveats that need to be considered along with this result. First, is that the parameter being measured only accounts for the Pt-Pt bonds in FCC like platinum, and the oxidised Pt is not leaving the particle, only changing environment, so the particle is more likely growing in overall size as oxygen is incorporated into the structure. Second, the model used to create Table 4 assumes all the Pt atoms are in the pure Pt FCC structure. Since the atoms that are oxidised are now in the shell of the core shell structure, and EXAFS is a bulk technique the atoms

is the shell of the particle will distort the values for the Pt core. What is clear though is that the core is getting smaller and the shell is growing.

Table 4. Displays the predicted 1st and 3rd coordination numbers for a range of Pt nanoparticle sizes based on the model by Jentys.[14]

Size / nm	No. of Atoms	CN1	CN3	CN3:CN1
0.83	13	5.18	3.41	0.66
1.39	55	7.75	8.19	1.06
1.75	135	8.64	11.33	1.31
2.03	201	8.94	12.61	1.41
2.57	429	9.47	14.99	1.58
3.05	767	9.91	16.88	1 .70
3.26	959	10.09	17.62	1.75
	Bulk	12	24	2

Figure 58 infers that as the sample is held at more and more oxidising potentials, the average number of Pt-O bonds increases. This will be used to estimate an average oxidation state, in bulk PtO_2 each Pt atom has 6 oxygens coordinated, so here oxidation state will be estimated based on the number of oxygen atoms coordinating, with 0 atoms coordinating being an oxidation state of 0 and 6 coordinating oxygens being an oxidation state of +4. These will be displayed and discussed in the next sections. This method will be compared to more conventional methods later in the chapter.

The fits at the most positive potentials also have information about the interface between the core and the shell, the Pt and the PtO_2 in this model. Importantly, this model calculates a value for the Pt-Pt bond length at the interface, coordinating to an oxidised platinum atom with a smaller radius (radius values Pt = 135 pm, Pt^{2+} = 94 pm, and Pt^{4+} = 77 pm).[28,29]

4.3.2 XANES measurements from B18 - Oxide

The XANES (X-ray Absorption Near Edge Structure) region of an X-ray Absorption spectrum (XAS) contains information about the oxidation state of the target atom. Since this is a per atom

technique any values for oxidation state should reflect the average oxidation states of all the absorber atoms (Pt in this case) and thus non-integer values are to be expected.

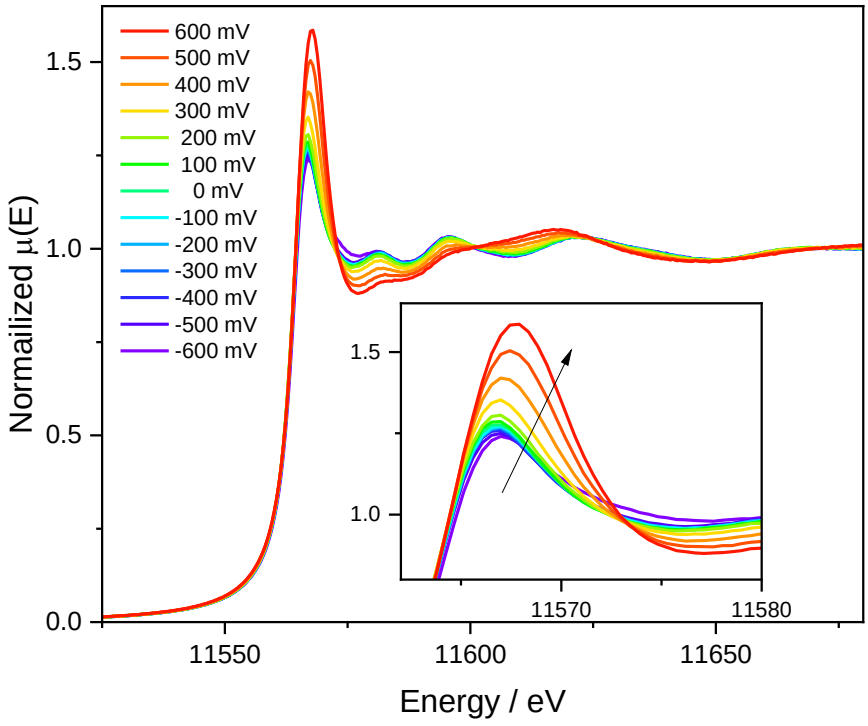

Figure 59. XAS spectra of Pt/C measured at Pt L_{III} edge on B18, held at potentials between -600 mV and +600 mV *vs.* SMSE. With zoomed in region of the white line.

Figure 59 shows the normalised XAS spectra for the XANES region for the Pt/C catalysts over a wide range of potentials (-600 mV to +600 mV *vs.* SMSE). There is a subtle change observed in the spectrum for -600 mV *vs.* SMSE (purple line) just after the edge (at approximately 11575 eV) with additional intensity observed. Apart from that subtle change, the rest of the spectra from -500 mV to +100 mV *vs.* SMSE show little observable change when viewed in E-space. The spectra from +200 mV to +600 mV *vs.* SMSE show increasing white line (first peak ~11564 eV) intensities and deepening of the first undulation (~11575 eV). The position of the white line shifts to higher energy as the potential applied to the electrode is more positive. This shift in white line intensity is more easily seen in Figure 60, where the first derivative is plotted. The peak of the first derivative was used as the edge positon, this is directly linked to the energy of the Pt $2p_{3/2}$ electronic state relative to the Fermi level. The linearity of the relationship between the oxidation state and the orbital energy of the core electrons allows us the make these estimations.[3]

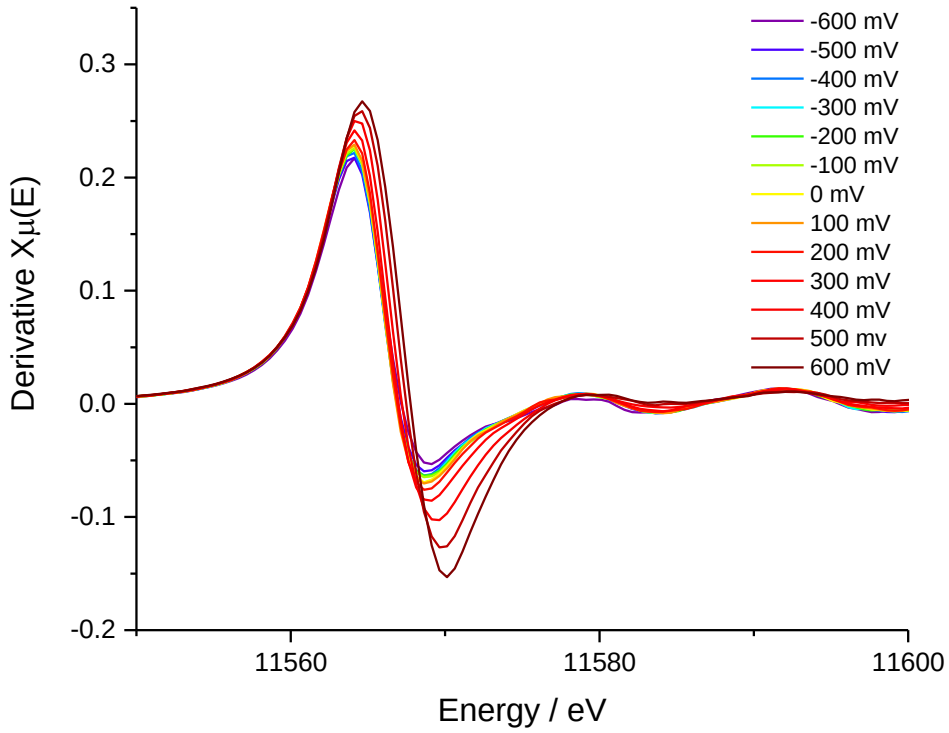

Figure 60. First derivative of the XAS spectra in Figure 59.

The edge positions of the references samples (Pt foil and PtO_2) were plotted *vs.* their known oxidation state and used as a calibration plot of the sample data to interpolate the average oxidation state of the catalysts, the results are shown in Figure 61. This crude analysis shows the oxidation state of the Pt/C nanoparticles as 0 from -500 mV to 100 mV *vs.* SMSE, which is to be expected from the voltammetry and the qualitative analysis of the spectra in Figure 59. The average platinum oxidation state increases with potential from +200 mV to +600 mV *vs.* SMSE, this also aligns with the electrochemistry, as there is a peak associated with platinum oxidation at this potential. The point for -600 mV *vs.* SMSE has been excluded from this plot as an anomaly, as it is not reasonable to suggest that the sample when held at -600 mV *vs.* SMSE to be more oxidised than all the other spectra from 500 mV to 100 mV *vs.* SMSE. This is probably due to the surface of the Pt being covered in H and will be discussed in more detail in section 1.3.4.

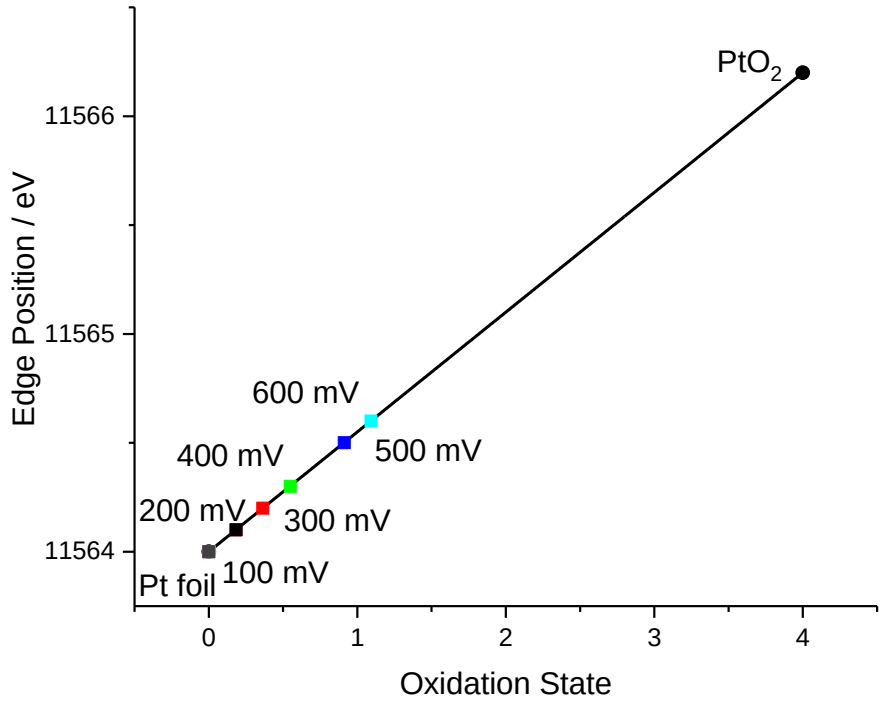

Figure 61. Plot of edge position *vs*. oxidation state for Pt foil and PtO_2 and a linear fir which was used to interpolate average *in situ* values for oxidation state. The point for -600 mV *vs.* SMSE has been excluded from this plot as an anomaly owing to the presence of H_{ads} at this potential.

Using the edge position is a good estimate of the oxidation state, but it does only use one data point from each spectrum, linear combination fitting (LCF) uses the whole XANES region -20 eV to +30 eV of the edge energy (shown in Figure 48 and Figure 49).

Figure 62 to Figure 65 show the linear combination fits for four selected potentials of the conventional XANES. The results of the two component (Pt foil and PtO_2) LCF are shown in and Figure 66, with the blue dots showing the proportion of the fit from the Pt foil and the red squares showing the proportion of the fit from the platinum oxide. The trend shown in Figure 66 is in agreement with the quantitative analysis from the edge position showing an initial deviation from the Pt foil at +200 mV *vs.* SMSE followed by a steady increase of the oxidation state until the final potential (+600 mV *vs.* SMSE).

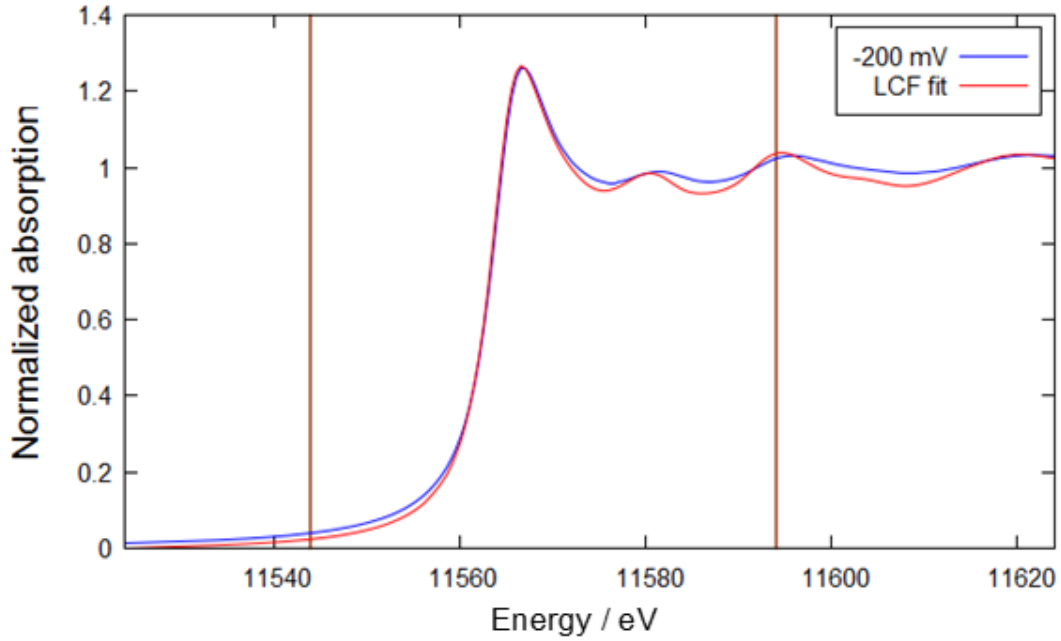

Figure 62. Blue line shows data for Pt/C at -200 mV *vs.* SMSE for data collected at B18. Red line shows the results of the LCF, vertical brown lines show the energy region over which the data have been fit. R-factor is 0.002.

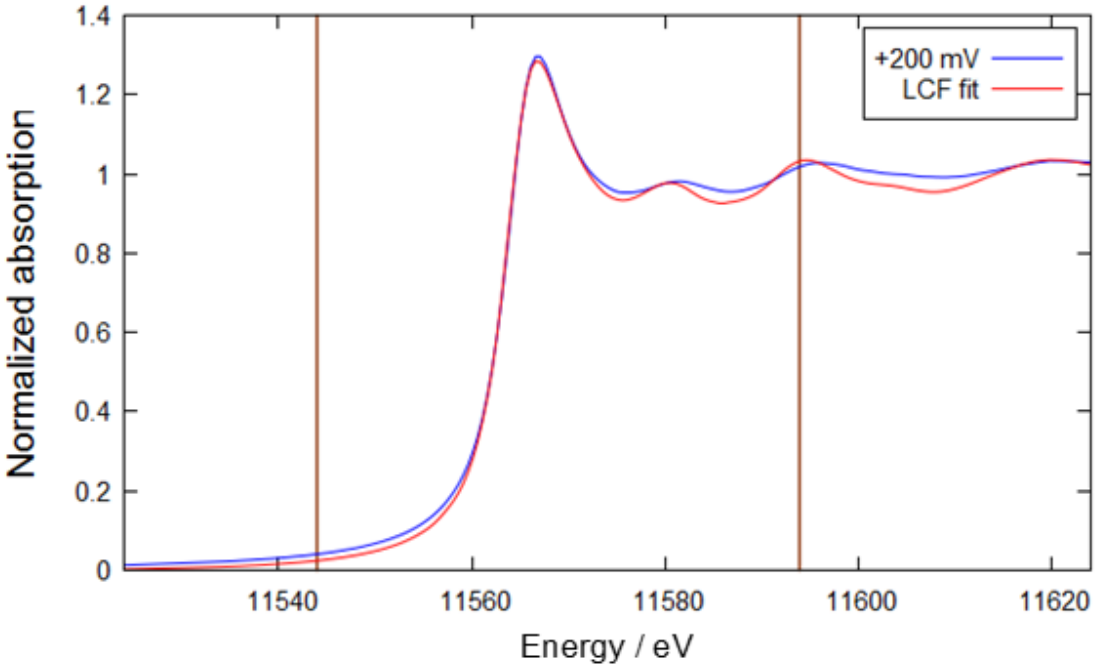

Figure 63. Blue line shows data for Pt/C at +200 mV *vs.* SMSE for data collected at B18. Red line shows the results of the LCF, vertical brown lines show the energy region over which the data have been fit. R-factor is 0.002.

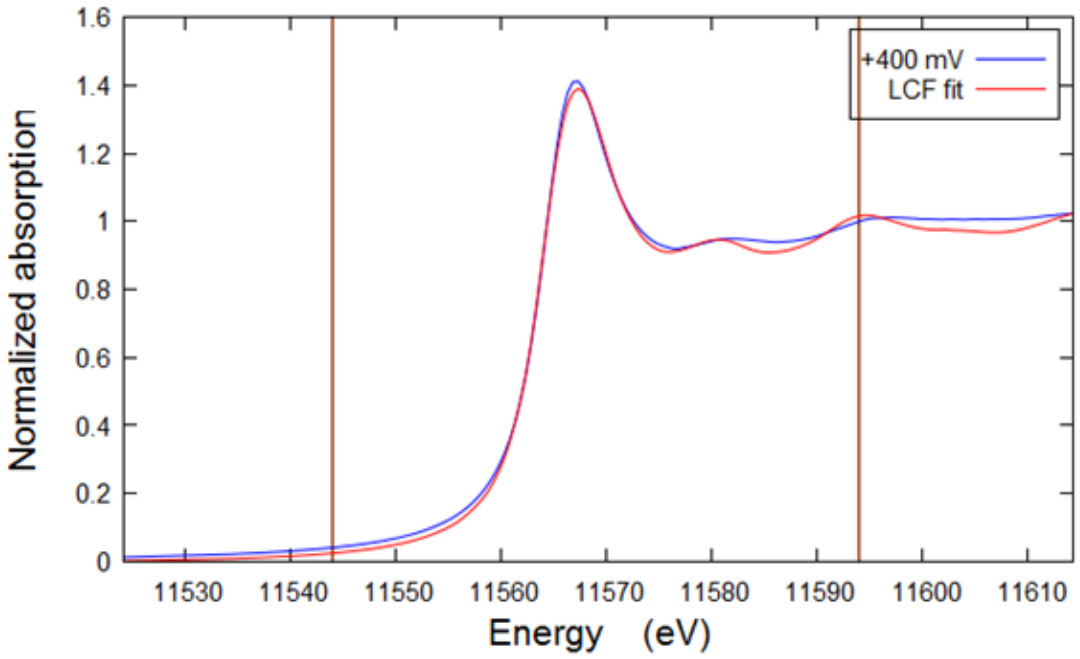

Figure 64. Blue line shows data for Pt/C at +400 mV *vs.* SMSE for data collected at B18. Red line shows the results of the LCF, vertical brown lines show the energy region over which the data have been fit. R-factor is 0.002.

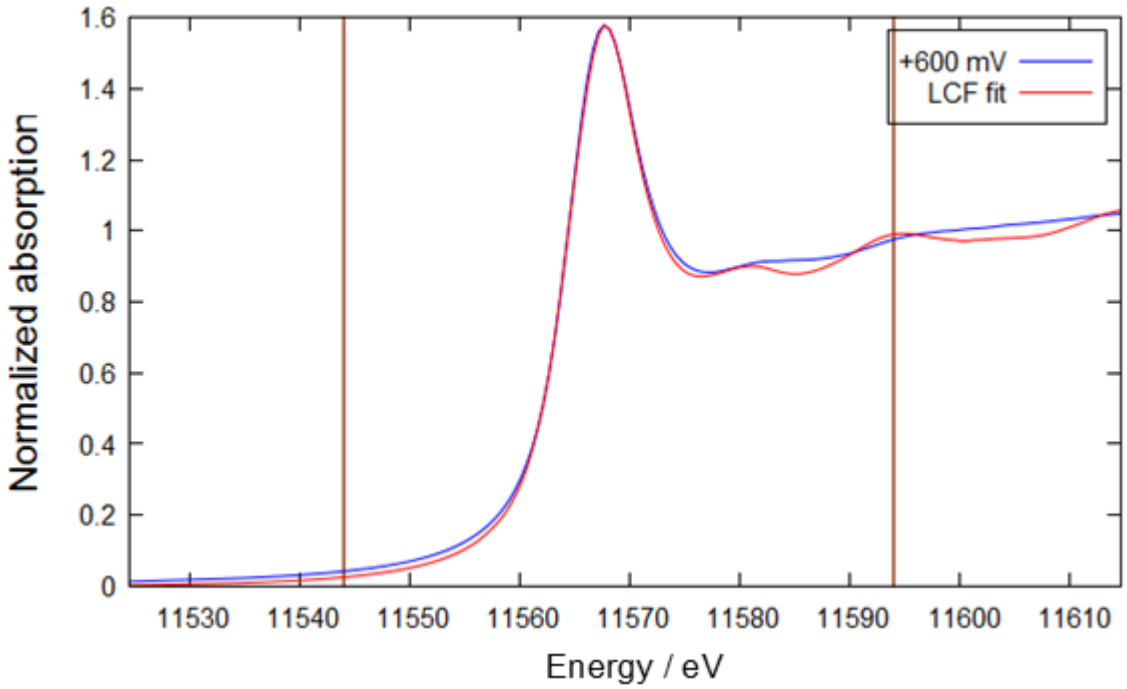

Figure 65. Blue line shows data for Pt/C at +600 mV *vs.* SMSE for data collected at B18. Red line shows the results of the LCF, vertical brown lines show the energy region over which the data have been fit. R-factor is 0.002.

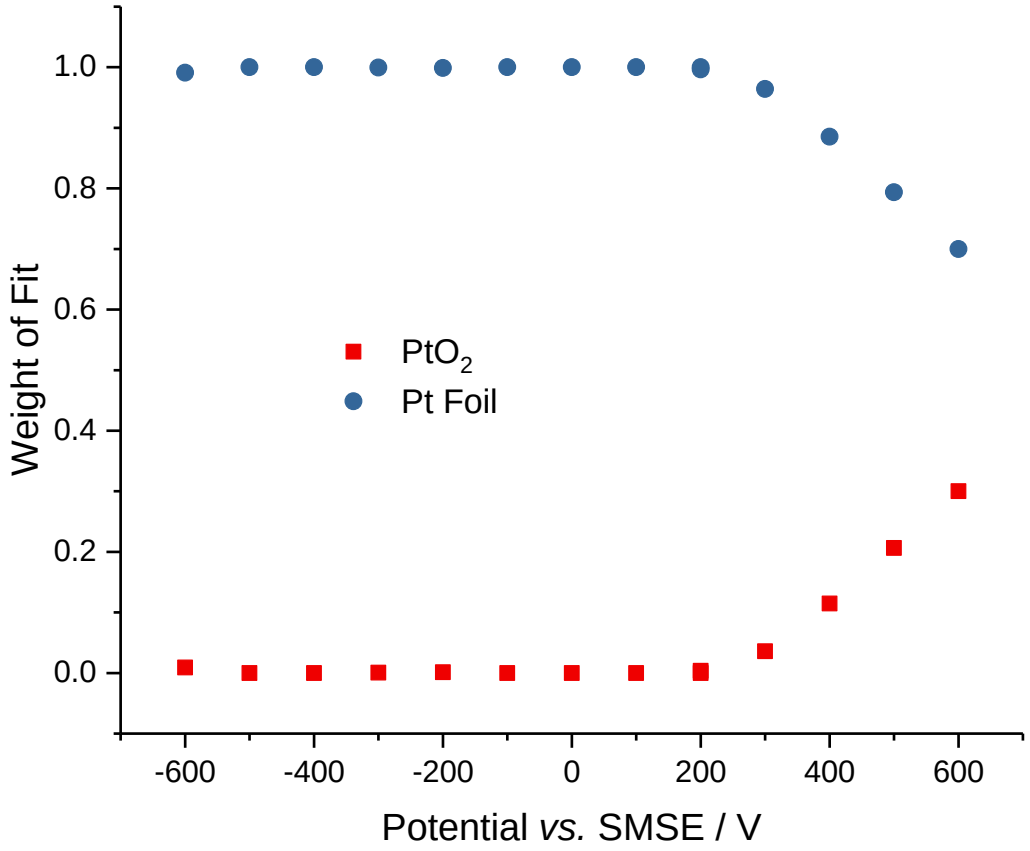

Figure 66. The results of the linear combination fit for the B18 spectra plotted *vs*. electrode potential. The R-factors ranged from 0.002-0.005.

It should be noted that this method, as it uses more data points than the one used for the edge position analysis, is less perturbed by the -600 mV spectrum which has a higher energy edge position, but bares little other resemblance to the PtO_2 spectrum. Figure 67 shows the calculated average oxidation state of the Pt is plotted *vs.* potential for all three methods discussed so far. The edge position method shows a sharper increase of oxidation state at +200 m V *vs.* SMSE followed by a steady increase of average oxidation state. The LCF method shows only slight oxidation at +200 m V *vs.* SMSE, but the changes over the next data points are so significant that by the final data point it is suggesting a more oxidised sample than the edge position method. Overall, both these methods give a similar account for the oxidation state of the sample over this potential range. The EXAFS predicts a higher average oxidation state than the XANES. This may be due to the assumption that every oxygen coordinated to a Pt atom is in the -2 oxidation state, as it is in PtO_2, which may not be accurate, as there may be other oxygen containing species such as PtOH.

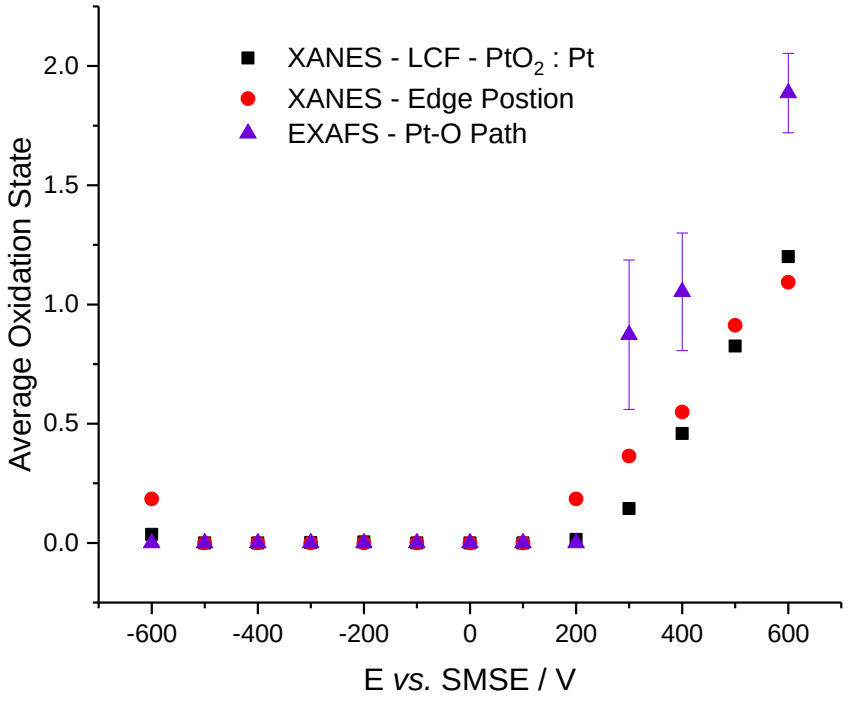

Figure 67. Showing the average oxidation state calculated from the spectra from the edge position method, the LCF method and from the EXAFS.

4.3.3 XANES Measurements from I20 - Oxide

In this section high energy resolution fluorescence detection data collected on beamline I20 at the Diamond Light Source will be presented and discussed. Figure 68 shows the normalised data and immediately it is clear there are differences from the data presented in section 4.3.2 and Figure 59 with the white line being significantly more pronounced on the scale of 2-3 of the normalised units compared to 1.2 -1.6. This is due to the higher energy resolution and reduced experimental broadening. The effects of increased resolution are most clear to see in Figure 69 where the high-resolution data has an asymmetrical peak.

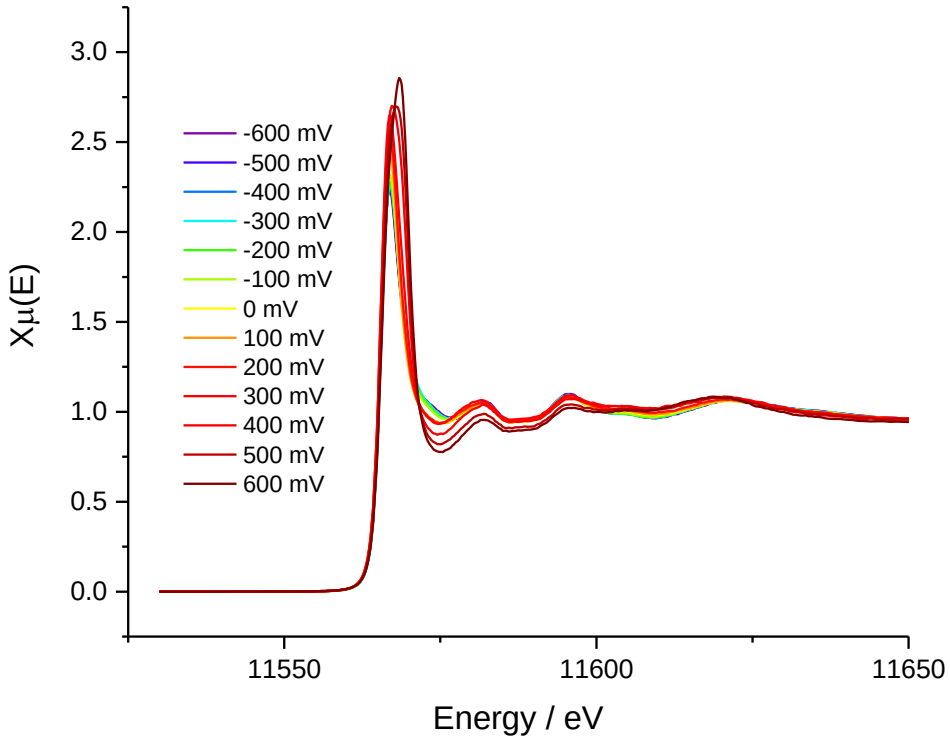

Figure 68. HERFD XAS spectra of Pt/C measured at Pt L_{III} edge on I20, held at potentials between -600 mV and +600 mV *vs.* SMSE. The data had been normalised.

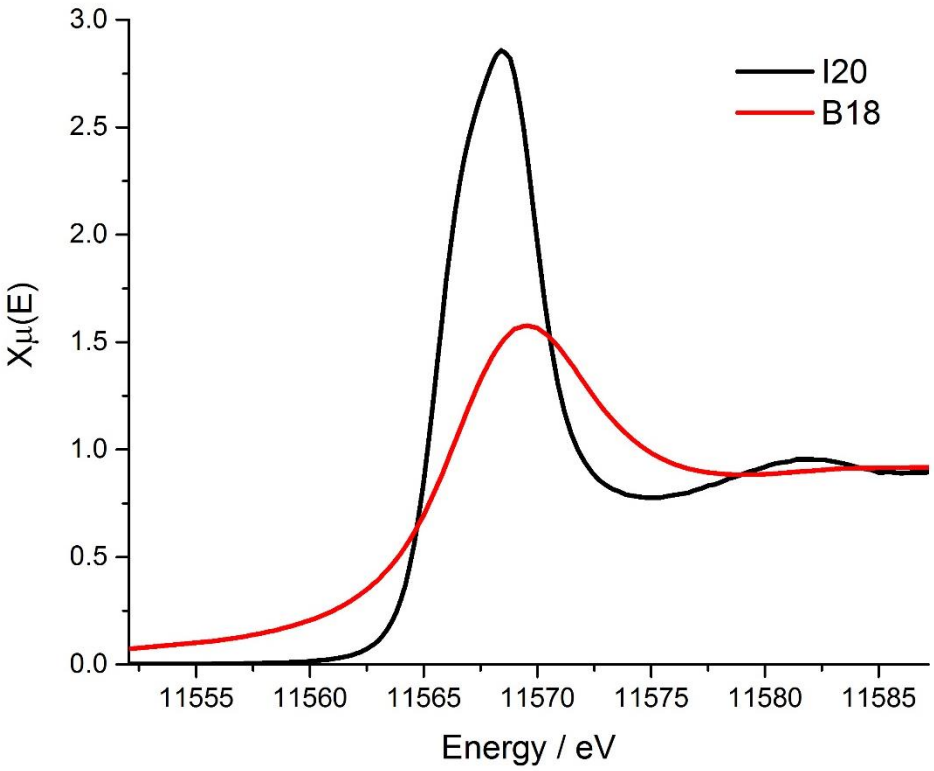

Figure 69. I20 and B18 spectra of Pt/C measured at Pt L_{III} edge on I20, held at +600 mV *vs.* SMSE. The data had been normalised.

As a result of the increased energy resolution, the edge position analysis performed in section 4.3.2 is not useful for this data set. This is because the spectra can resolve both the Pt and PtO_2 peak (and intermediate oxides) so clearly, and in this experiment there is always enough Pt to see the peak at 11564 eV the edge position does not move with potential. The spectra have, therefore, been analysed using linear commination fitting. Simulated spectra were calculated using the FDMNES code and used as reference files for the LCF.

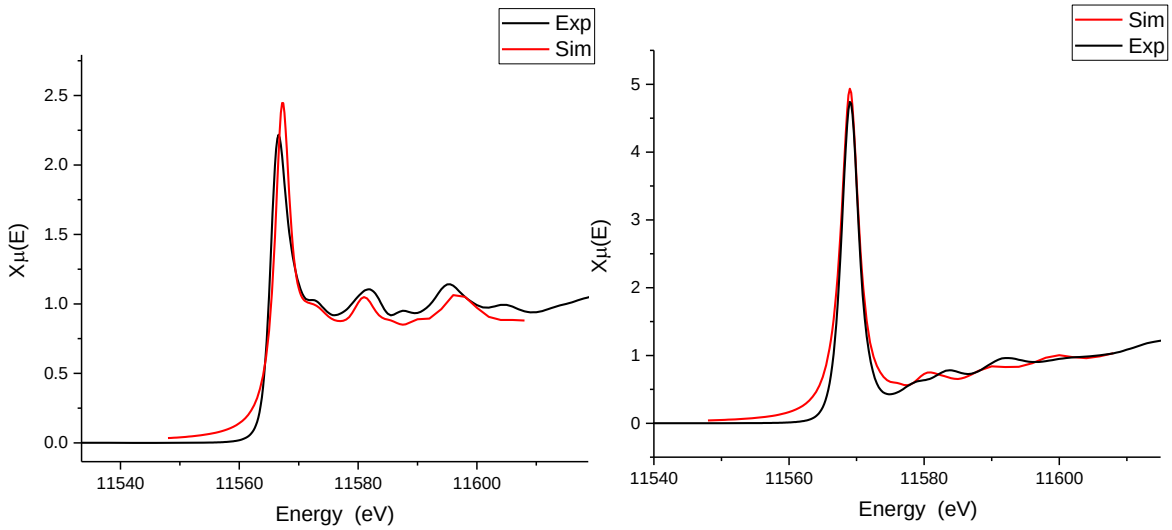

Figure 70. Shows experimental and simulated spectra for Pt (left) and PtO_2 right. The simulated spectra was calculated using the FDMNES code.

Figure 70 presents the results of the FDMNES calculations and compares them to the experimentally collected spectra. The correlation is not perfect, but the results are very similar. It should be noted that the only change between the two calculations was the input structure, this is very important as the same parameters will be used to calculate spectra for structures for which experimental data is not available. The input structures were obtained from the ICSD and were selected as structures measured using XRD.[30–32] Knowing that the same parameters simulate the experimental data well across a wide range of oxidation states gives confidence that the intermediate oxide structures simulated XANES will be broadly accurate.

A simulation of the spectrum of Pt_3O_4 was calculated and is very similar qualitatively to the most oxidising potential the samples were measured at. PtO PtOH and PtH were also simulated using the same model, but these spectra did not improve the LCF and were therefore not considered any longer for this analysis. This is shown in Figure 71 along with the measured +600 mV sample and the Pt and PtO_2 reference materials. This is in agreement with Friebel *et al.* who also simulated spectra to analyse HERFD XANES measurements and also proposed that Pt_3O_4 was on

the surface.[6] Observing the simulated spectra, all of the peaks are at the same energy as the experimental spectra, although the peak intensities are greater in the simulation.

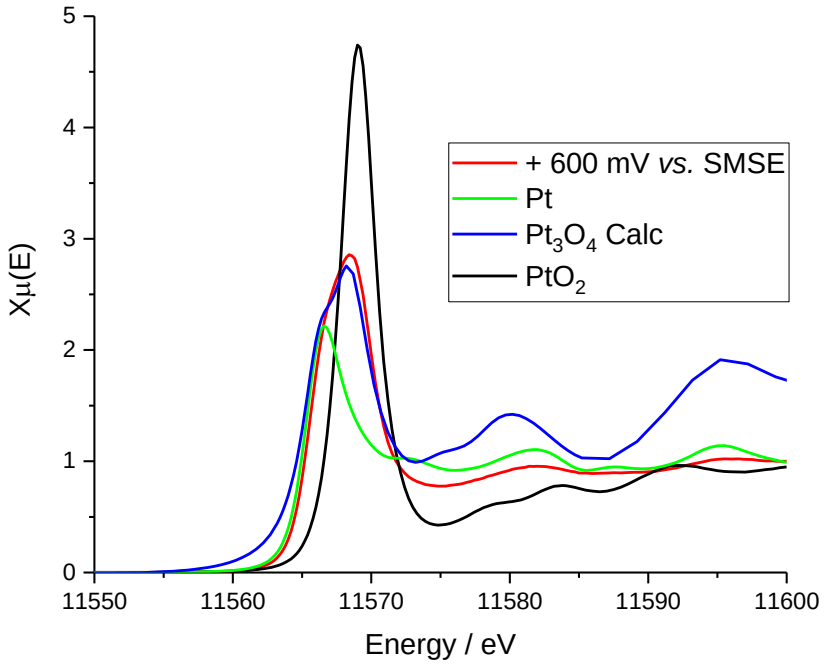

Figure 71. Comparison between Pt foil, PtO_2 and +600 mV *vs.* SMSE Pt nanoparticles and the simulated Pt_3O_4 spectra.

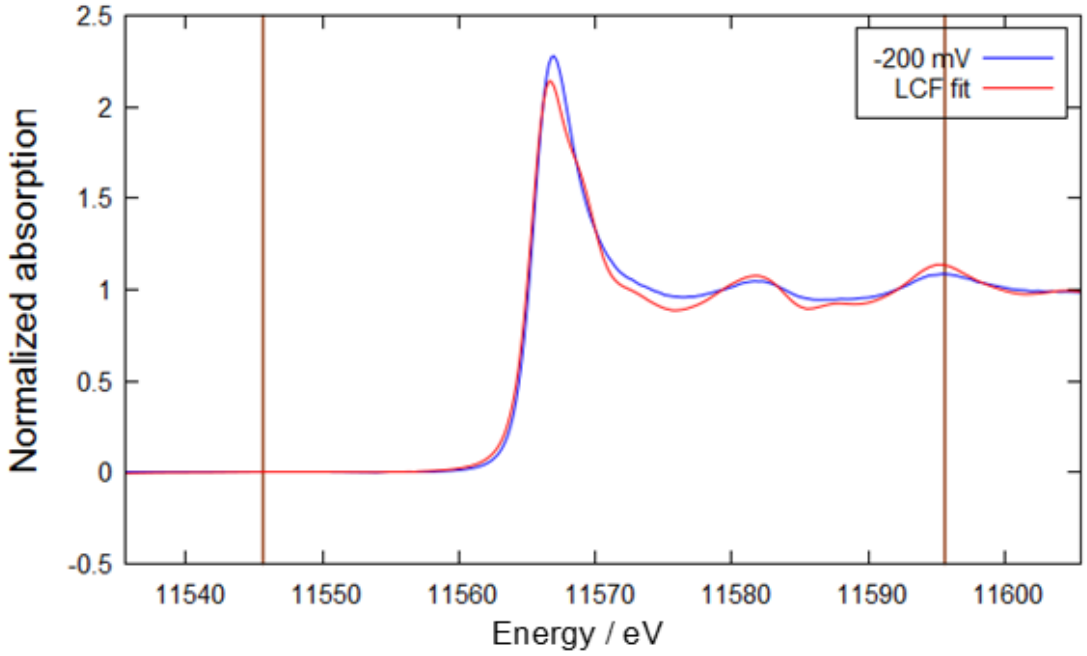

Figure 72. Blue line shows data for Pt/C at -200 mV *vs.* SMSE for data collected at I20. Red line shows the results of the LCF, vertical brown lines show the energy region over which the data have been fit. R-factor is 0.001.

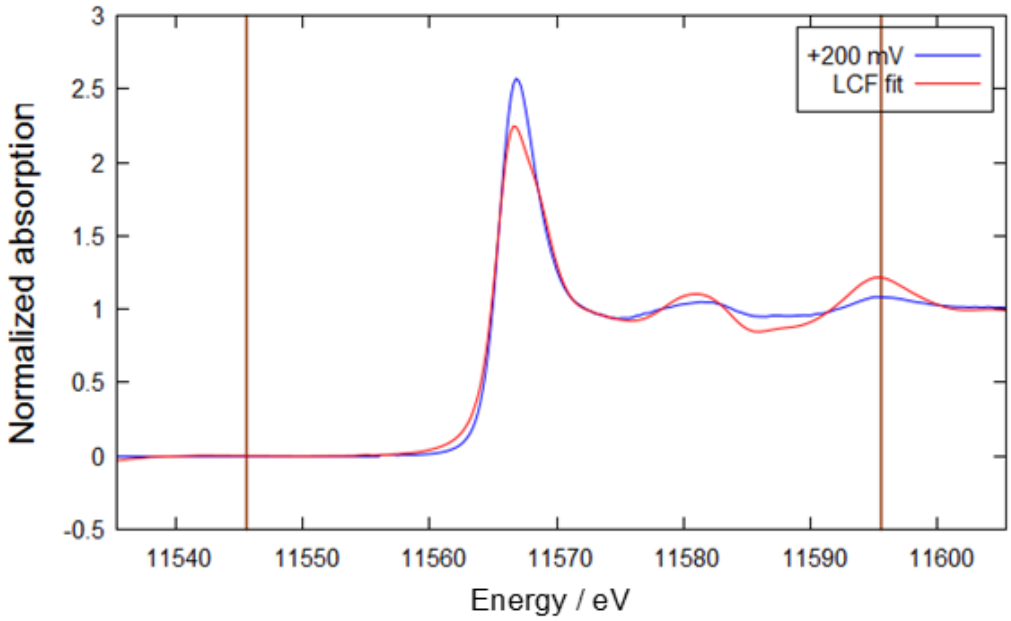

Figure 73. Blue line shows data for Pt/C at +200 mV *vs.* SMSE for data collected at I20. Red line shows the results of the LCF, vertical brown lines show the energy region over which the data have been fit. R-factor is 0.002.

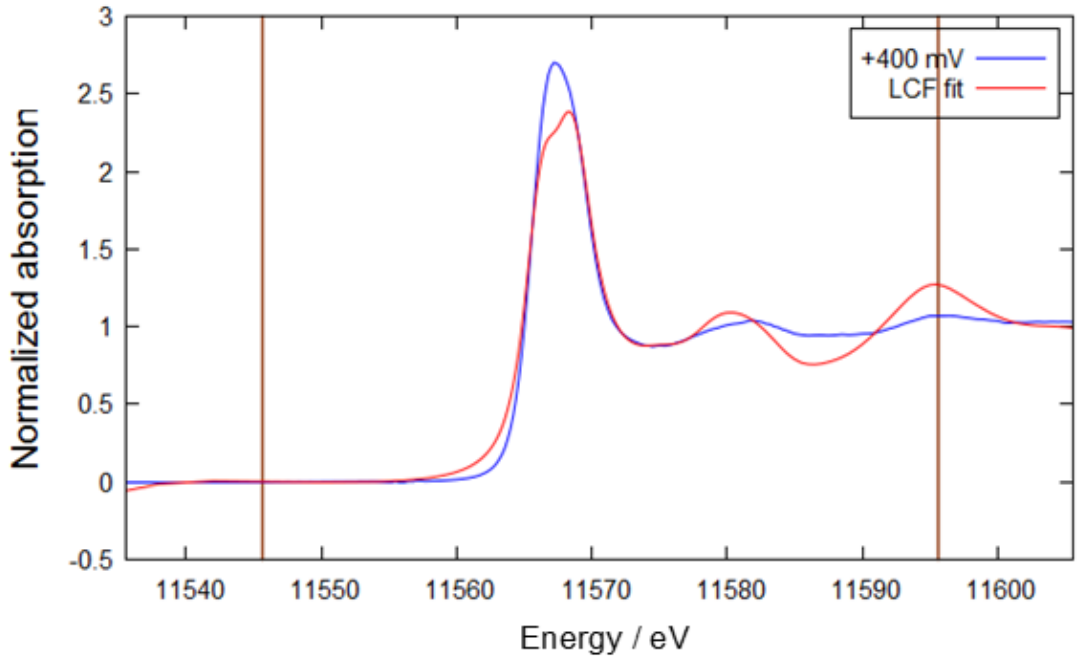

Figure 74. Blue line shows data for Pt/C at +400 mV *vs.* SMSE for data collected at I20. Red line shows the results of the LCF, vertical brown lines show the energy region over which the data have been fit. R-factor is 0.003.

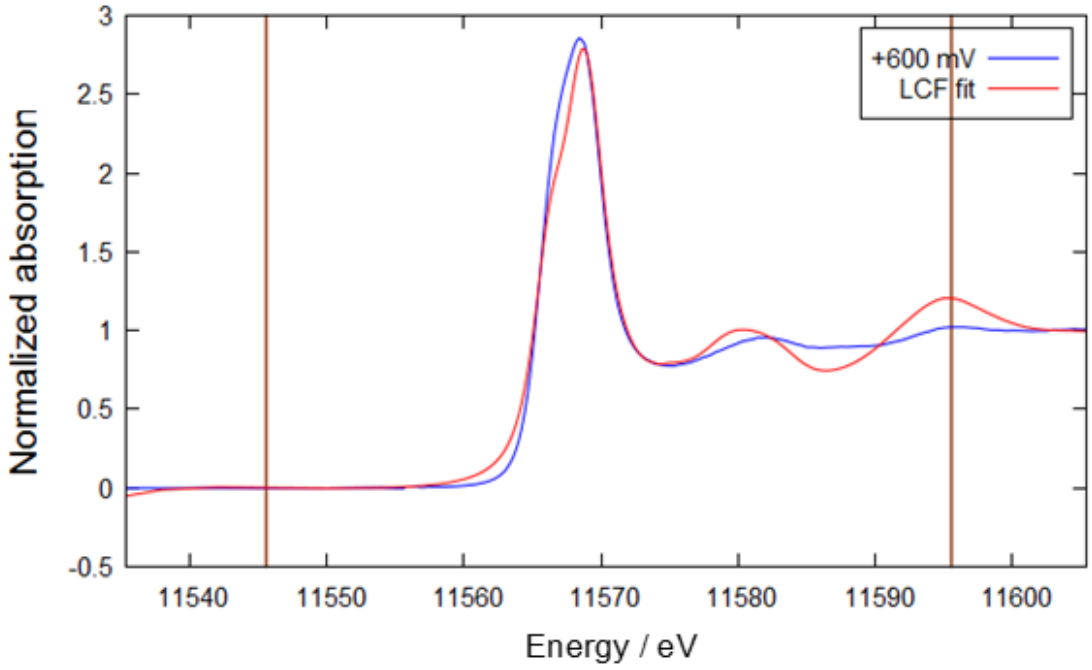

Figure 75. Blue line shows data for Pt/C at +600 mV *vs.* SMSE for data collected at I20. Red line shows the results of the LCF, vertical brown lines show the energy region over which the data have been fit. R-factor is 0.002.

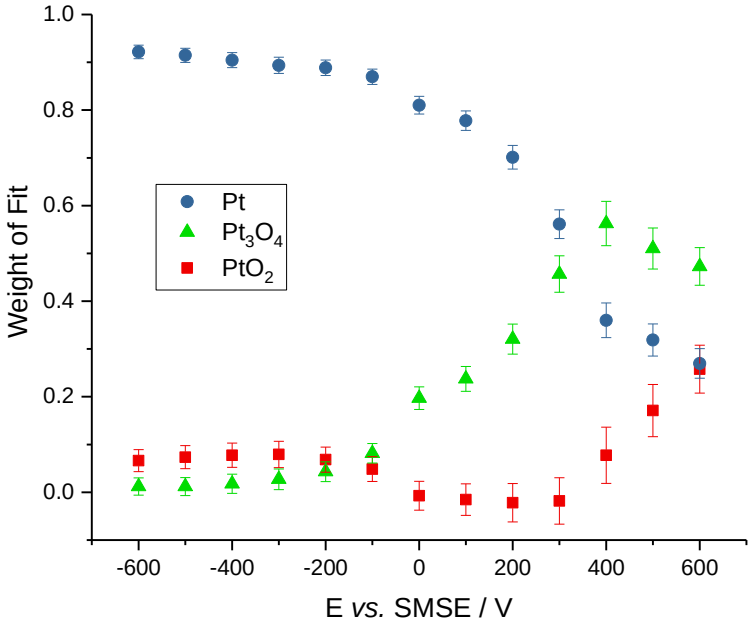

Figure 76. Results of the linear combination fit of the XANES region of the HERFD spectra with Pt foil, PtO_2 and simulated Pt_3O_4 reference files. The R-factors were all less than 0.03.

Three of the spectra Pt foil, PtO_2 and simulated Pt_3O_4 were used as references for a linear combination fitting for the HERFD XANES spectra and the results are presented in Figure 76 (Figure 72 to Figure 75 show four of the linear combination fits compared to the experimental spectra). Similar to the conventional XANES, the more negative potentials are almost entirely Pt metal, as the potential moves more positive the proportion of the fit which is Pt_3O_4 grows from -

100 mV *vs.* SMSE and this reaches a peak at +400 mV *vs.* SMSE before dropping off. The fit uses an increasing amount of PtO_2 from +300 mV *vs.* SMSE. From this fit it could be suggested that this is the point where there is a full layer of PtO_2 on the surface on the nanoparticles, which then begins to grow. This is in contrast to Friebel *et al.* who propose Pt_3O_4 at 1600 mV *vs.* RHE (~900 mV *vs.* SMSE), although their work was on Pt thin films on Rh electrodes so the sample environment is different. This is not to say that other species are not present, just that this data set can be fit within error using these three reference spectra, PtOH (and PtH) are likely to be present inside this electrochemical potential region as has been shown using SERS.[33] Consequently, complimentary methods are required to build a complete understanding of this system.

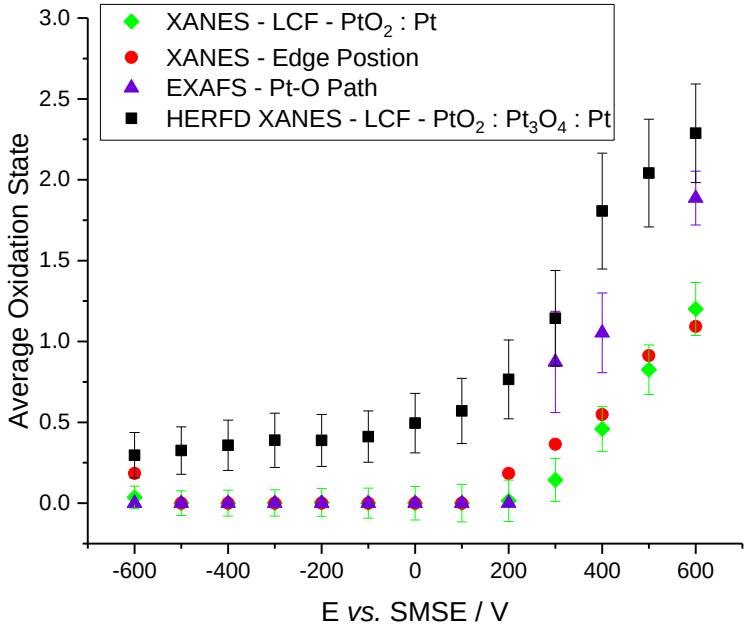

Figure 77. Showing the average oxidation state calculated from the spectra from the edge position method, the LCF method conventional XANES and HERFD XANES and from the EXAFS fitting.

Using a similar method as before, assuming the formal oxidation state of Pt in each of the reference structures is the same in the linear combination fit, the average oxidation state can be calculated for these nanoparticles. Figure 77 shows the results of this calculation with the results of the previous methods. The HERFD XANES shows the highest values for average oxidation state for all of the potentials. This may be a result of including an intermediate oxide so the fit includes oxides reference spectra more readily (due to the intermediate oxide having features more in between the Pt and PtO_2).

4.3.4 XANES Conventional and HERFD – Hydrogen Features

Previous studies have shown that hydrogen on the surface of Pt leads to an increase of intensity 10 eV above the edge. This was shown by Samant and Boudart when using a heterogeneous Pt in

a Y-zeolite catalyst, in the presence of hydrogen gas compared to helium gas this increase in absorption was observed.[23] Since it is expected that at more negative potentials (-600 to -400 mV *vs.* SMSE) hydrogen is chemisorbed to the surface of Pt electrodes the XANES spectra previously presented were analysed to observe this feature.

The Δμ method was used, where relative intensities are compared by subtracting one spectrum from the set of spectra, in this case the reference spectrum was the -100 mV *vs.* SMSE for both the conventional XANES and the HERFD XANES. This potential was chosen as the XAS analysis presented thus far suggests neither PtH or PtO_x are present. Electrochemical data presented in Chapter 3 also supports the hypothesis that the surface of the material has fewest coordinating species at this potential. It should be remembered when analysing this data, that the choice of reference spectrum is vital to any features that are observed, as all features are relative to this spectrum. Ramaker and Koningsberger discussed the use of the $\Delta\mu$ method for observing the effect on platinum XANES, they discussed equation 31.[34]

$$\Delta\mu = \Delta\mu_0 + \Delta[\mu_0\chi_{Pt-Pt}] + \mu_0\chi_{Pt-H}$$

Equation 31

The three terms include changes in the existent atomic x-ray-absorption fine structure ($\Delta\mu_0$), Pt-Pt scattering ($\Delta[\mu_0\chi_{Pt-Pt}]$), and the additional Pt-H scattering ($\mu_0\chi_{Pt-H}$). The results are presented in Figure 78 and Figure 79.

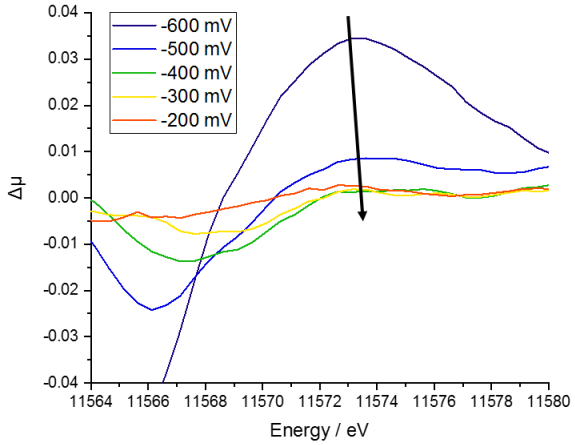

Figure 78. Δμ results for the conventional XANES with the -100 mV *vs*. SMSE used as the reference spectrum. Arrow shows change in spectra intensity 10 eV above the edge as the potential has increased.

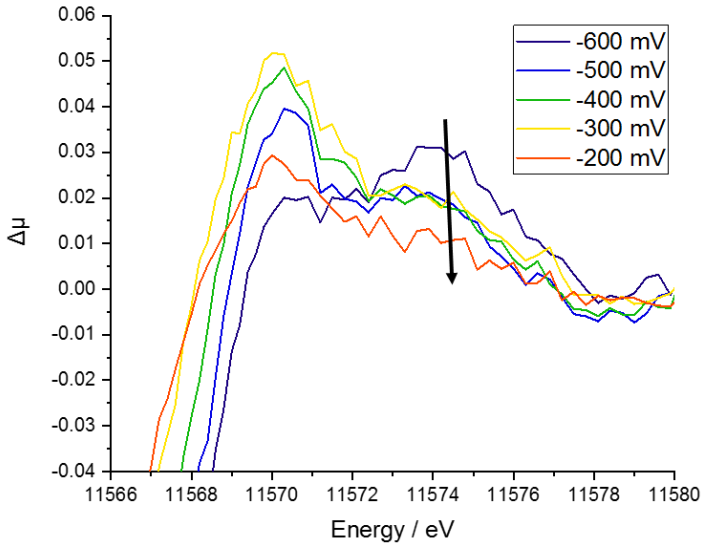

Figure 79. Δμ results for the HERFD XANES with the -100 mV *vs*. SMSE used as the reference spectrum. Arrow shows change in spectra intensity 10 eV above the edge as the potential is increased.

In both cases (Figure 78and Figure 79) there is clearly increased intensity 10 eV above the edge for the -600 mV *vs.* SMSE spectrum. In both cases this intensity drops with increased potential, suggesting that the hydrogen is becoming desorbed, although in the conventional spectra the increased intensity has diminished by - 400 mV *vs.* SMSE. This is in contrast to the HERFD spectra, where the increased intensity remains until the final spectra shown (-200 mV *vs.* SMSE) and by default by -100 mV *vs.* SMSE the increased intensity will be 0. This is very strong spectral evidence that there is chemisorbed hydrogen on the surface of Pt electrodes at reducing potentials, which is similar to chemisorbed hydrogen gas.

4.3.5 Energy Dispersive EXAFS – Time Resolution

So far all of the data presented, has although been *in-situ,* has been using static increments where the electrochemical potential has been held at a fixed value while spectra were collected (for between 30 minutes to 2 hours, depending of the speed of the XAS technique). By using an Energy Dispersive technique the whole XAS spectrum can be collected simultaneously and dynamic experiments can be conducted. This aspect of the project was in part to help commission beamline I20-EDE by running the first electrochemical experiments on the beamline.

With the increased time resolution there are a number of issues, the most important being determining a reliable background to subtract from the recorded data (a typical I_0 is not possible in an EDE set up). As a result an air sample was used as a background (measured by moving the sample stage away from the beam before and after the measurement). There are also issues with beam damage and many of the first attempts were halted when it became apparent that the

measurement was changing the sample. As this measurement was conducted in transmission, a significantly greater amount of sample was required which then affects the electrochemistry and speed of reactions, as these measurements are only valid if the whole sample changes as the same time.

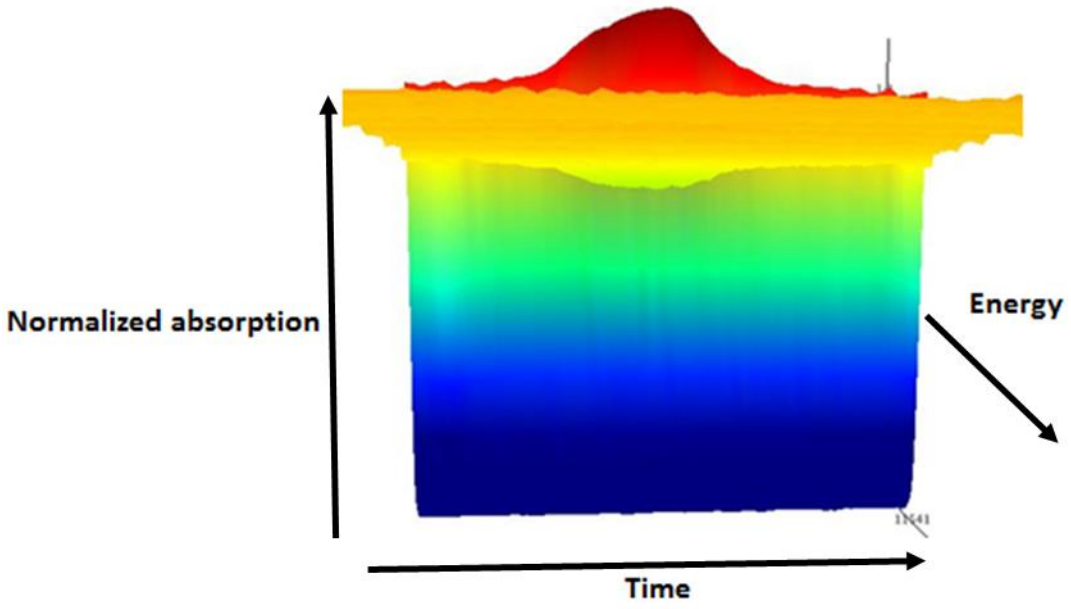

Figure 80. Showing the set of spectra with 5 second acquisition time. Potential at T = 0 is – 650 mV *vs.* SMSE, T = 650 is +400 mV *vs.* SMSE and T = 1300 is – 650 mV *vs.* SMSE, the potential as swept at 2 mV s^{-1}. A shows time on the x-axis, Xm(E) on the y-axis, and photon energy on the z-axis (increasing coming out of the page).

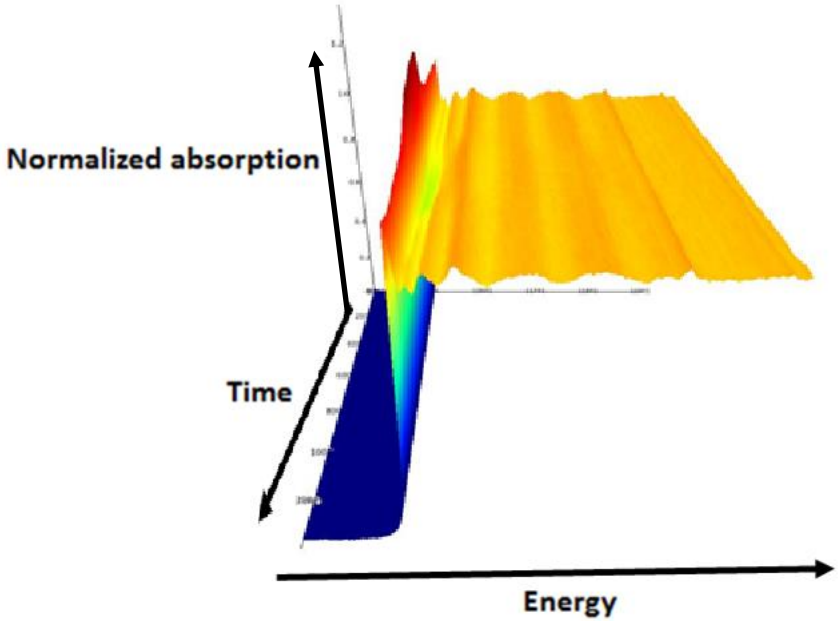

Figure 81. Showing the set of spectra with 5 second acquisition time. Potential at T = 0 is – 650 mV vs. SMSE, T = 650 is +400 mV *vs.* SMSE and T = 1300 is – 650 mV vs. SMSE, the potential as swept at 2 mV s^{-1}. A shows photon energy on the x-axis, Xm(E) on the y-axis, and time on the z-axis (decreasing coming out of the page).

Despite the above caveats promising data were collected using the EDE beamline, Figure 80 and Figure 81 show the spectra as a function of time (while the potential is changed). It is clear that a number of the features described in previous sections, such as the increased intensity of the white line are noticeable in the energy dispersive data. Figure 82 shows how oxide features, such as a growing white line and loss of intensity after the edge can be tracked in 'real-time', with very close agreement to the electrochemical data. Not only are there obvious oxide features that align very well with the electrochemistry, but there are also subtle increases in intensity when the electrode is reduced, suggesting that the chemisorbed hydrogen could be distinguished. These are only preliminary results and further experiments are planned for the near future to build on the work.

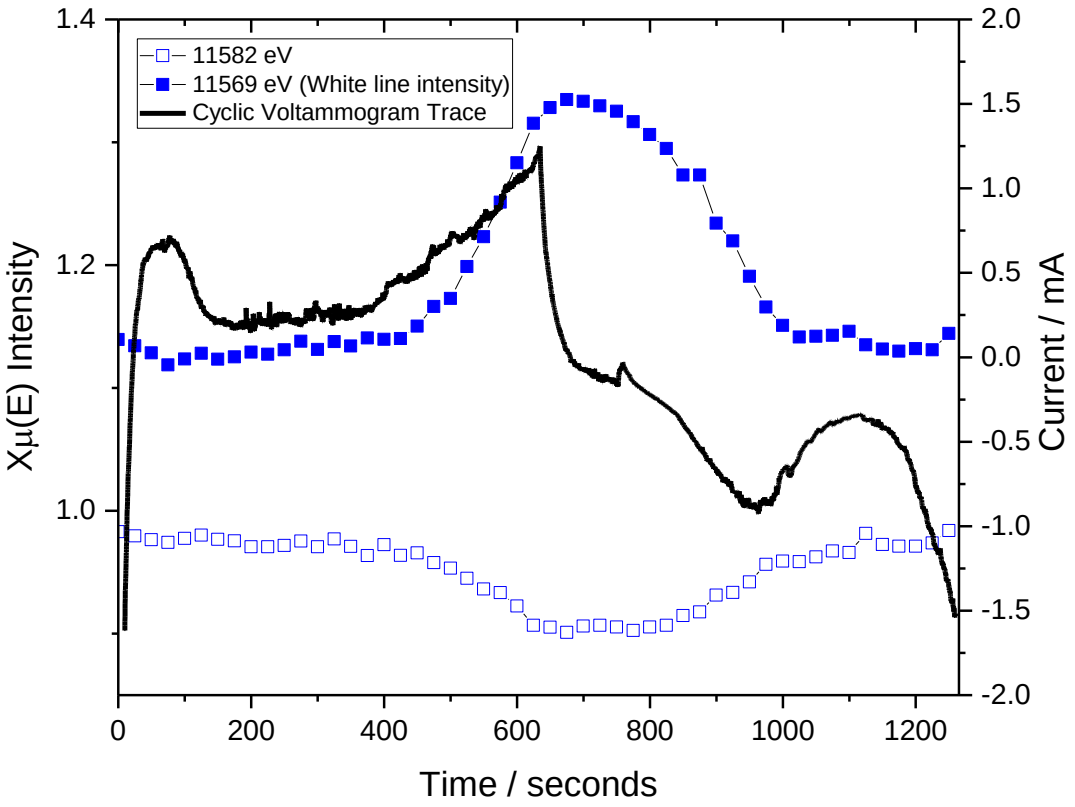

Figure 82. Black line is the current time trace using the right hand axis. Filled in blue squares show the spectra intensity at 11569 (top of the absorption edge). Blue outlined squares show the spectra intensity at 11582 (after the absorption edge). Potential at T = 0 is – 650 mV *vs.* SMSE, T = 650 is +400 mV *vs.* SMSE and T = 1300 is – 650 mV *vs.* SMSE, the potential as swept at 2 mV s^{-1}.

The EXAFS were very hard to analyse as there was only data to 10 $Å^{-1}$ in *k* space, below even the values reported by Mathew *et al.,* which showed significant artificial changes to the spectra.[35] It is clear that on this time scale the EDE measurement is able to align with the electrochemistry. Therefore, more confidence can be had in future *in operando* measurements when gas can be supplied to the electrode, mimicking more realistic electrode working environments. It is for these faster measurements that EDE is essential. When these experiments are repeated there will be an attempt to increase the *k* space range.

4.4 Conclusions

A comprehensive study to investigate the oxidation of platinum nanoparticles using a number of synchrotron-based techniques has been presented. The overall conclusion from the XANES analysis is that the particle is hydrogen covered at reducing potentials (-600 mV *vs.* SMSE to at least -500 mV *vs.* SMSE, but the HERFD spectra's additional energy resolution suggested this could be the case to -300 mV *vs.* SMSE).

Table 5. Presents the different information that can be extracted from the HERFD XANES, conventional XANES, EXAFS and EDE.

	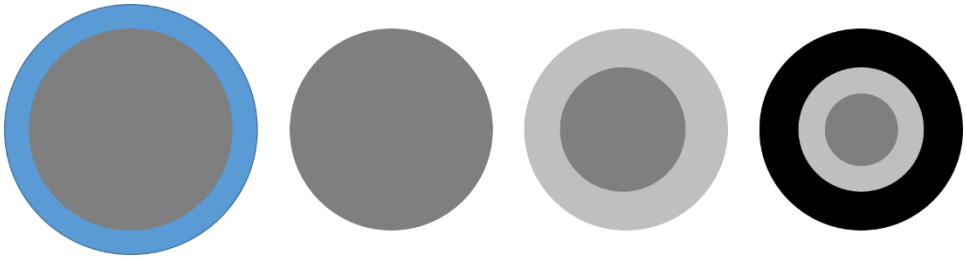			
Method	Pt with H adsorbed	Pt	Pt core with Pt_3O_4 shell	Pt core with Pt_3O_4 interface with PtO_2 shell
Conventional XANES	-600 to -500 mV *vs.* SMSE	- 400 to +200 mV *vs.* SMSE	N/A	+300 to +600 mV *vs.* SMSE (without Pt_3O_4 interface)
HERFD XANES	-600 to -300 mV *vs.* SMSE	- 200 to +0 mV *vs.* SMSE	+0 to +300 mV *vs.* SMSE	+400 to +600 mV *vs.* SMSE
EXAFS	N/A	<+200 mV *vs.* SMSE	N/A	+300 to +600 mV *vs.* SMSE (with interface)
EDE	Possibly observed at most negative potentials <-600 mV *vs.* SMSE	- 600 to +300 mV *vs.* SMSE	N/A	+300 to +600 mV *vs.* SMSE (without Pt_3O_4 interface)

The particle is then partially oxidised from 100 to 200 mV *vs.* SMSE starting with a Pt_3O_4 like structure and finally to a PtO_2 structure, which is first observed using the HERFD XANES at 400 mV *vs.* SMSE, and continues to grow at more positive potentials. The HERFD allowed for these extra structures to be added to the fits, as this information is lost to experimental broadening in the

conventional XANES. The EXAFS data was also fit and gave similar results as the conventional XANES.

Table 5 shows the additonal stages of particle oxidation and reduction, which are propsed using the higher energy resolution spectra, it is clear that the chemisorbed hydrogen can be observed over a larger range of potentials. Also an interface between the Pt metal and the PtO_2 can be resolved.

This additional information from the HERFD combined with the EDE spectra, which offers significantly higher time resolution, both shown in this work, can in future work be comined to assist the understanding of electrode processes under real operating conditions. This will allow the optinisation of sensor electrodes, as the activity of electrocatalysts can be measured *in operando*.

4.5 References

1 E. M. Erickson, M. S. Thorum, R. Vasić, N. S. Marinković, A. I. Frenkel, A. A. Gewirth and R. G. Nuzzo, *J. Am. Chem. Soc.*, 2012, **134**, 197–200.

2 A. E. Russell and A. Rose, *Chem. Rev.*, 2004, **104**, 4613–4636.

3 A. N. Mansour, J. W. Cook and D. E. Sayers, *J. Phys. Chem.*, 1984, **88**, 2330–2334.

4 L. R. Merte, F. Behafarid, D. J. Miller, D. Friebel, S. Cho, F. Mbuga, D. Sokaras, R. Alonso-Mori, T. C. Weng, D. Nordlund, A. Nilsson and B. Roldan Cuenya, *ACS Catal.*, 2012, **2**, 2371–2376.

5 B. Qi, I. Perez, P. H. Ansari, F. Lu and M. Croft, *Phys. Rev. B*, 1987, **36**, 2972–2975.

6 D. Friebel, D. J. Miller, C. P. O'Grady, T. Anniyev, J. Bargar, U. Bergmann, H. Ogasawara, K. T. Wikfeldt, L. G. M. Pettersson and A. Nilsson, *Phys. Chem. Chem. Phys.*, 2011, **13**, 262–266.

7 M. Tromp, J. A. Van Bokhoven, O. V Safonova, F. M. F. De Groot, J. Evans and P. Glatzel, .

8 O. V. Safonova, M. Tromp, J. A. van Bokhoven, F. M. F. de Groot, J. Evans and P. Glatzel, *J. Phys. Chem. B*, 2006, **110**, 16162.

9 A. Gorczyca, V. Moizan, C. Chizallet, O. Proux, W. Del Net, E. Lahera, J.-L. Hazemann, P. Raybaud and Y. Joly, , DOI:10.1002/anie.201403585.

10 H. Asakura, N. Kawamura, M. Mizumaki, K. Nitta, K. Ishii, S. Hosokawa, K. Teramura and T. Tanaka, *J. Anal. At. Spectrom.*, 2018, **33**, 84–89.

11 H.-G. Fritsche and R. E. Benfield, *Zeitschrift für Phys. D Atoms, Mol. Clust.*, 1993, **26**, 15–17.

12 R. E. Benfield, *J. Chem. Soc., Faraday Trans.*, 1992, **88**, 1107–1110.

13 J. M. Montejano-Carrizales, F. Aguilera-Granja and J. L. Morán-López, *Nanostructured Mater.*, 1997, **8**, 269–287.

14 A. Jentys, *Phys. Chem. Chem. Phys.*, 1999, **1**, 4059–4063.

15 D. Glasner and A. I. Frenkel, in *AIP Conference Proceedings*, AIP, 2007, vol. 882, pp. 746–748.

16 A. M. Beale and B. M. Weckhuysen, *Phys. Chem. Chem. Phys.*, 2010, **12**, 5562.

17 R. J. Mathew and A. E. Russell, *Top. Catal.*, 2000, **10**, 231–239.

18 J. Singh, M. Tromp, O. V. Safonova, P. Glatzel and J. A. van Bokhoven, *Catal. Today*, 2009, **145**, 300–306.

19 M. Teliska, V. S. Murthi, S. Mukerjee and D. E. Ramaker, *J. Electrochem. Soc.*, 2005, **152**, A2159.

20 T. M. Arruda, B. Shyam, J. M. Ziegelbauer, S. Mukerjee and D. E. Ramaker, *J. Phys. Chem. C*, 2008, **112**, 18087–18097.

21 N. Ramaswamy and S. Mukerjee, *Adv. Phys. Chem.*, 2012, **2012**, 1–17.

22 L. R. Merte, F. Behafarid, D. J. Miller, D. Friebel, S. Cho, F. Mbuga, D. Sokaras, R. Alonso-Mori, T.-C. Weng, D. Nordlund, A. Nilsson and B. Roldan Cuenya, *ACS Catal.*, 2012, **2**, 2371–2376.

23 M. G. Samant and M. Boudart, *J. Phys. Chem.*, 1991, **95**, 4070–4074.

24 A. J. Dent, G. Cibin, S. Ramos, S. A. Parry, D. Gianolio, A. D. Smith, S. M. Scott, L. Varandas, S. Patel, M. R. Pearson, L. Hudson, N. A. Krumpa, A. S. Marsch and P. E. Robbins, *J. Phys. Conf. Ser.*, 2013, **430**, 12023.

25 B. Ravel and M. Newville, *J. Synchrotron Radiat.*, 2005, **12**, 537–541.

26 D. Inwood, University of Southampton, 2017.

27 S. Calvin, *XAFS for Everyone*, CRC Press, 2014.

28 R. D. Shannon and IUCr, *Acta Crystallogr. Sect. A*, 1976, **32**, 751–767.

29 J. C. Slater, *J. Chem. Phys.*, 1964, **41**, 3199–3204.

30 E. E. Galloni and A. E. Roffo, *J. Chem. Phys.*, 1941, **9**, 875–877.

31 E. A. Owen and E. L. Yates, *London, Edinburgh, Dublin Philos. Mag. J. Sci.*, 1933, **15**, 472–488.

32 S. Siegel, H. R. Hoekstra and B. S. Tani, *J. Inorg. Nucl. Chem.*, 1969, **31**, 3803–3807.

33 Y.-F. Huang, P. J. Kooyman and M. T. M. Koper, *Nat. Commun.*, , DOI:10.1038/ncomms12440.

34 D. E. Ramaker and D. C. Koningsberger, *Phys. Rev. Lett.*, 2002, **89**, 139701.

35 S. Maniguet, R. J. Mathew and A. E. Russell, *Spectrosc. Tools Anal. Electrochem. Syst.*, 2002, **99**, 61–67

Chapter 5: Design of Experiment – Electrode Optimisation and Testing

Electrochemical gas sensors use platinum for electrode materials, which are expensive and scarce. In this work five factors that are believed to have an impact on the quality and performance of gas diffusion electrodes, have been studied using a 'designed experiment', and statistically analysed. If the electrodes can be better fabricated less material may be used, saving money and a precious resource. Another use for platinum is fuel cells for cars, but it was estimated in 2006 by Gordon *et al.* that the world's reserves of the metal would only last 15 years if all cars were made with fuel cells.[1]

5.1 Introduction

The materials used in electrodes are not the only important factors for making an active and durable electrode for use in a gas sensor, although these are the parameters explored most widely in the literature. Structure and morphology of the catalyst particles are also very important. Factors such as particle size and shape and the macro structures formed by agglomerates of particles, have an effect on the long and short term performance of electrodes.[2]

This chapter will investigate the importance of five stages of electrode production, on the structure and performance of electrodes when used in a gas sensor. There are many ways to influence the morphology, including chemically and physically, and here both are investigated. The former, by the use of a dispersing agent as well as varying the amount of the binding material (PTFE) and the latter, by using two different pressures for pressing the electrodes as well as using a different amount of the electrode material. Two different catalysts materials have also been investigated.

5.1.1 Designed Experiments and Split Plots

The main advantage of a 'designed experiment' is that no stone is left unturned. In contrast, if a 'best guess approach' is used, where the experimenter uses experience and knowledge to make a best guess as to which parameter to change next and look for improvements in the measured outputs, the experimenter may find a good combination of the input factors or even the optimum combination, but not for certain.[3] In 'designed experiments' a factor is a parameter that is being changed during the experiment, the different values used for a factor are called levels. An improvement on the 'best guess' approach is the 'one factor at a time' method, where the input

factors are compared one at a time to determine the best value for each, against the measured output values, before moving on to the next factor.[4] Whilst being more systematic, the 'one factor at a time' method ignores the possibility that the factors may have an effect on one another, therefore the optimum combination of input factors may not be determined using this approach. Full factorial experiments test every combination of input factors. Five factors are being tested at two levels (a high and a low value for each). Therefore 2^5 (32) batches of samples will be tested. Not only have all these samples been prepared and tested, they have been done so in a random order. By taking the precaution to ensure the order is random, eliminating the effect of time, and measuring all possible factor combinations, there is the best possible chance of determining the optimum combination of factors. Statistical analysis requires the errors to be randomly distributed, independent variables and by randomising the order in which the samples are prepared we satisfy this assumption.

Preparation of the samples cannot be completely randomised as there are 'hard to change' factors in the experiment. 'Hard to change' factors are defined as those for which it is not feasible (for the amount of time and/or money it would take) to change.[5] For example, changing the ink used to print the electrodes is time consuming and will take time out of a busy production line. Therefore, to save both time and money, the ink is changed as few times as possible. All the factors involved in the ink preparation (catalyst surface area, PTFE content and use of a dispersing agent) are therefore considered hard to change. As a result only eight inks were prepared to make the 32 batches of electrodes, this type of design is known as a spilt plot design.

The inks are known as 'whole plots', the subsequent factors are known as 'sub plots'. The 'whole plots' are completely random as each is independently prepared, but the 'sub plots' are linked because groups of them are made from the same ink (whole plot), and need to be considered when undertaking the statistical analysis.[6] The 'split plot' design can be thought of as two full factorial experiments, the 'whole plot' where the hard to change factors are studied, followed by the collection of 'sub plot' experiments where the 'easy to change' factors are studied.

Figure 83 shows an example 'split plot' design where factor 1 is 'hard to change', therefore this process is only carried out twice (for example, the type of catalyst in an ink, only two inks are made and all the resulting samples are prepared from one of these two inks). Since factors 2 and 3 are not 'hard to change' and batches A and B have the same value for factor 2, they are prepared independently. Even though they could be prepared at the same time, it would increase the chance of systematic error, as any impacts on the one process would affect both batches. The order in which the easy to change factors are applied should also be random.

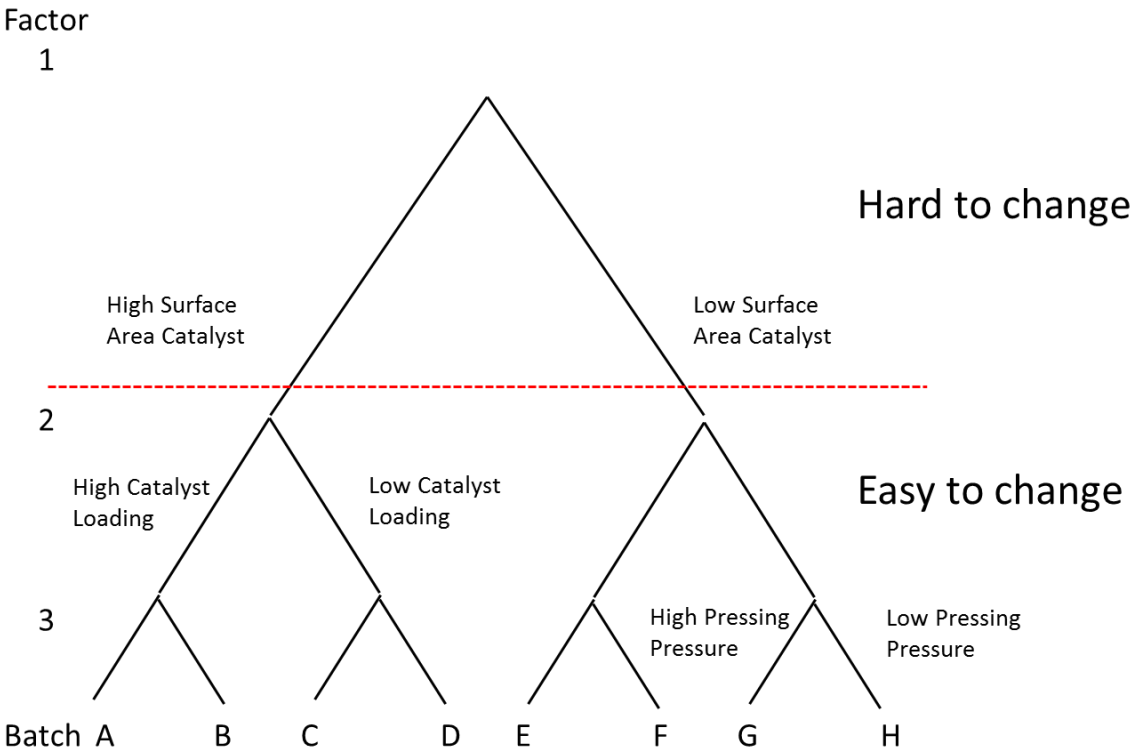

Figure 83. A schematic of a split plot experimental design with 1 hard to change factor, factor 1 the surface area of catalyst, and two easy to change factors; factor 2 the loading of the catalyst, and factor 3 the pressure used to press the electrode.

The main advantages of a 'designed experiment' are; (i) that they test all combinations of factors so interference between factors can be examined and, (ii) that they are time efficient, allowing for the minimum number of experiments to be conducted for the analysis to be meaningful. Although they can be very useful, the assumptions involved in the statistical theory must be understood and followed to ensure the conclusions are valid.

The assumptions used during the analysis are:

- That the samples are randomly prepared. This assumption has not been fulfilled but is accounted for as the analysis is of a 'split plot' design
- The response is normally distributed, in a symmetrical bell shaped curve with a defined mean and standard deviation, because the error is random
- The factors are fixed, meaning they are set at one of two levels and no other value is possible

- The response across the range of factor levels (i.e. for the catalyst between high surface area and low surface area), is approximately linear, this is the hardest to be sure of and should be highlighted along with any conclusions

The results of the analysis will provide a mean and standard deviation for each factor, as well as a description of how each of the factors interact with each other. The mean values and standard deviations will be tested using an F-test to determine if there is any significant variation from the overall mean.

5.1.2 Electrochemical Electrode Characterisation – Cyclic Voltammetry

Cyclic voltammetry is a technique that has been used previously in this work. For this chapter it has been used as a characterisation technique for electrodes, providing a method for measuring the electrochemical surface area (ECSA), achieved by integrating the area under the hydrogen adsorption peaks and calculating the charge, which is proportion to the ECSA. The value used to calculate the ECSA is 210 μC cm^{-2}.[7] It has also been assumed that only 77% of the surface Pt sites have been covered by hydrogen, and has been discussed in depth by Biegler *et al*.[8]

5.1.3 Electrochemical Electrode Characterisation – Electrochemical Impedance Spectrocopy

Impedance spectroscopy is an analytical technique that can reveal many characteristics of an electrode. In particular it investigates the resistive and capacitive components of a whole electrical system. Impedance has a magnitude and a phase; it is the AC vector equivalent to resistance, which is a measure of a DC circuit only and only has a real component. In a DC circuit there is only a potential in one direction, therefore the impedance and resistance are equal. EIS is a technique where a potential perturbation, on the order of 10 mV, is applied to an electrode over a range of frequencies - typically over several orders of magnitude. A sine wave has been used here. The potential applied to the system is described by Equation 32.

$$E_t = E_0 \sin(\omega t) \qquad \textbf{Equation 32}$$

Where E_t is the potential applied to the system at time t, E_0 is the amplitude of the potential at time 0 and ω is the angular frequency described in Equation 33.

$$\omega = 2\pi f \qquad \textbf{Equation 33}$$

Where f is the frequency (Hz). The measured quantity is the resulting current, which can also be represented by a sine wave where the amplitude is I_0, the current observed is described by Equation 34.

$$I_t = I_0 \sin(\omega t + \varphi) \qquad \textbf{Equation 34}$$

Where φ is the amount by which the phase is shifted with respect to the potential (E_t). The phase difference is clearly observed in Figure 84 where the two sine functions are plotted against time. The impedance of a system is a combination of all the resistors, inductors and capacitors considered. In an electrochemical system the double layer charging region at the surface of an electrode is analogous to a capacitor.

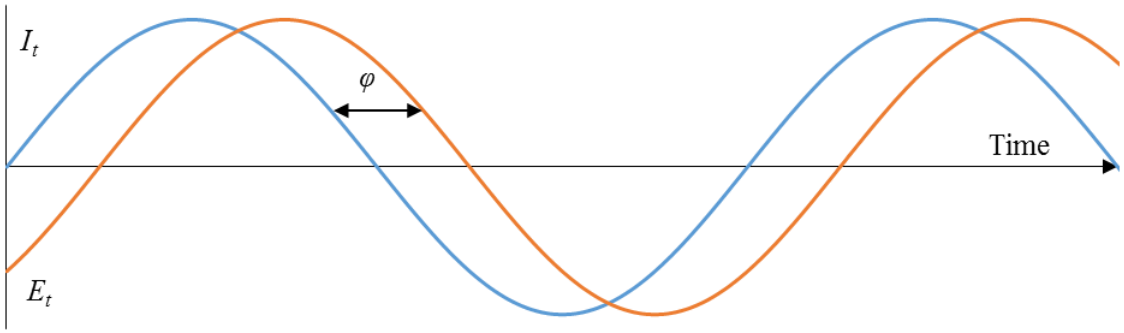

Figure 84. Graph representing the differences between the applied potential and observed current.

Impedance data is often represented in the complex-impedance-plane or Nyquist plot, and is the case here, where $-Z_i$ is plotted against Z_r, and both axes are in units of Ω cm^2.

De Levie suggested a model in 1963 to represent porous electrodes as transmission lines of resistors and capacitors, as shown in Figure 85.[9] The model assumes that the pores are homogenously filled with electrolyte and are uniformly distributed and are cylindrical with a uniform diameter. At short time frames (high frequency) there is a frequency dependence on the penetration depth of the pore as described by Raistrick.[10] Once the frequency is low enough, and penetrates the whole depth of the pore, the response no longer has a real component. This is schematically shown in Figure 85 with the coloured areas of the diagram showing the active parts of the circuit. Figure 86 shows the theoretical Nyquist plot expected from the transmission line model shown in Figure 85. There are two regions in the impedance spectrum, separated by the characteristic frequency. From 1-2 Ω cm^2 on the real (x-) axis where there is a line with a 45° angle, which is the part of the spectrum where the penetration depth is frequency dependant, as the frequency decreases the circuit best describing the electrode shifts from Figure 85a to Figure 85b. There is also a vertical line which is at 2 Ω cm^2 on the real (x-) axis, the region of the spectrum where the frequency is below the characteristic frequency, here the circuit is as shown

in Figure 85b and the electrode is acting without RC in series. If the high frequency range in Figure 86 was extended, the point at which it met the x-axis would be equal to R_u, and the real value of the impedance at and above the characteristic frequency is equal to R_u combined with the resistance along the pore.

Figure 88

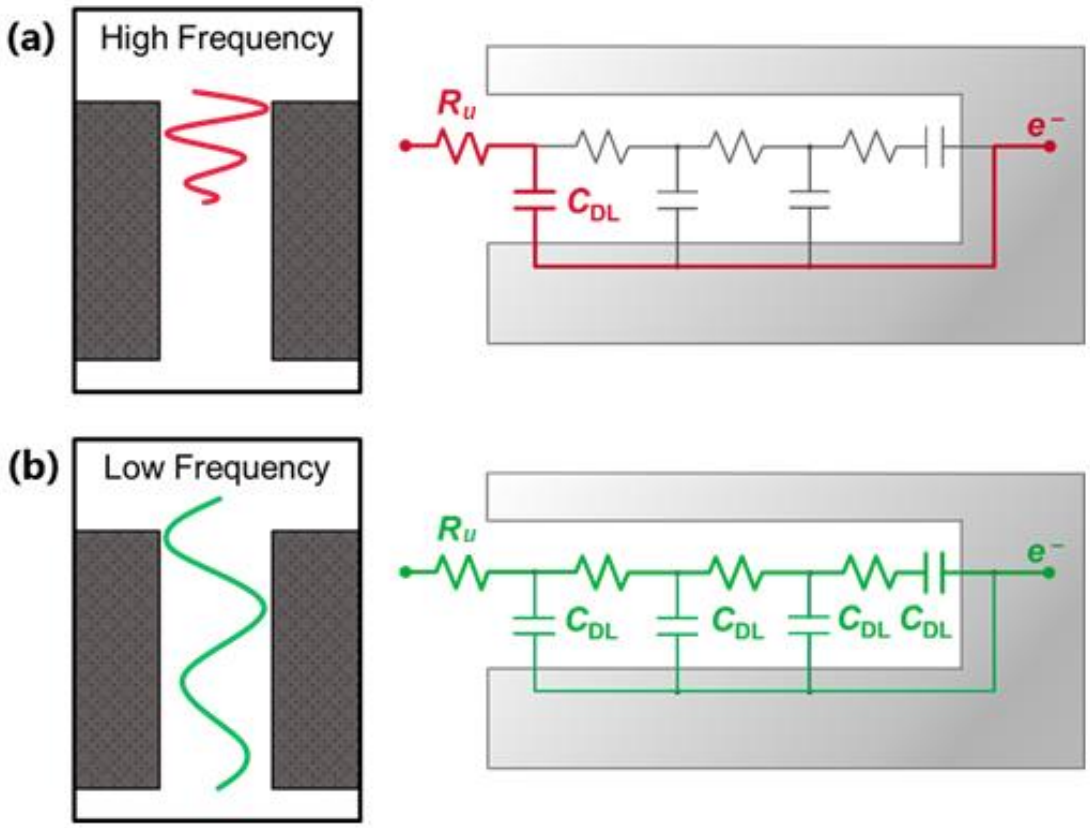

Figure 85 showing the transmission line model for a high and low frequency perturbation. Credit Tammy Nimmo

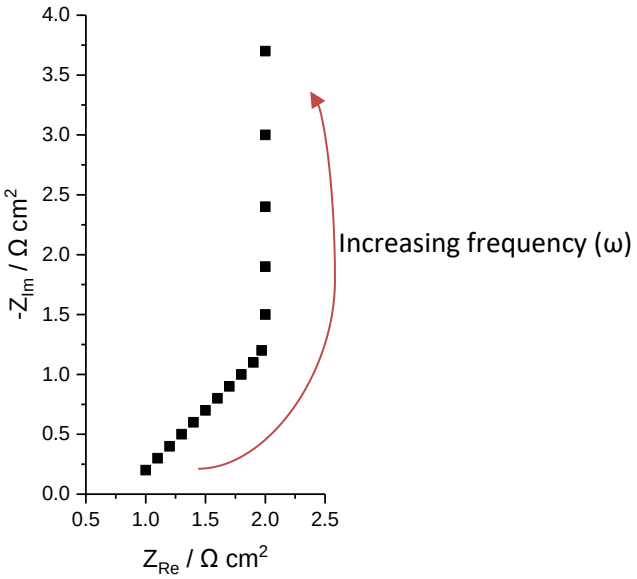

Figure 86. Showing the expected Nyquist plot for a highly porous electrode, recreated from Raistrick[10]

5.2 Experimental

The electrodes have been prepared by Dr Marvin Gayle of City Technology and built and tested under the supervision of Dr John Chapples. The analysis has been conducted in collaboration with Dr John Chapples. Unless otherwise indicated in the test, all other work was carried out by the author.

A range of electrodes have been made changing five different parameters. Each electrode batch has a unique combination of platinum catalyst (HAS or RM32) PTFE content, dispersing agent, loading of material and been pressed by a different pressure. The electrodes have been prepared by John Chapples from City Technology. These parameters have been chosen as it is believed they have a noticeable effect on the performance of the electrodes and sensors. A high and low value for each parameter has been chosen. Table 6 below shows which parameters have been used to prepare each batch of electrodes.

Table 6 shows all the electrode numbers and the parameters used to prepare them. As discussed in the introduction, this order is as random as feasibly possible given that some of the factors are hard to change.

Run Order	PTFE[HTC]	DA[HTC]	Cat[HTC]	Pressing / Kg	Loading / mg
1	12	High	RM29	200	50
2	12	High	RM29	800	50
3	12	High	RM29	200	30
4	12	High	RM29	800	30
5	12	Low	RM29	200	50
6	12	Low	RM29	800	50
7	12	Low	RM29	200	30
8	12	Low	RM29	800	30
9	20	High	RM29	200	50
10	20	High	RM29	800	50
11	20	High	RM29	200	30
12	20	High	RM29	800	30
13	12	High	HSA	200	50
14	12	High	HSA	800	50
15	12	High	HSA	200	30
16	12	High	HSA	800	30
17	20	Low	RM29	200	50

18	20	Low	RM29	800	50
19	20	Low	RM29	200	30
20	20	Low	RM29	800	30
21	20	High	HSA	200	30
22	20	High	HSA	800	30
23	20	High	HSA	200	50
24	20	High	HSA	800	50
25	12	Low	HSA	200	30
26	12	Low	HSA	800	30
27	12	Low	HSA	200	50
28	12	Low	HSA	800	50
29	20	Low	HSA	200	30
30	20	Low	HSA	800	30
31	20	Low	HSA	200	50
32	20	Low	HSA	800	50

Table 1. List of electrodes prepared using the high surface area catalyst

From each batch, 16 electrodes were made into gas sensors and tested *in situ* (as these tested are conducted at the end of the production line it is called End of Line (EoL) data), and some of the electrodes have been tested *ex situ* in a lab environment.

5.2.1 Lab Based Testing

The flooded electrode experiments (as described in chapter 2) conducted at the University of Southampton started with 20 fast conditioning scans at 20 mV s^{-1} to ensure a reproducible voltammogram, followed by two slower scans at 5 mV s^{-1} and finally an AC impedance spectrum was obtained. With this information the electrochemical surface area can be calculated using two different methods. First, using the hydrogen desorption peaks on the voltammogram and integrating the area under these peaks using the conversion factor of 210 µC cm^{-2}. Second Electrochemical Impedance Spectroscopy (EIS) was carried out, the parameters used were; first frequency – 10^4 Hz, last frequency - 0.01 Hz, 5 measurements per decade, amplitude - 10 mV (around -0.2 V *vs* SMSE), wave type – sine.

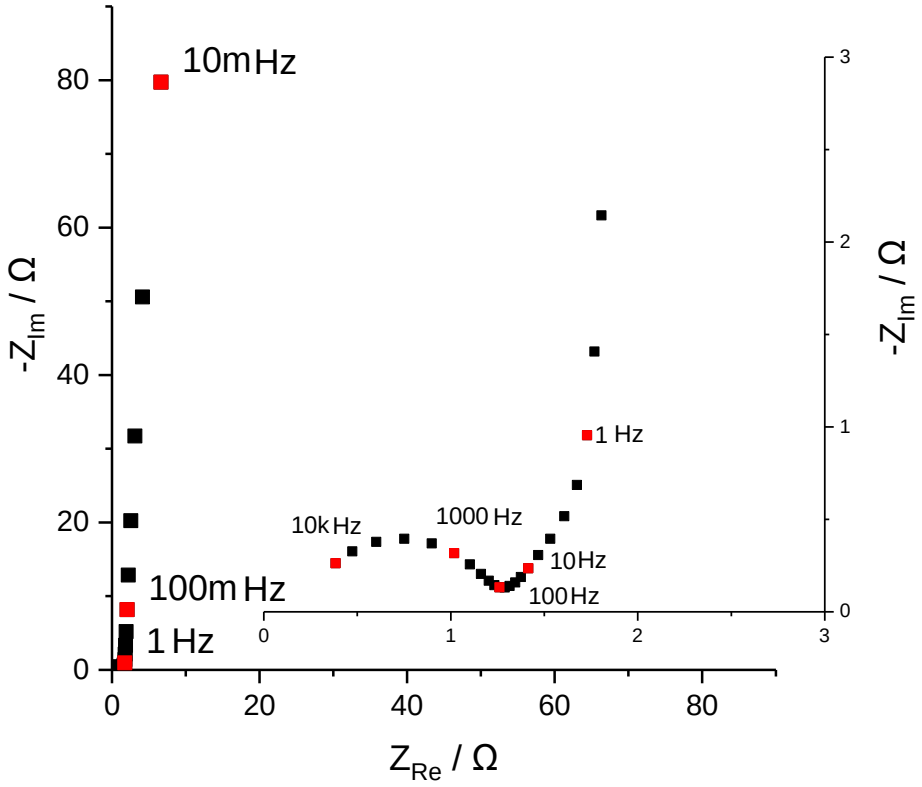

Figure 87. Typical complex plane impedance plot, with zoomed in plot displaying high frequency data inlaid. The frequencies are shown every decade by the red squares. Plot shown is for electrode 3. The measurements were conducted at -0.2 V *vs* SMSE.

Figure 87 shows the complex plane plots for a typical electrode with all the data displayed in the main plot, and a zoomed in plot displaying the low frequency data inlaid. This plot looks similar to the expected plot in Figure 86 when looking at frequencies from 100 Hz and slower. The analysis performed was to plot the low frequency imaginary data vs 1/2π f. The gradient of the graph is then 1/C where C is the capacitance, described by Pletcher in "A First Course in Electrode Processes":[11] This analysis assumes the electrode is acting purely capacitively, which given the results shown in Figure 88, a straight line with an R^2 value of 0.99, seems a reasonable assumption to make.

$$-Z'' = \frac{1}{2\pi f C}$$

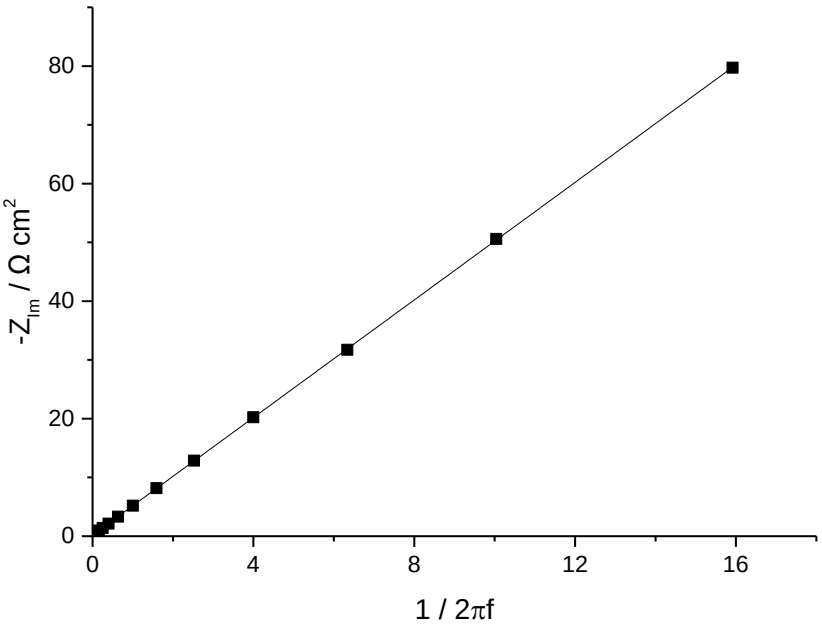

Figure 88. Plot of the imaginary impedance vs 1/2*πf* for the data from Figure 87

From the capacitance the ECSA was calculated with the conversion factor 40 µF cm^{-2}, as had been used by Elliot *et. al*.[12] These values were compared to the hydrogen peaks in Figure 89. Four electrodes of each type were measured from each set, the 95% confidence for each set was calculated using the standard deviation and is shown by the error bars, the trend line is also displayed with a 95% confidence, calculated from only the points for each set. Although there is a small offset the ECSA found using the integration of hydrogen peaks are larger by 7 ± 5 %, but there is an obvious correlation between the two methods. The offset may be; an error in the integration of the hydrogen peaks, which includes a user defined baseline, in the estimated coverage of the Pt surface, in the estimated capacitance of these electrodes, or a combination of the above among other factors not mentioned. The strong correlation revealed in Figure 89 suggests that a relatively quick impedance spectra could be used as well as, or instead of, other electrochemical tests to monitor electrode surface area changes. This test could even be implemented into a "smart" sensor to track electrode degradation. It should be remembered that it is, as conducted in this work, only valid for electrode materials where all the electroactive area is of interest. Materials such as Pt/C where only the Pt is catalytically active but the carbon, which is often in greater amounts, would also give a capacitive response, Reid *et al.* have discussed how these materials could be measured using multiple impedance spectra.[13] To conduct an approximation of the platinum surface area of a carbon supported material impedance spectra are required at potentials where there is a platinum surface process occurring and potentials where there is no platinum surface process.

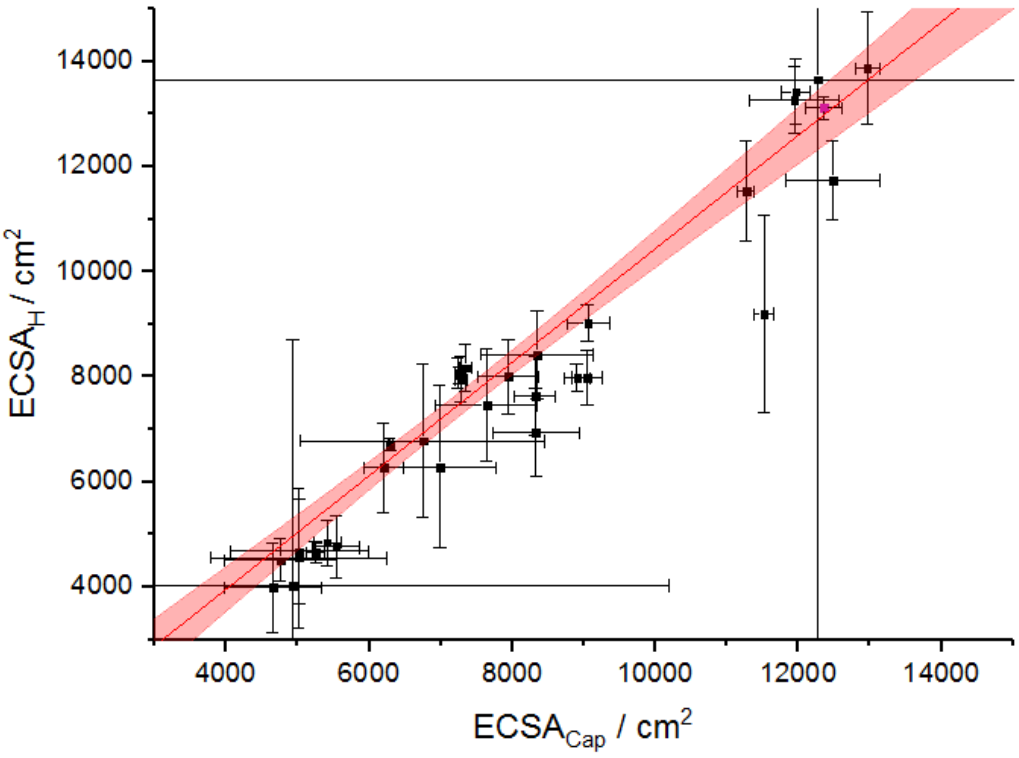

Figure 89. Plot showing the ECSA calculated by two methods for 32 different types of electrode.

SEM images have been taken of all the batches of electrodes. As described in section 2 the electrodes were frozen and cut before being measured. Each electrode type was measured top down viewing the surface area of the electrode, and at 90° viewing the cross section of the electrode.

Electrode 7 **Electrode 21**

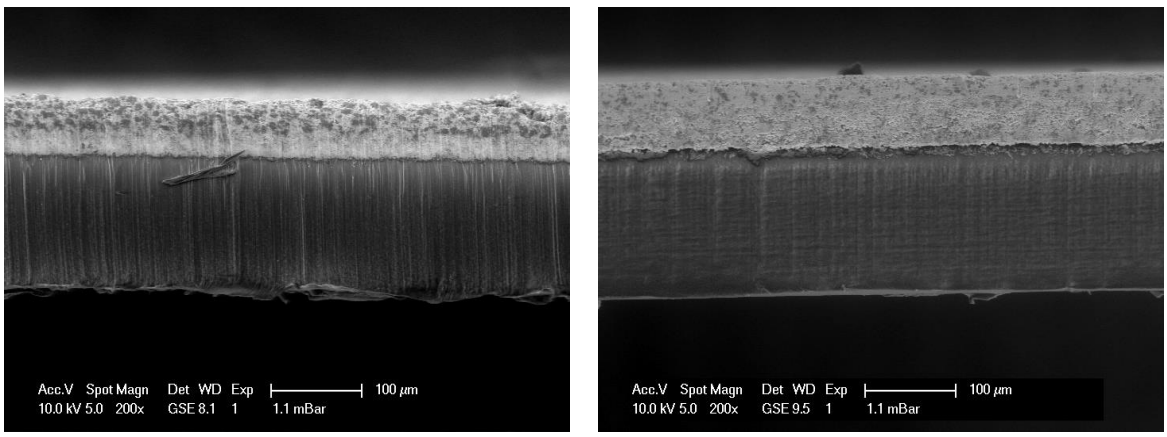

Figure 90. Cross sectional SEM images of two electrodes prepared in the same way except electrode 7 in using the lower surface area catalyst and electrode 21 is using the high surface area catalyst.

Figure 90 shows two typical cross sectional SEM images, these two images show a different pore structure and depth of catalyst layer, despite having the same amount of material. The only difference is the type of Pt catalyst used. On these images the top “rough” layer is the catalyst

layer, these have very different structures as displayed in Figure 90. The depth of the catalyst layer and the PTFE support has been measured for each electrode.

5.2.2 End of Production Line (EoL) Tests

The end of line (EoL) tests consist of; the response time, sensitivity, cross sensitivity to H_2, and recovery time. All of these parameters are very important for the functioning of the sensors. These tests are carried out by first exposing the sensors to an inert gas (synthetic air) for 5 minutes. Then the sensors are exposed to 1000 ppm CO for 3 minutes, followed by 5 minutes of air again and then of 2000 ppm H_2 for 5 minutes. Finally, air is supplied to the sensor for 5 minutes. Figure 91 is a exemplar data set of an expected current-time transient for one of these sensors.

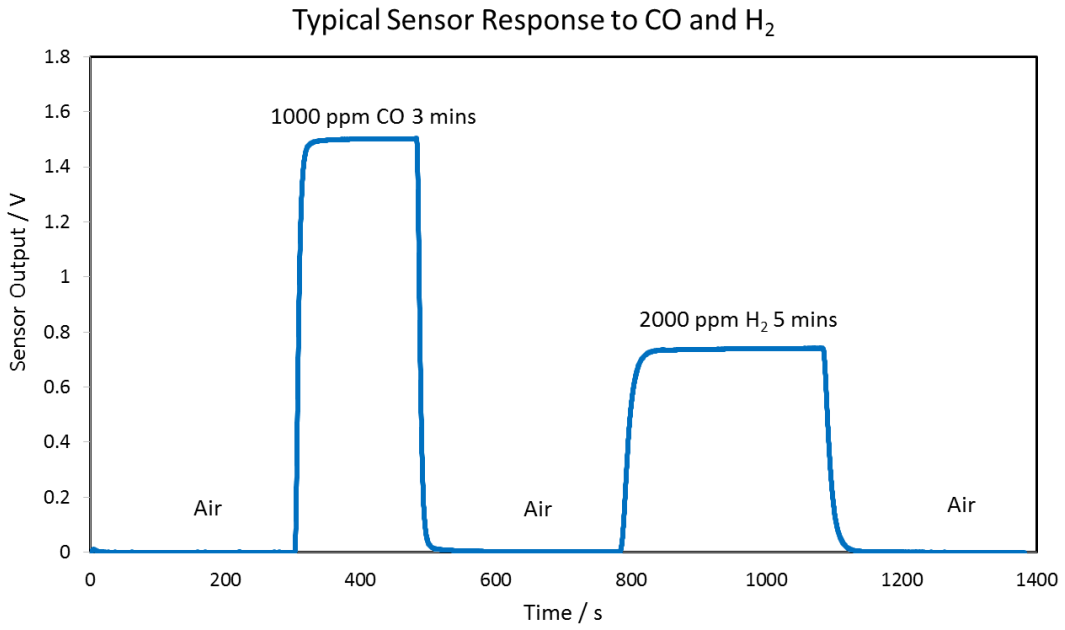

Figure 91. Exemplar data set showing an expected current response from the sensors different electrodes during testing

The response time is the amount of time the sensor took to go from reading 1% of the final stable value to reading 90% of the final stable value. It is expected to be affected by the porosity of the electrode and how quickly gasses diffuse to the three-phase interface.

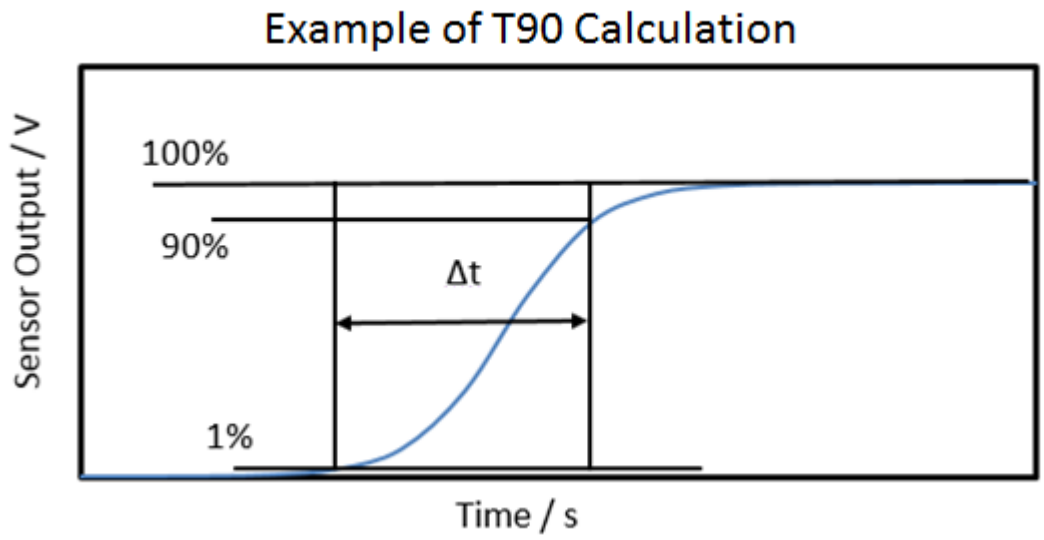

Figure 92. Schematic showing how the response time (T90) is measured (lines are not to scale)

Figure 92 shows graphically how this is done. Recovery time is reverse parameter to response time, and is measured by the time taken for the response to drop from 99% of the stable value to 10% once the gas being sensed is no longer supplied to the electrode. The start point for each of these measurements was chosen as a 1% deviation from the baseline current to allow for systemic error from the pipes and equipment supplying the gas.

5.3 Results and Discussion

A split-plot experimental design was chosen due to having limited time access to the manufacturing line and the cost constraints associated with running platinum inks. The following abbreviations will be used throughout this chapter; the hard to change factors [HTC] were the catalyst type (Cat[HTC]), PTFE content (PTFE[HTC]), and Borchi-Gen® dispersing agent concentration (DA[HTC]),easy-to-change factors [ETC] were electrode pressing pressure (pressing) and catalyst weight (loading).

5.3.1 Response Time (T90)

The response time is the time taken to register 90% of the eventual output. Figure 93 shows the mean and 95% confidence interval for all the electrodes, the low surface area electrodes are the blue circles and the high surface area electrodes are the brown circles (this distinction has been made as it is the clearest differential in the data thus far). On inspection of Figure 93 and Figure 94 (showing the same results for the H_2 test), it is clear to see that the blue dots (low surface area catalyst) have much smaller response times, which is more desirable. They range from between 10 and 16 seconds for the low surface area catalyst compared to between 12 and 22 seconds for the high surface area catalyst. The 95% confidence intervals are also smaller, which shows the results are more reproducible.

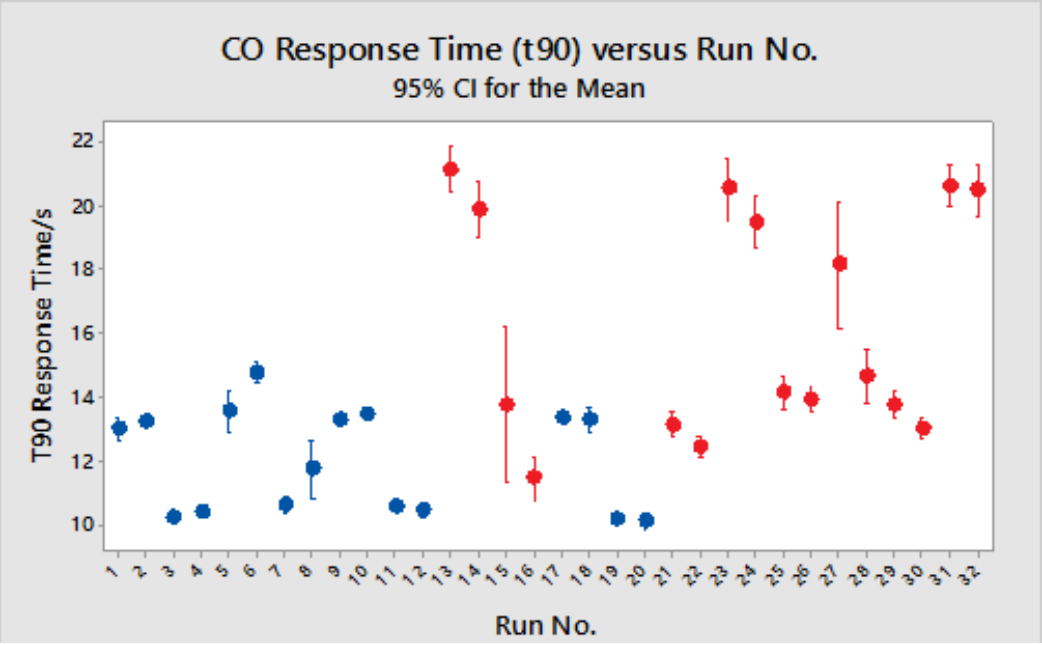

Figure 93. Shows the results of the T90 response time test (CO) for all 32 batches of electrodes with 95% confidence limit individually calculated. Data shown in blue dots are for runs made using low surface area catalyst and those in brown for high surface area catalyst respectively.

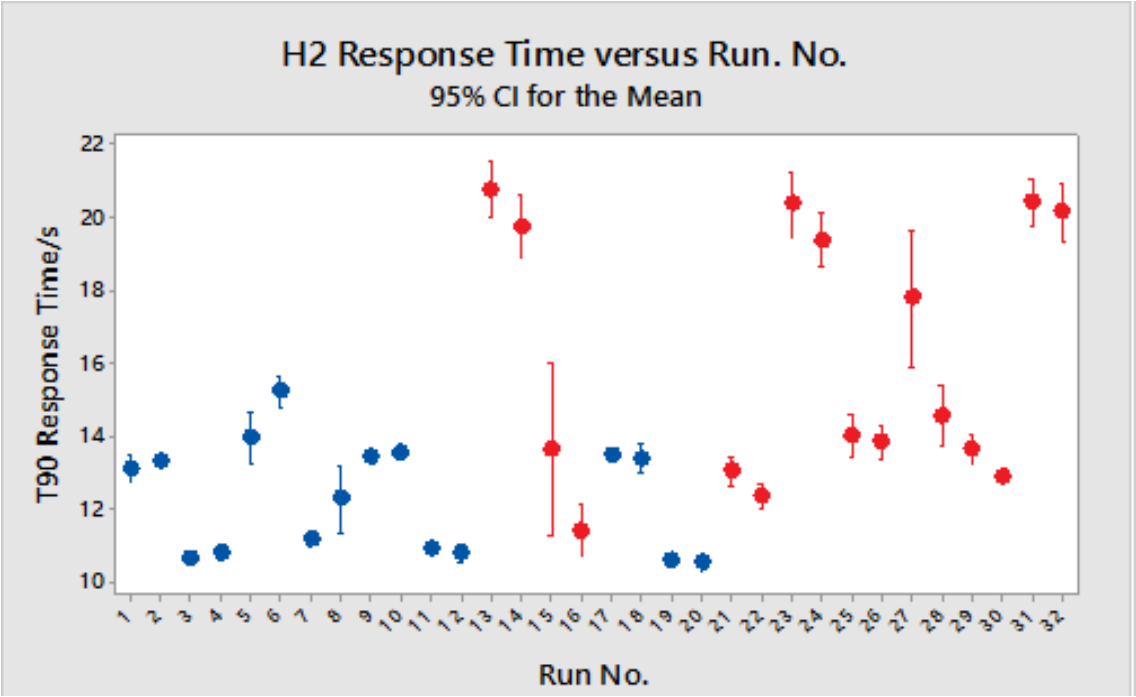

Figure 94. Shows the results of the T90 response time test (H_2) for all 32 batches of electrodes with 95% confidence limit individually calculated. Data shown in blue dots are for runs made using low surface area catalyst and those in brown for high surface area catalyst respectively.

Following the visual overview the data was then analysed in more detail using the split plot design of experiment. The initial (comprehensive) linear model for the split plot design is given below.

Response = PTFE[HTC] + DA[HTC] + Cat[HTC] + PTFE[HTC]*DA[HTC] + PTFE[HTC]*Cat[HTC] + DA[HTC]*Cat[HTC] + PTFE[HTC]*DA[HTC]*Cat[HTC] + WP Error + Pressing + Loading + PTFE[HTC]*Pressing + PTFE[HTC]*Loading + DA[HTC]*Pressing + DA[HTC]*Loading + Cat[HTC]*Pressing + Cat[HTC]*Loading + Pressing*Loading + PTFE[HTC]*DA[HTC]*Pressing + PTFE[HTC]*DA[HTC]*Loading + PTFE[HTC]*Cat[HTC]*Pressing + PTFE[HTC]*Cat[HTC]*Loading + PTFE[HTC]*Pressing*Loading + DA[HTC]*Cat[HTC]*Pressing + DA[HTC]*Cat[HTC]*Loading + DA[HTC]*Pressing*Loading + Cat[HTC]*Pressing*Loading + PTFE[HTC]*DA[HTC]*Cat[HTC]*Pressing + PTFE[HTC]*DA[HTC]*Cat[HTC]*Loading + PTFE[HTC]*DA[HTC]*Pressing*Loading + PTFE[HTC]*Cat[HTC]*Pressing*Loading + DA[HTC]*Cat[HTC]*Pressing*Loading + PTFE[HTC]*DA[HTC]*Cat[HTC]*Pressing*Loading

Terms shown in blue text represent the whole plot (HTC factors), where PTFE[HTC], DA[HTC], and Cat[HTC] correspond to the main factors, PTFE[HTC]*DA[HTC], PTFE[HTC]*Cat[HTC], DA[HTC]*Cat[HTC] and PTFE[HTC]*DA[HTC]*Cat[HTC] are interactions between the main factors and “WP Error” is the whole plot error. Terms shown in red text correspond to subplot, ETC factors “pressing” and “loading” along with their associated interactions. Analysis was simplified by only including terms up to third order in the initial model.

The analysis will confirm which of the terms shown above are statistically significant (to a 95% confidence level) and therefore the majority of the variation should be able to be represented

using a much smaller number of terms. As we are working to confidence level of 95% any parameters with P-values lower than 0.05 will be considered significant.

Table 6. Shows the P-values for the significant parameters for CO T90 response time

Source	P-Value
Cat[HTC]	<0.001
WP Error	0.612
Loading	<0.001
Cat[HTC]*Loading	0.001

The results of the split-plot analysis (shown in Table 6) for T90 response time to CO indicate that the main effects of catalyst type (P<0.001) and loading (P<0.001) are significant at the 0.05% level in addition to the catalyst*loading interaction (P=0.001). All the other parameters (and interactions between parameters) were not significant effects on CO T90. The analysis suggests that the following reduced model is an appropriate fit to the CO T90 response time data.

$$T_{90}\ CO = \text{Catalyst type} + \text{Loading} + \text{Catalyst type*Loading} + \text{error}$$

It can be seen from Table 7 that 96.33% of the variation in the whole plots is accounted for by the single [HTC] factor catalyst and 84.12% of the variation in the subplots is accounted for by the [ETC] factor loading in addition to the interaction term Cat[HTC]*Loading.

Table 7. Summary statistics for the reduced model of the CO T90 response time.

S	R^2(SP)	S(WP)	R^2 (WP)
1.23815	84.12%	*	96.33%

Where S is the standard deviation of the CO T_{90} response time. R-sq(SP) is the proportion of variation among subplots (within whole plots) that is accounted for by the mode. R-sq (WP) is the proportion of variation among whole plots that is accounted for by all of the terms in the model that involve only hard-to-change factors. The suitability of the model was checked through examination of the residual plots as shown below.

Figure 95 is a set of residual plots, from top left clockwise there is the normal probability plot, the residual verses fits, the residual versus observation order, and a frequency versus residual histogram. The residual in each of these cases is the disparity between the experimental observation and the fitted model. In the normal probability plot the data are plotted against a theoretical normal distribution, so that the points should form a straight line. Variation from a straight line suggests the data may not be normally distributed. The residual versus fits is used to ensure there the variation in the data is random and not dependent on the fitted value. Plotting

the residual versus observation order also check the residual is random and not dependent on external experimental factors changing over time. Finally the histogram also checks the data are normally distributed. There will be a number of these figures all with the same plots, in each case the unit of the residual will be the same as the unit of the observation.

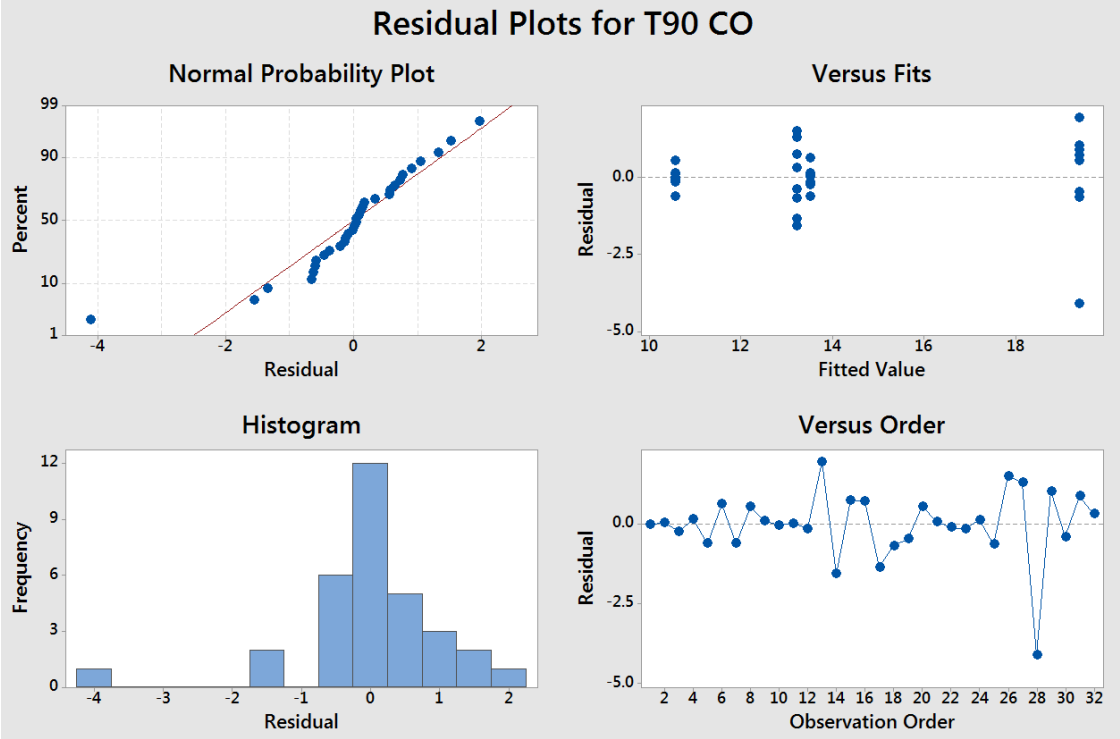

Figure 95. Residual plots for split-plot analysis for CO t90 response time. Units for residual are s.

Overall the model is satisfactory, with the exception of observation 28, which has a large residual of -3.83 standard deviations. Observation 28 corresponds to a run where problems with ink coagulation were noted. It is possible that this caused underweight electrodes to be deposited.

The T90 response time data for H_2 was analysed in the same way with the results shown in Table 8, where the same parameters and interactions are the significant terms. All three having p-values much lower than the 0.05 limit. It is not surprising that both gasses have the same factors effecting the response time as the same physical and electrochemical processes should be occurring in both cases (diffusion, dissolution and the adsorption). The analysis suggests that the following reduced model is an appropriate fit to the CO T90 response time data.

$$T_{90}\ CO = Catalyst\ type + Loading + Catalyst\ type*Loading + error$$

Table 8. Shows the P-values for the significant parameters for H_2 T90 response time.

Source	P-Value
Cat[HTC]	<0.001

WP Error	0.453
Loading	<0.001
Cat[HTC]*Loading	0.001

Table 9. Summary statistics for the reduced model of the H_2 T90 response time.

S	R^2(SP)	S(WP)	R^2 (WP)
5.77904	73.42%	3.46602	93.62%

Again it can be seen from Table 9 that 93.62% of the variation in the whole plots is accounted for by the single [HTC] factor catalyst and 73.42% of the variation in the subplots is accounted for by the [ETC] factor loading in addition to the interaction term Cat[HTC]*Loading.

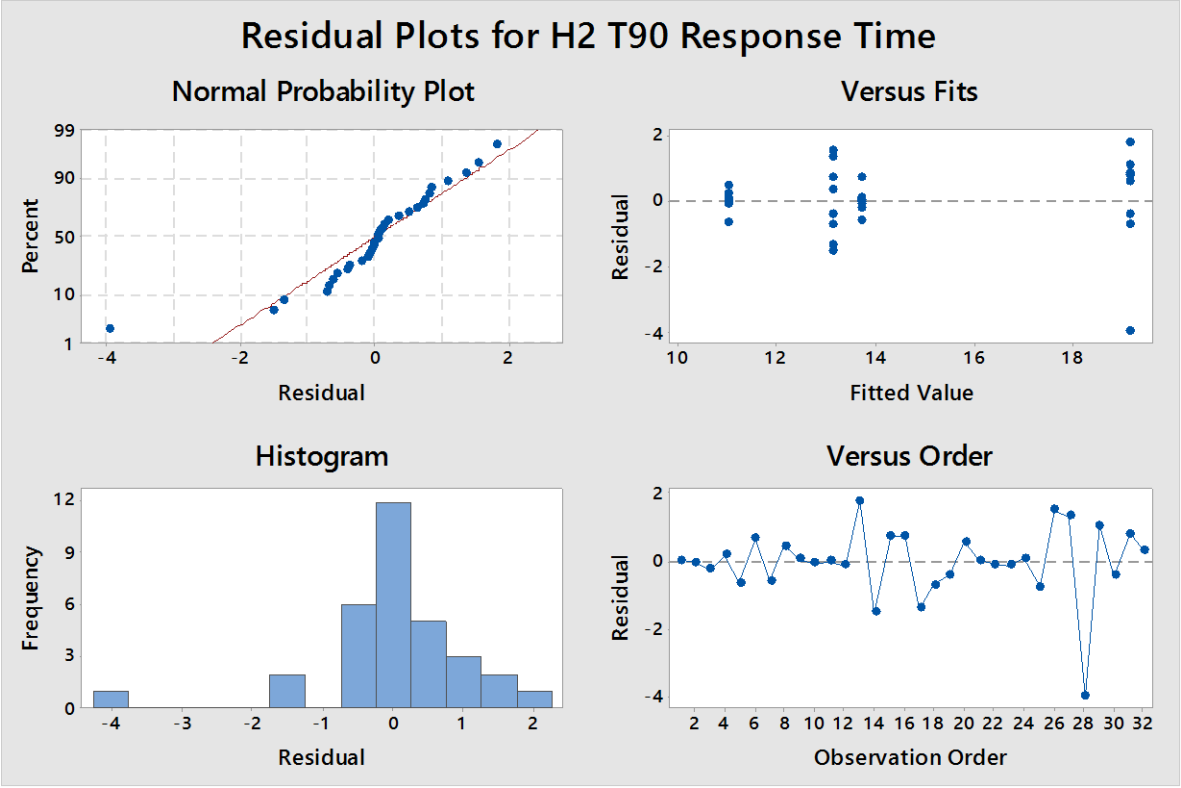

Figure 96. Residual plots for split-plot analysis for H_2 T90 response time. Units for residual are s.

Observation 28 corresponds to the same anomaly as in the T90 CO test, as previously stated these electrodes were noted as having a coagulated ink.

The analysis has yielded very similar results for both CO and H_2 response times. The model indicates the controlling factor in response time for both gases in the cell is the catalyst amount and loading. Suggesting electrochemical factors are more important than cell geometry controlling gas diffusion. This result is consistent with the fact that electrode capacitance might be expected to physically correlate with surface area of the catalyst and loading.

5.3.2 Sensitivity

Following the response time test the same analysis was conducted for the sensitivity of the electrode. Figure 97 and Figure 98 show the sensitivity (nA per ppm) for both gasses (CO and H_2), and the first point to be noted is the y-axis for both graphs: for Figure 97 it ranges between 68 and 80 (nA per ppm), and for Figure 98 it ranges between 10 and 90 (nA per ppm). There is significantly more deviation in the sensitivity to H_2 than there is to CO. This result is not completely unexpected, as the design of the sensor is such that the response should be controlled by capillary limited diffusion to the electrode, and H_2 is much faster at diffusing than CO.[14] More detailed observation of Figure 97 reveals that there is much greater variation in sensitivity of CO for the low surface area electrodes than there is for the high surface area electrodes. This is in contrast to what is shown in Figure 98 where the opposite is true and the high surface area catalyst shows significantly greater variation and on average much larger values. The ideal response would be a high sensitivity to CO and a Low sensitivity to H_2.

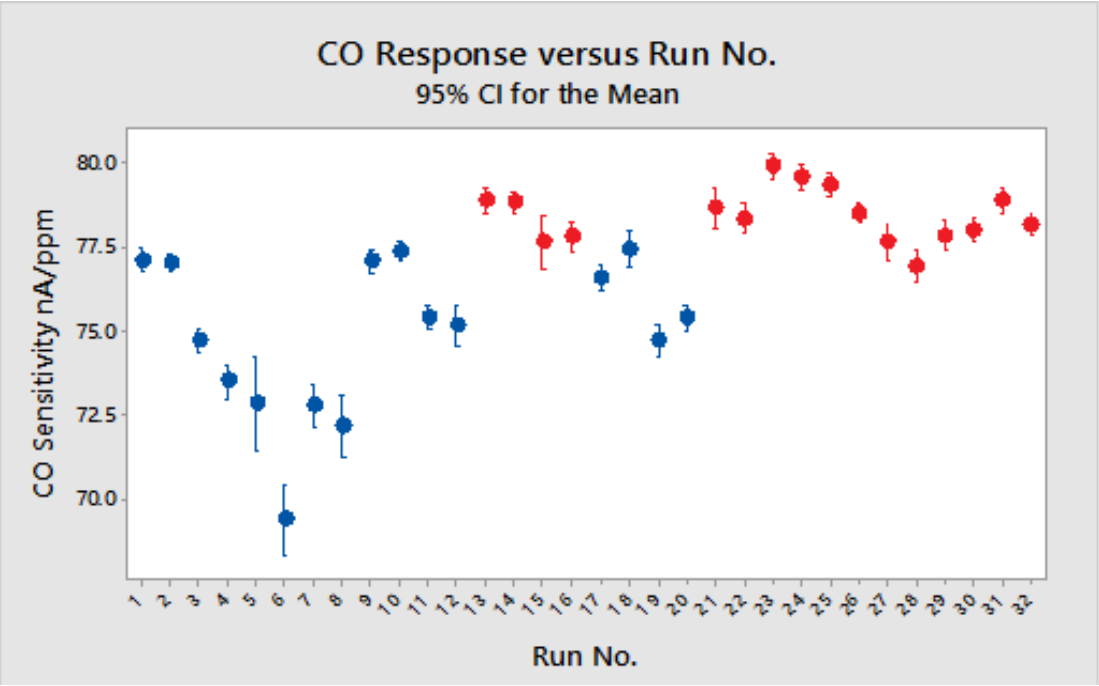

Figure 97 shows the sensitivity for all 32 electrodes to CO with 95% confidence limit individually calculated. Data shown in blue dots are for runs made using low surface area catalyst and those in brown for high surface area catalyst respectively.

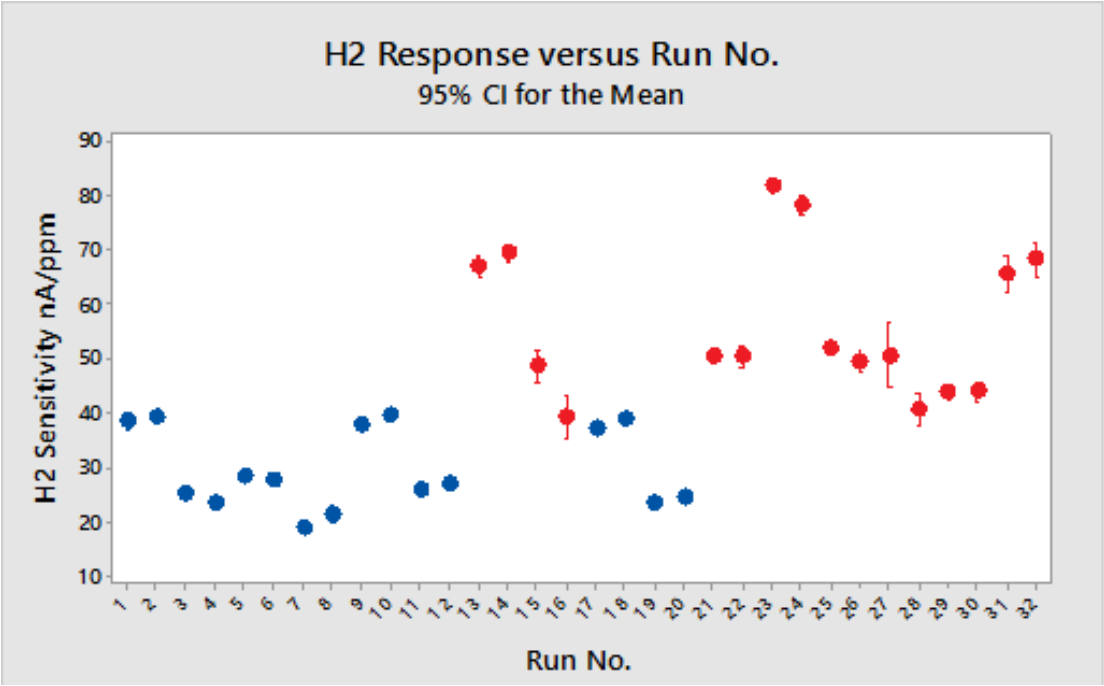

Figure 98 shows the sensitivity for all 32 electrodes to H_2 with 95% confidence limit individually calculated. Data shown in blue dots are for runs made using low surface area catalyst and those in brown for high surface area catalyst respectively.

Table 10. Shows the P-values for the significant parameters for CO sensitivity.

Source	P-Value
DA[HTC]	0.272
Cat[HTC]	0.019
WP Error	<0.001
Loading	0.017
DA[HTC]*Loading	0.009

The results of the split-plot analysis for CO output sensitivity indicate that the main effects of dispersing agent (P=0.272), catalyst type (P=0.019) and loading (P=0.017) are significant at the 0.05% level in addition to the DA*loading interaction (P=0.009). Even though the dispersing agent P-vaule is greater than 0.05 it has been included as the interaction term cannot be included without both main effect, since the interaction with loading term is significant the main effect has been included in the model.

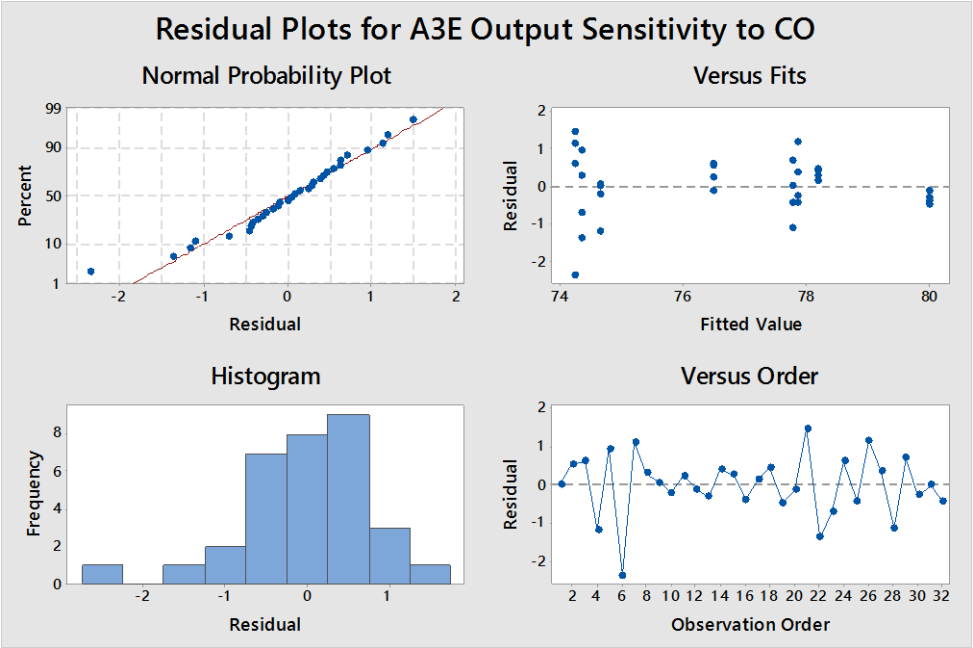

Figure 99. Residual plots for split-plot analysis for gas sensor output sensitivity to CO. Units for residual are nA/ppm.

The residuals follow an approximately normal distribution with the exception of point 6, which has a large standardised residual of -3.03 standard deviations. Residual standard deviations versus fits, show larger residuals for batches of ink that contain no dispersing agent. Overall the model fit is not particularly good in terms of explaining the sensors sensitivity to CO. This can be seen for the model summary data in Table 11, which shows 72.38% of the variation in the whole plots is accounted for by catalyst type and 40.6% of the variation in the subplots is accounted for by the [ETC] factor loading in addition to the interaction term DA[HTC]*Loading. The best fit to the CO output sensitivity data that could be achieved using the information available is shown below.

$$\text{CO output sensitivity} = \text{DA[HTC]} + \text{Cat[HTC]} + \text{Loading} + \text{DA[HTC]*Loading} + \text{error}$$

Table 11. Summary statistics for the model of gas sensor output sensitivity to CO.

S	R^2(SP)	S(WP)	R^2 (WP)
0.940748	40.60%	1.38406	72.38%

Finally the analysis was conducted on the H_2 sensitivity results. Table 12 shows the P-values for the significant terms in the model.

Table 12. Shows the P-values for the significant parameters for H_2 sensitivity.

Source	P-Value
PTFE[HTC]	0.033
DA[HTC]	0.024
Cat[HTC]	<0.001
WP Error	0.397

Loading	<0.001
PTFE[HTC]*Loading	0.02
DA[HTC]*Loading	0.011

The results of the split-plot analysis for H_2 output sensitivity indicate that the main effects of catalyst type (P<0.001), loading (P<0.001), dispersing agent (P=0.024) and PTFE (P=0.033) are significant at the 0.05% level in addition to the DA*loading interaction (P=0.011) and PTFE*loading interaction.

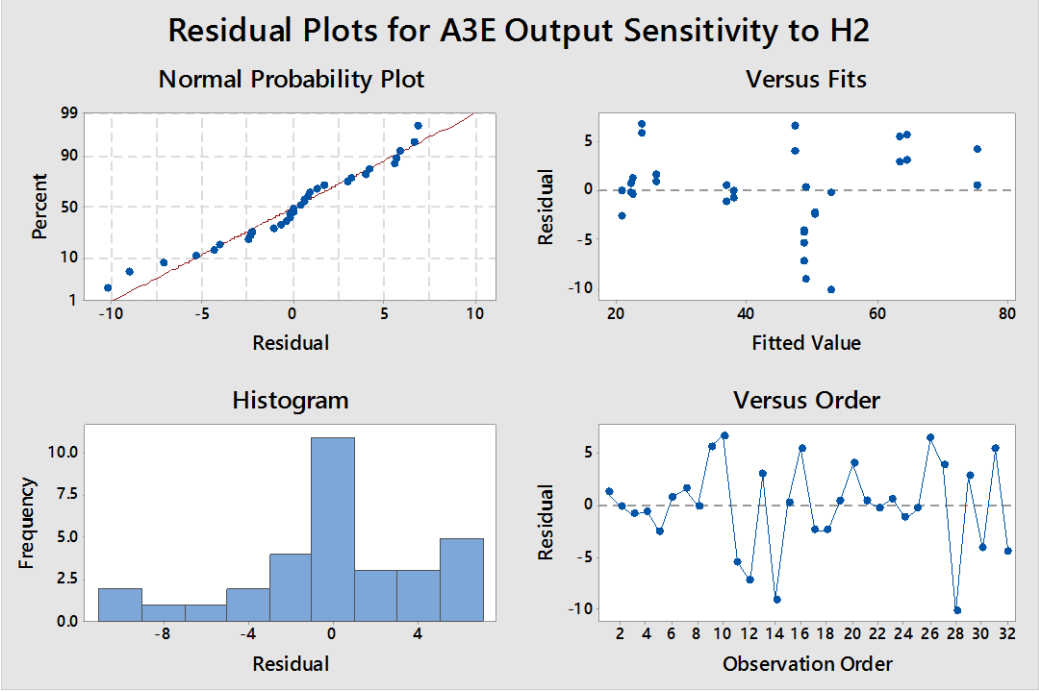

Figure 23. Residual plots for split-plot analysis for A3E output sensitivity to H_2. Units for residual are nA/ppm.

The residuals follow an approximately normal distribution with the exception of points 14 and 28 which have residuals of -9.6 and -10.0 (-2.16 and -2.43 standard deviations respectively). The standardised fit versus residual fit shows quite a large spread in standard deviations. Overall the summary statistics for the model fit (refer to Table 13) shows that 98.2% of the variation in the whole plots is accounted for by the [HTC] factors catalyst type, PTFE and DA and 79.55% of the variation in the subplots is accounted for by the [ETC] factor Loading in addition to the interaction terms DA[HTC]*Loading and PTFE*Loading. The analysis suggests the following model as the most appropriate fit to the data.

H2 Output sensitivity = PTFE[HTC] + DA[HTC] + Cat[HTC] + Loading
+ PTFE[HTC]*Loading DA[HTC]*Loading + error

Table 13. Summary statistics for the model of gas sensor output sensitivity to H_2.

S	R^2(SP)	S(WP)	R^2 (WP)
5.18846	79.55%	0.676133	98.20%

Overall the goodness of fit statistics for the models as summarised in Table 11 and Table 13 are better at explaining the variation in H_2 output sensitivity compared to CO. The effects of all model factors on CO output are small, affecting the output by only a few percent and not practically significant. The most likely explanation is that output response to CO is controlled primarily by diffusion of CO through the gas inlet capillary hole, a factor not included in the experiment. In contrast there is a near doubling in response to H_2 when the catalyst type is changed between RM29 and HSA. The result suggests that any diffusion restrictions imposed by the capillary are much smaller for H_2 and the response is more strongly affected by electrode related factors, gas solubility will also be greater for H_2 compared to CO. This may explain why additional factors and interactions are statistically important for H_2 compared to CO. Although it might be expected that the output response for H_2 may be dependent on catalyst type/surface area and loading the terms relating to PTFE and DA in the model possibly suggests that electrode structure is also important, but to a lesser extent. There are noticeable interactions and the most significant being for electrodes with the highest loading (50mg).

The analysis suggests that with further optimisation it may be possible to reduce H_2 response for HSA catalyst though optimisation of loading without overly compromising the response to CO. Optimisation of the electrode formulation might also be worth consideration since PTFE and Borchi-gen dispersing agent were also significant factors, with the lowest H_2 response obtained with these at the low setting. However, this result is more likely to be due to the ink formulation not being optimised for HSA material and the results are simply due to less than optimal utilisation of the catalyst in the electrode, due to insufficient ink stabilisation resulting in the observed ink coagulation.

5.3.3 Surface Area

The electrodes were also all tested in the laboratory environment, where the electrode electrochemically active surface area (ECSA) was calculated by two methods and cross sectional SEM images were also recorded. The two methods used to calculate the ECSA are measuring impedance spectra by determining the capacitance and then converting to an area, and measuring the charge passed during the hydrogen desorption peaks and converting to an area. Both methods are explained in the experimental section of this chapter.

The results of the split-plot analysis for electrode capacitance indicate the main effects of catalyst type (P<0.001) and loading (P<0.001) are significant at the 0.05% level in addition to the Catalyst*Loading interaction (P=0.024), shown in Table 14. Although the interaction term is statistically significant, it accounts for much less (1.83%) of the overall variation compared to the factors catalyst (25.31%) and Loading (65.18).

Table 14. Shows the P-values for the significant parameters for $ECSA_{Cap}$.

Source	P-Value
Cat[HTC]	0.001
WP Error	0.925
Loading	0.001
Cat[HTC]*Loading	0.024

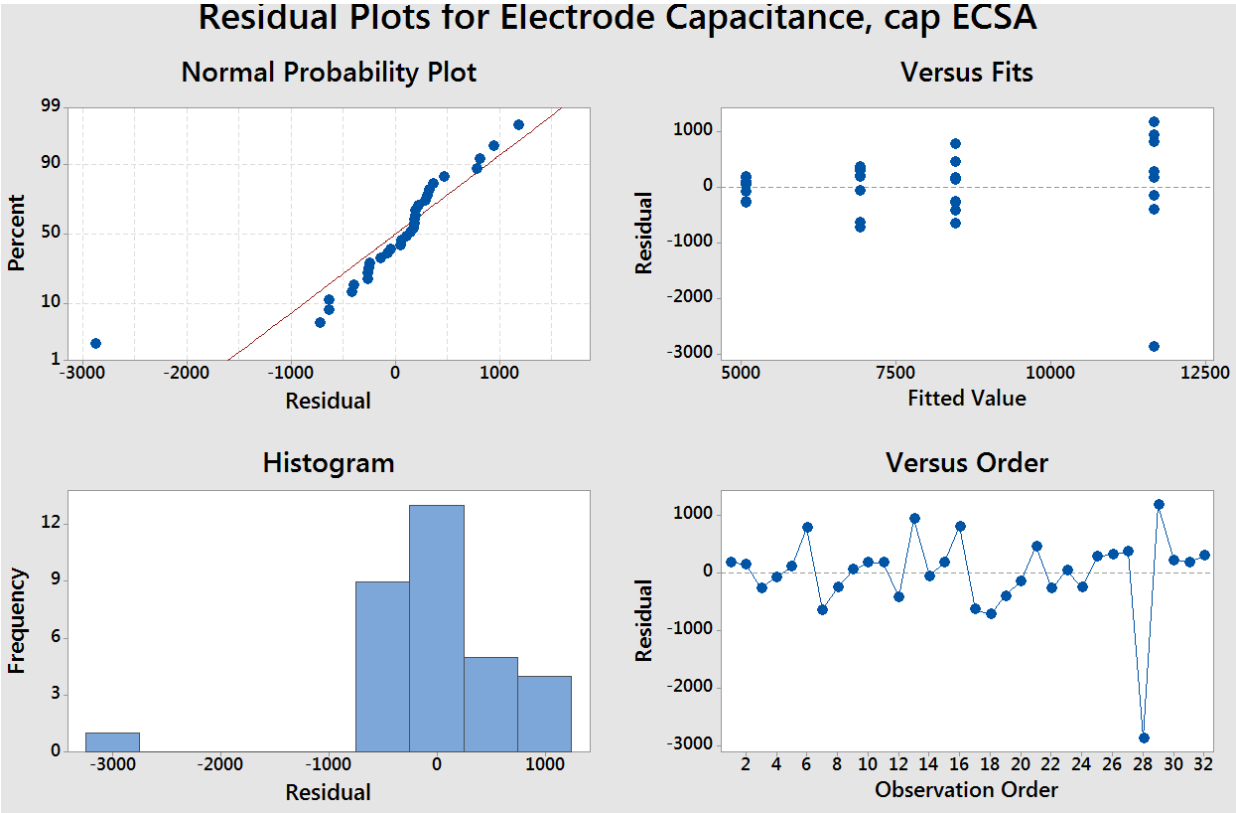

Figure 100. Residual plots for split-plot analysis for $ECSA_{Cap}$. Units for residual are cm^2.

The residuals follow an approximately normal distribution with the exception of point 28 as expected, which has a standardised residual of -4.16. Apart from this, the residual versus fit and observation order look reasonable. The analysis suggests that the following simplified model provides a good fit to the observed data.

Cap ECSA = Catalyst type + Loading + Catalyst type*Loading + error

The fit of data to the reduced model is shown in Table 15. 98.35% of the variation in the whole plots is accounted for by the [HTC] factor catalyst and 90.23% of the variation in the subplots is accounted for by the [ETC] factor loading in addition to the interaction term Cat[HTC]*Loading.

Table 15. Summary statistics for the model of $ECSA_{Cap}$.

S	R^2(SP)	S(WP)	R^2 (WP)
798.563	90.23%	*	98.35%

A similar analysis was carried out for hydrogen peaks ECSA. The charge associated with the hydrogen features of the cyclic voltammogram.

Table 16. Shows the P-values for the significant parameters for $ECSA_H$.

Source	P-Value
Cat[HTC]	0.001
WP Error	0.186
Loading	<0.001

The Catalyst type accounts for 36.27% of the total variation and Loading 51.24% of the total variation. Unlike the model for $ECSA_{Cap}$, the variation explained by the interaction term Cat[HTC]*Loading is not statistically significant. The analysis suggests the following simplified model provides a satisfactory fit to the observed data.

H ECSA = Catalyst type + Loading + error

Table 17. Summary statistics for the model of $ECSA_{Cap}$.

S	R^2(SP)	S(WP)	R^2 (WP)
1003.20	84.64%	403.336	91.92%

Overall the summary statistics for the model fit shows that 91.92% of the variations in the whole plots are accounted for by the single HTC factor catalyst type, and 84.64% of the variation in the subplots is accounted for by the ETC factor Loading.

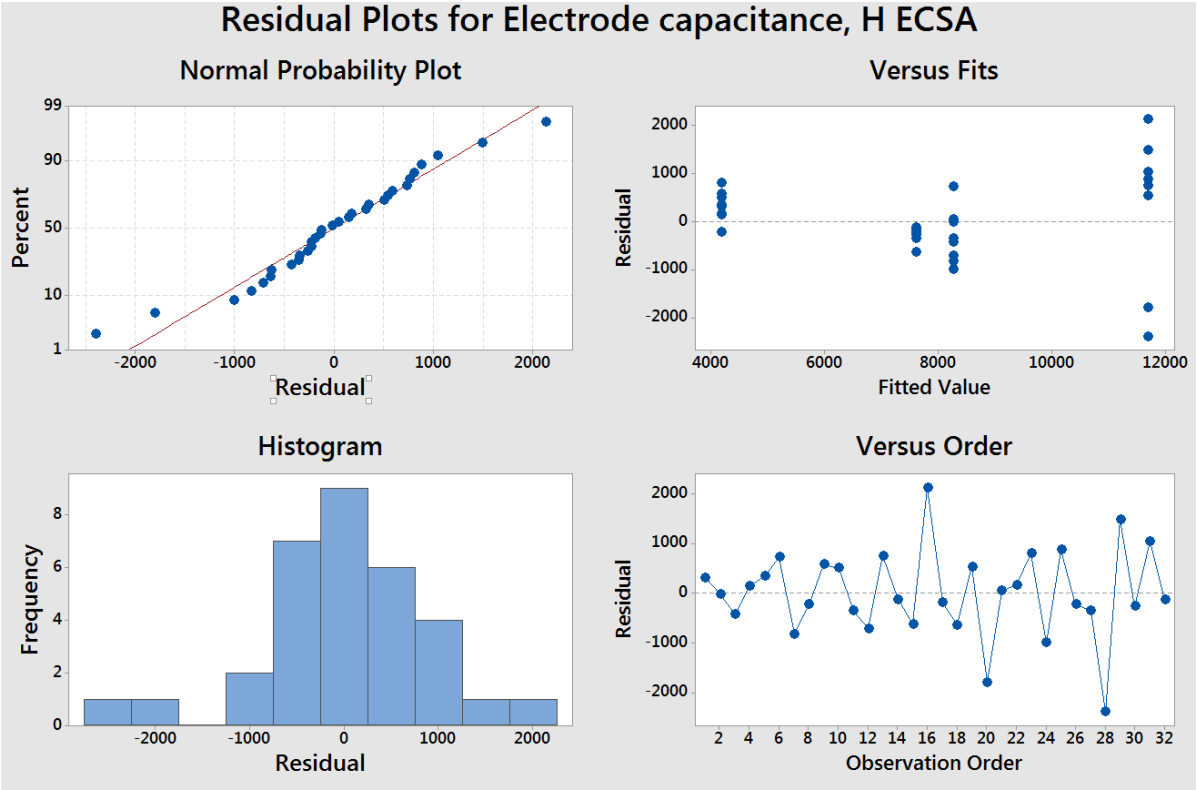

Figure 101. Residual plots for H $ECSA_H$. Units for residual are cm^2.

Overall the residual fits are approximately normal. This suggests the model is a good fit for the data. Both methods of measuring electrode surface area produce models whose surface area depends significantly on catalyst type and loading, which is to be expected as the different catalysts are defined by surface area, and using more material leading to higher surface areas makes logical sense. The lack of impact from the dispersing agent is surprising though, as when used it should keep the catalyst particles apart leading to a higher surface area.

5.3.4 Regression Analysis of Response time versus Surface area.

Previous analysis of response time data suggested that for both H_2 and CO the T90 response was controlled by the same factor that effected the surface area measurements (catalyst type and loading). Indicating there may be a good correlation between response time and surface area. Figure 102 and Figure 103 show regression fits for CO and H_2 response time versus the different methods of measuring surface area.

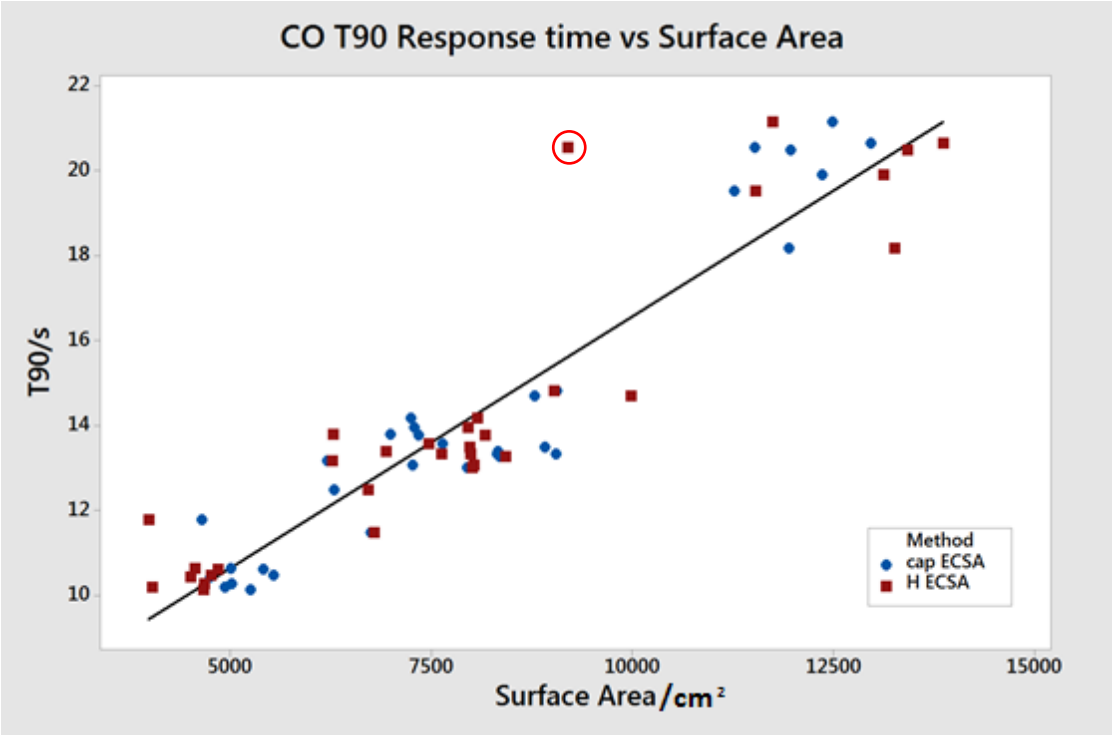

Figure 102. Regression fits for CO T90 response time versus $ECSA_{Cap}$ (blue) and $ECSA_{H}$ (red) surface area measurements. Point highlighted by red circle was identified as an outlier in the regression analysis.

The most concise fit to the data is a single straight line given by the following regression fit. The addition of separate regression fits for each measurement method does not give an improved description of the data.

$$\text{T90 CO} = 4.708 + 0.001186 \text{ Surface Area}$$

Table 18. Regression analysis of the CO T90 vs catalyst surface area fit.

S	R^2	R^2(adj)
1.24882	87.05%	86.84%

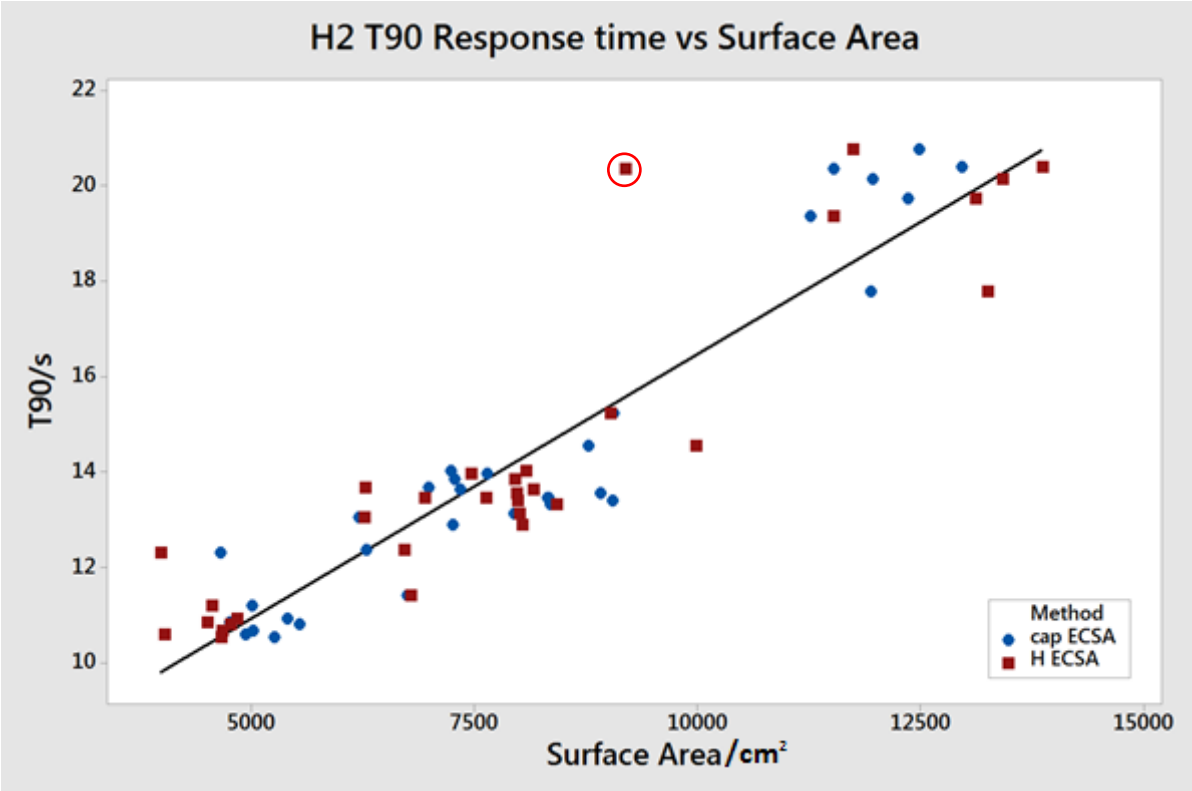

Figure 103. Regression fits for H_2 T90 response time versus $ECSA_{Cap}$ (blue) and $ECSA_H$ (red) surface area measurements. Point highlighted by red circle was identified as an outlier in the regression analysis.

The most concise fit to the data is also a single straight line given by the following regression fit.

$$T90\ H2 = 5.388 + 0.001107\ Surface\ Area$$

Table 19. Regression analysis of the H_2 T90 vs catalyst surface area fit.

S	R^2	R^2(adj)
1.22730	85.85%	85.62%

The regression fits are very similar for both CO and Hydrogen with the R^2(adj) values for both gases being greater than 85%, shown in Table 18 and Table 19. Therefore 85% of the variability in the T90 response time data can be explained by the surface area of the catalyst. Knowing this, to reduce the response time of the sensor, reducing the surface area of the electrode would be recommended. This could be reasoned by having less surface area to saturate, therefore taking less time.

5.3.5 SEM Cross-Sections

Selected cross sectional SEM images will be displayed to highlight the differences observed. All the electrodes were imaged, but many were very similar and therefore haven't been reported in this work.

The most noticeable structural changes were observed when the dispersing agent was varied. Figure 104 and Figure 105 show the effect of the dispersing agent on the structure of the electrodes. There are clear differences with the electrode that has no dispersing agent and is made up of two layers, a dense layer on the bottom and a more porous layer on the top of the electrode (Figure 104). Figure 105 is in contrast and shows a single homogenous layer. Therefore, despite the dispersing agent having little effect on the measured parameters in the design of experiment analysis, there is a clear effect on the electrode structure. This is surprising as it might be expected that different electrode structures would change the sensitivity and response time of the sensors. There was also little effect on the electrochemical surface area measurements, meaning that either the structure has no effect on these diagnostics or the images are not on the appropriate scale to see the important structural effects.

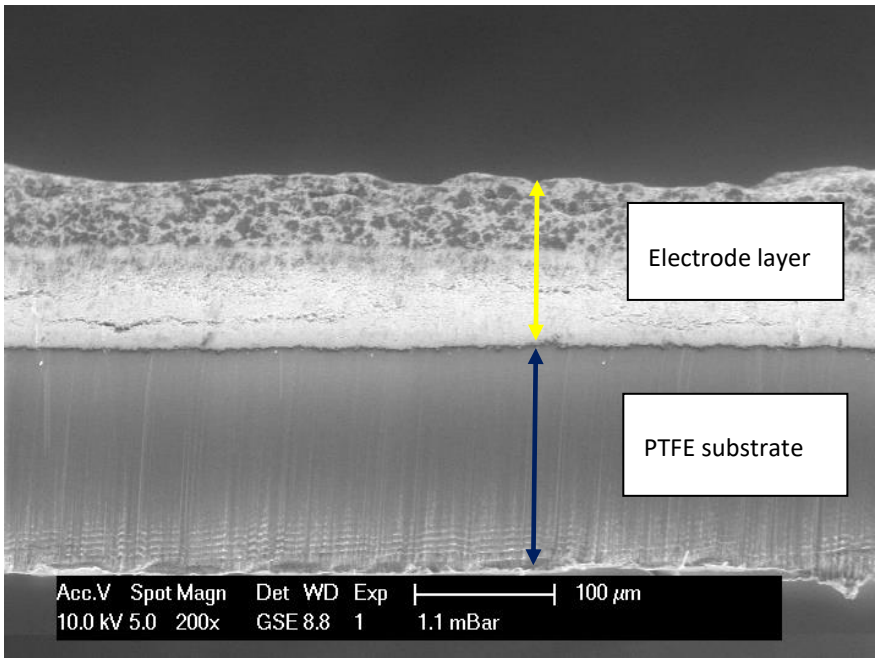

Figure 104. SEM electrode cross-section image for an electrode produced during Run 6 (catalyst Low, 12 wt% PTFE, 0 wt% dispersing agent, 50 mg weight and 800 N pressure).

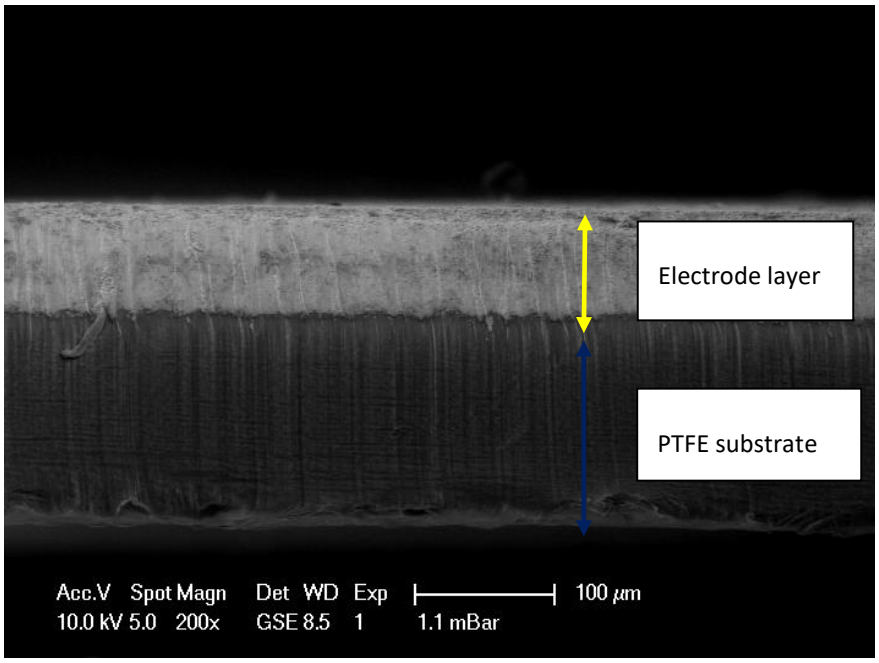

Figure 105. SEM electrode cross-section image for an electrode produced during Run 2 (catalyst Low, 12 wt% PTFE, 0.01 wt% dispersing agent, 50 mg weight and 800 N pressure).

All the other input parameters made no observable change to the SEM images.

5.4 Conclusions

The main aim was completed and improvements to the electrode design can be recommended. The high surface area catalyst could be used to reduce cost, and it should be used at a low loading to minimise the sensitivity to H_2 while not impacting much on the sensitivity to CO (also reducing cost). Having a lower loading will also reduce the response time of the sensors, another benefit. The values used for PTFE content and pressing pressure were not found to be as significant for any of the tests, therefore it may be wise to widen the range of values they are varied between. The dispersing agent had a small but statistically significant impact on the sensitivity of both gases, and was also shown to improve the homogeneity of the electrode structure on the ~100 micron scale.

In addition to the main objectives, it was also found that the electrochemically active surface area of a porous electrode can be determined by analysing the low frequency AC impedance spectroscopy treating the response as if it were only a capacitor. This method gave values very similar (although slightly offset) to measuring the charge of the hydrogen peaks. This could have a use in commercial products, like gas sensors, to monitor the degradation (loss of surface area) of electrodes.

Further work could be conducted to investigate other parameters in the sensor build, for example the capillary size and the oven temperatures at which the electrodes are cured. Expanding the range of loadings would also show how low the loading can go before the effect on the CO sensitivity is too great. Tests using carbon-supported catalysts may also allow for lower metal loadings and therefore cheaper electrodes.

The calculation of the ECSA using AC impedance measurements could be used during sensor operation, but further tests would be required to ensure that the response in the working sensor is similar to the lab based results.

5.5 References

1 Gordon, R. B.; Bertram, M.; Graedel, T. E. *Proc. Natl. Acad. Sci. U. S. A.* **2006**, *103* (5), 1209–1214.

2 Sui, S.; Wang, X.; Zhou, X.; Su, Y.; Riffat, S.; Liu, C. *J. Mater. Chem. A* **2017**, *5* (5), 1808–1825.

3 Montgomery, D. C. *Design and analysis of experiments*, 8th ed.; John Wiley & Sons, Inc: Hoboken, 2013.

4 Ott, L.; Longnecker, M. *An introduction to statistical methods and data analysis.*, 6th ed.; Brooks/Cole Cengage Learning: Australia, 2010.

5 Kowalski, S. M.; Potcner, K. J. *Qual. Prog.* **2003**, *36* (11), 60–66.

6 Potcner, K. J.; Kowalski, S. M. *Qual. Prog.* **2004**, *37* (12), 67–74.

7 J. Bett, K.Kinoshita, K. Routsis, P. S. *J. Catal.* **1973**, *29* (1), 160–168.

8 Biegler, T.; Rand, D. A. J.; Woods, R. *J. Electroanal. Chem. Interfacial Electrochem.* **1971**, *29* (2), 269–277.

9 de Levie, R. *Electrochim. Acta* **1963**, *8* (10), 751–780.

10 Raistrick, I. D. *Electrochim. Acta* **1990**, *35* (10), 1579–1586.

11 Pletcher, D. *A First Course in Electrode Processes*, 2nd ed.; The Royal Society of Chemistry: Cambridge, 2009.

12 Elliott, J. M.; Owen, J. R. *Phys. Chem. Chem. Phys.* **2000**, *2* (24), 5653–5659.

13 Reid, O.; Saleh, F. S.; Easton, E. B. *Electrochim. Acta* **2013**, *114*, 278–284.

14 Engineering ToolBox. Air - Diffusion Coefficients of Gases in Excess of Air https://www.engineeringtoolbox.com/air-diffusion-coefficient-gas-mixture-temperature-d_2010.html (accessed Sep 18, 2018).

Chapter 6: Conclusions

The overall aim of this thesis was to develop the understanding of surface processes on platinum electrodes with a view to making cheaper, more efficient gas sensors by better understanding and optimising the most important factors in the electrode manufacturing process. This aim was achieved by two different approaches. Firstly electrochemical measurements have built on the work of the Koper group extending the pH ranged where the Nernst equation can accurately predict the potential of hydrogen features on platinum voltammograms.[1–3] Secondly, a range of XAS techniques have been employed to comprehensively study the oxidation of platinum nanoparticles.

The electrochemical studies presented in chapter 3 show very strong agreement with values previously reported in the literature, shown in Figure 106. The extension of the pH range down to -5 was made possible by using the Hammett acidity function in place for values less than one.

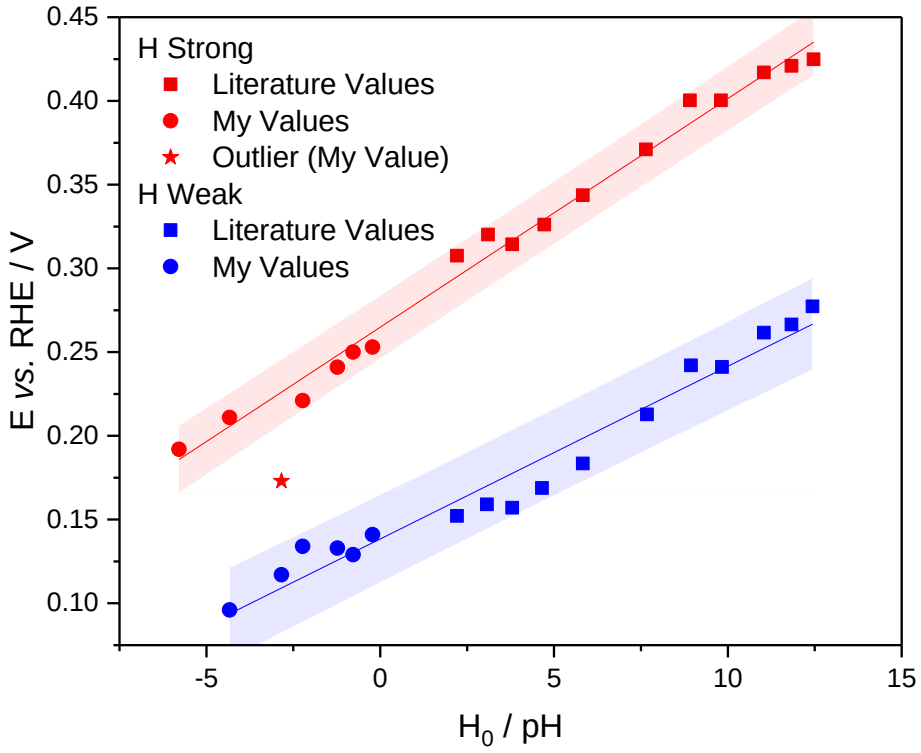

Figure 106. Plot showing the relationship between the hydrogen peaks and Hammet acidity function of the perchloric acid electrolyte, and values published by Gisbert et al. versus pH.[3] The coloured bands indicate the 95% confidence limit of the trendlines.

Comparison of the strong hydrogen peak with the oxide formation inflection point was shown to correlate linearly with electrolyte concentration. As a result, this can be used as a diagnostic in gas sensors, and other electrochemical devises where the electrolyte concentration may vary with

environmental factors over its life span.[4] The empirically derived relationship is shown in equation 35.

$$[H_2SO_4] = \frac{\Delta V - 0.606 \pm 0.008}{0.0124 \pm 0.0015}$$

Equation 35

In Chapter 4 a number of XAS techniques provided different information about surface processes on Pt/C. The additional information measured by the HERFD XANES required an extra platinum oxide species to satisfy the linear combination fitting, a species which would not be identified by convention XANES. This is in agreement with the findings of Merte *et al*.[5] The results of the two XANES LCFs are shown in table 1.

Table 20. Presents the different information that can be extracted from the HERFD XANES and conventional XANES

	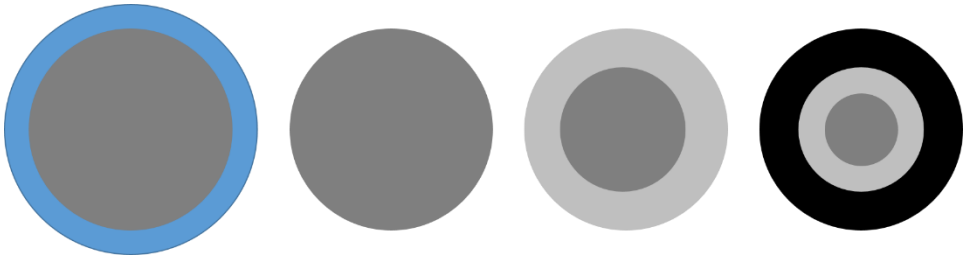			
Method	Pt with H adsorbed	Pt	Pt core with Pt_3O_4 shell	Pt core with Pt_3O_4 interface with PtO_2 shell
Conventional XANES	-600 to -500 mV *vs.* SMSE	- 400 to +200 mV *vs.* SMSE	N/A	+300 to +600 mV *vs.* SMSE (without Pt_3O_4 interface)
HERFD XANES	-600 to -300 mV *vs.* SMSE	- 200 to +0 mV *vs.* SMSE	+0 to +300 mV *vs.* SMSE	+400 to +600 mV *vs.* SMSE

Convention EXAFS remained the best data collected for that part of the spectrum, although there is promise that combining the results with EDE measurements could give accurate fits (from the conventional EXAFS or HERFD XANES) along with high time resolution. More work needs to be done to optimise the EDE measurements.

The final results chapter concluded high surface area catalysts could be used to reduce cost, and should be used at a low loading to minimise the sensitivity to H_2 while not impacting much on the

sensitivity to CO. Also reducing the response time of the sensors, another benefit. The dispersing agent had a small but statistically significant impact on the sensitivity of both gases, and was also shown to improve the homogeneity of the electrode structure on the ~100 micron scale measured using a SEM.

Additionally AC impedance measurements were also shown to be a good estimation of ECSA, when using the low frequency data and assuming the electrode behaves as a capacitor, and could be used during sensor operation. However, further tests would be required to ensure that the response in the working sensor is similar to the lab-based results.

6.1 References

1 van der Niet, M. J. T. C.; Garcia-Araez, N.; Hernández, J.; Feliu, J. M.; Koper, M. T. M. *Catal. Today* **2013**, *202*, 105–113.

2 Huang, Y.-F.; Kooyman, P. J.; Koper, M. T. M. *Nat. Commun.* **2016**, *7*.

3 Gisbert, R.; García, G.; Koper, M. T. M. *Electrochim. Acta* **2010**, *55*, 7958–7965.

4 Leach, A. S.; Russell, A. E. WPO, WO2018/059717Al, **2016**.

5 Merte, L. R.; Behafarid, F.; Miller, D. J.; Friebel, D.; Cho, S.; Mbuga, F.; Sokaras, D.; Alonso-Mori, R.; Weng, T. C.; Nordlund, D.; Nilsson, A.; Roldan Cuenya, B. *ACS Catal.* **2012**, *2* (11), 2371–2376.